

Technical Report

Battery Iron from Minnesota Iron Resources

Submitted by:

Dr. Sunil Kumar Tripathy

Mr. Matthew Mlinar

Mr. Kyle Bartholomew

Date:

October 29, 2025

Report Number:

NRRI/TRC-2025-48

Collaborators:

Form Energy

Funding:

Minnesota Department of Commerce

Technical Report Information

Recommended Citation

Tripathy, S.K., Mlinar, M.A., and Bartholomew, K., 2025. Battery Iron from Minnesota Iron Resources. Natural Resources Research Institute, University of Minnesota Duluth, Technical Report NRRI/TRC-2025/48.

Copyright

©2025 by the Regents of the University of Minnesota. All rights reserved.

Keywords

Battery, Iron-air, High-purity iron, Iron anode, Long-duration energy storage, Geo-metallurgy, Beneficiation, Characterization, Automated Mineralogy, Magnetic Separation, Flotation

Contact

Natural Resources Research Institute, University of Minnesota, Duluth 5013 Miller Trunk Highway, Duluth, MN 55811-1442

Telephone: 218.788.2694; Email: nrri-reports@umn.edu; Website: http://www.nrri.umn.edu

NRRI Publications: https://nrri.umn.edu/research/publications

UMN Diversity, Equity and Inclusion Statement

The University of Minnesota is committed to the policy that all persons shall have equal access to its programs, facilities, and employment without regard to race, color, creed, religion, national origin, sex, age, marital status, disability, public assistance status, veteran status, or sexual orientation. Learn more at https://diversity.umn.edu/

Table of Contents

List of Tablesi	İ
List of Figuresiv	/
Executive Summaryv	Ί
Introduction	1 2 3
Project Goal and Objectives5	5
Experimental Methods 6 Iron Ore Test Samples 6 Characterization Studies 7 Comminution and Beneficiation Studies 8	ე 7
Results and Discussion	3 2
Magnetic Separation using Low-Intensity Magnetic Separation (LIMS)	3
Form Energy Battery Testing Results61	
Conclusions	
Acknowledgements63	3
References64	1
Appendices	7 1 0

List of Tables

Table 1. Sample details used in the project	6
Table 2. Experimental and process conditions considered for the flotation tests	12
Table 3. Sample details used in the project	13
Table 4. Sample details used in the project	14
Table 5. Specific gravity and bulk density of the samples	15
Table 6. Results of the Satmagan analysis of the samples	15
Table 7. Key magnetic properties from the hysteresis curve	16
Table 8. Chemical analysis of as-received iron ore samples analyzed at NRRI	17
Table 9. Size-wise chemical analysis of Sample A	18
Table 10. Size-wise chemical analysis of Sample C	18
Table 11. Size-wise Chemical Analysis of Sample B	
Table 12. Size-wise Chemical Analysis of Sample D	19
Table 13. Semi-quantification of mineral phases by Rietveld refinement method	22
Table 14. Size-wise XRD analysis and semi-quantification of mineral phases in Sample A	22
Table 15. Size-wise XRD analysis and semi-quantification of mineral phases in Sample B	23
Table 16. Size-wise XRD analysis and semi-quantification of mineral phases in Sample C	23
Table 17. Size-wise XRD analysis and semi-quantification of mineral phases in Sample D	23
Table 18. Summary of the point analysis of magnetite in Sample C	24
Table 19. Summary of the geo-chemical correlations and behavior	26
Table 20. Summary of EPMA point analysis of the image depicted in Figure 17	
Table 21. Summary of EPMA analysis of Sample C	32
Table 22. Results on particle size of milled samples	
Table 23. Results of the Davis Tube tests at different grinding times for Sample A	36
Table 24. Results of the Davis Tube tests at different grinding times for Sample C	
Table 25. Results on magnetic separation in a single-stage LIMS for Sample A	
Table 26. Results on magnetic separation in a single-stage LIMS for Sample C	
Table 27. Results on magnetic separation in a two-stage LIMS for Sample A	
Table 28. Results on magnetic separation in a two-stage LIMS for Sample C	42
Table 29. Design of experiment considered for the flotation tests, along with test	40
Conditions	
Table 30. Results of the flotation concentrate/underflow for Sample A	40
Table 31. Parameter estimate as well as other model parameters along with statistical data for mass pull, grade ($Fe_{(T)}$, SiO_2) of flotation concentrate/underflow for Sample A	48
Table 32. Parameter estimate as well as other model parameters along with statistical	40
data for recovery Fe _(T) , rejection of SiO ₂ of flotation concentrate/underflow for Sample A	48
Table 33. Results of the flotation concentrate/underflow for Sample C	
Table 34. Results of parameter estimate, as well as other model parameters, along with	
statistics data for mass pull, grade (Fe _(T) , SiO ₂), recovery (Fe _(T) %) of flotation	
concentrate/underflow for Sample C	54
Table 35. Design of experiment (DOE) adopted for the combination of magnetic	EG
separation and flotationseparation and flotation	oo

Table 36. Results of the combined studies using magnetic separation and flotation for Sample A	57
Table 37. Results of the combined studies using magnetic separation and flotation for Sample C	57
Table 38. Comparison of the results achieved in three different processing routes at different particle sizes (Sample A)	59
Table 39. Comparison of the results achieved in three different processing routes at different particle sizes (Sample C)	60
Table 40. Chemical analysis of as-received iron ore samples, along with major, minor and trace elements analyzed at ALS Global	70
Table 41. Chemical analysis of as-received iron ore samples, along with major, minor and trace elements analyzed at ALS Global	70
Table 42. Chemical analysis of as-received iron ore samples, along with major, minor and trace elements analyzed at ALS Global	70

List of Figures

Figure 1. Opportunities in Iron-air Battery Market 2025–2033 (Data Insights Market, 2024)	2
Figure 2. The unit iron-air cell with an anion membrane in an alkaline electrolyte, showing the main processes occurring in a) charge and b) discharge cycles	3
Figure 3. Location map of identified ferrous mineral resources in Minnesota	6
Figure 4. Characterization methods used in the project for analyzing iron ore samples at different stages	7
Figure 5. STM VRM5 experimental set-up at NRRI	8
Figure 6. Experimental procedure for Liberation studies using Davis Tube Tester	9
Figure 7. Wet low-intensity magnetic separator at NRRI	10
Figure 8. LIMS configuration considered for the present study	11
Figure 9. Flotation experimental set-up at NRRI	12
Figure 10. Particle size distribution of four samples used in this project	14
Figure 11. Hysteresis curve measured at room temperature for the as-received samples	16
Figure 12. X-ray diffraction pattern of as-received Sample A	20
Figure 13. X-ray diffraction pattern of as-received Sample B	20
Figure 14. X-ray diffraction pattern of as-received Sample C	21
Figure 15. X-ray diffraction pattern of as-received Sample D	21
Figure 16. Silicon deportment in magnetite grains in Sample C	25
Figure 17. Backscattered image (BSE) of particles of coarser size fraction (+25 μm) of Sample C	27
Figure 18. EPMA analysis of magnetite particles along with EDS data	29
Figure 19. EPMA analysis of magnetite and other associated particles along with EDS data	29
Figure 20. Elemental mapping 1 of particles of Sample C	30
Figure 21. Elemental mapping 2 for particles of Sample C	31
Figure 22. Particle size distribution of the mesh of grind studies at three different grinding intervals for Sample A	33
Figure 23. Particle size distribution of the mesh of grind studies at three different grinding intervals for Sample C	34
Figure 24. RSM-CCD experimental design	43
Figure 25. Grade-recovery correlation for iron and silica content in the flotation concentrate/underflow for Sample A	44
Figure 26. Kinetics curve for froth recovery of each stage of flotation (NRRI Test 1) for Sample A	45
Figure 27. Interactional effects of variables on performance of flotation responses for Sample A	49
Figure 28. Grade-recovery correlation for iron and silica content in the flotation concentrate/underflow for Sample C	50
Figure 29. Kinetics curve for froth recovery of each stage of flotation (NRRI Test 1) for Sample C	51
Figure 30. Interactional effects of variables on performance of flotation responses for Sample C	55

both magnetic separation and flotationflow for the test work with a combination of	56
Figure I. Correlation between total iron and silica content reported in magnetite grains for	
Sample C Figure II. Correlation between total iron and silica content with titanium reported in magnetite grains for Sample C	71
Figure III. Correlation between total iron and silica content with zinc reported in magnetite grains for Sample C	73
Figure IV. Correlation between total iron and silica content with manganese reported in magnetite grains for Sample C	74
Figure V. Correlation between total iron and silica content with calcium reported in magnetite grains for Sample C	75
Figure VI. Correlation between total iron and silica content with magnesium reported in magnetite grains for Sample C	76
Figure VII. Correlation between total iron and silica content with sodium reported in magnetite grains for Sample C	77
Figure VIII. Correlation between total iron and silica content with potassium reported in magnetite grains for Sample C	77
Figure IX. Correlation between total iron and silica content with phosphorous reported in magnetite grains for Sample C	78
Figure X. Correlation of total iron and silica content with sulfur reported in magnetite grains for Sample C	78
Figure XI. Correlation of total iron and silica content with chlorine reported in magnetite grains for Sample C	79
Figure XII. Kinetics curves for froth recovery of reach stage of flotation (NRRI Test 2–10) for Sample A	80
Figure XIII. Relation between actual and predicted responses based on the developed models (Sample A)	81
Figure XIV. Kinetics curves for froth recovery of reach stage of flotation (NRRI Test 2–10) for Sample C	82
Figure XV. Relation between actual and predicted responses based on the developed models (Sample C)	83
Figure XVI. XRD pattern for the magnetic fraction of the optimum condition at double-stage magnetic separation in LIMS for Sample A	
Figure XVII. XRD pattern for the non-magnetic fraction of the optimum condition at double-stage magnetic separation in LIMS for Sample A	
Figure XVIII. XRD pattern for the concentrate (underflow) of flotation process for Samp	ple
Figure XIX. XRD pattern for the tailings (froth) of flotation process for Sample A	
Figure XX. XRD pattern for the magnetic fraction of the optimum condition at double-stage magnetic separation in LIMS for Sample B	86
Figure XXI. XRD pattern for the non-magnetic fraction of the optimum condition at double-stage magnetic separation in LIMS for Sample B	86
Figure XXII. XRD pattern for the concentrate (underflow) of flotation process for Sample B	87
Figure XXIII. XRD pattern for the tailings (froth) of flotation process for Sample B	87

Executive Summary

The global transition toward a renewable energy-based economy is critically dependent on the development of cost-effective, long-duration energy storage solutions to ensure grid stability and reliability. Iron-air batteries are emerging as a transformative technology in this sector, offering the potential for multi-day energy storage at a fraction of the cost of incumbent technologies like lithium-ion batteries. A key component of this promising technology is the battery's anode, which requires a high-purity iron feedstock and presents a significant opportunity to leverage Minnesota's vast taconite resources, potentially establishing a secure, domestic supply chain for a critical component in the US clean energy future.

This project, a collaboration between the Natural Resources Research Institute (NRRI) and our industrial partner, Form Energy, was undertaken to investigate this opportunity. Funded by the Minnesota Department of Commerce, this research provides a comprehensive geo-metallurgical and beneficiation study of several Minnesota iron ores to determine the technical feasibility of producing battery-grade iron concentrate from existing resources.

The primary objective of this project was to determine if Minnesota taconite resources can be processed to meet the stringent purity specifications required for iron-air battery anode material. The specific goals were to:

- Conduct a comprehensive geo-metallurgical characterization of representative taconite samples to understand their mineralogy, chemistry, and physical properties.
- Evaluate and compare different mineral processing options using only incumbent technologies, including magnetic separation and flotation, to identify the most effective route for impurity removal.
- Enable feasibility testing of high-purity iron oxide for battery manufacturing processing by Form Energy if the iron concentrate achieved specific quality targets.

Creating an iron-based battery precursor material at the lowest cost was paramount. Therefore, a key constraint in this research was that mineral processing testing would be limited to conventional physical separation techniques such as grinding, magnetic separation, and silica froth flotation, while higher-cost extractive metallurgical approaches, such as pyrometallurgy, hydrometallurgy, or electrometallurgy, were considered out of scope. Furthermore, the product was not pelletized but instead kept in the form of a fine concentrate without binders, flux, or any other reagents being mixed with the material.

The project successfully characterized four distinct taconite samples from the Central and Western Mesabi range (Sample A, B, C, and D) and systematically evaluated their response to mineral processing techniques. The investigation yielded several key findings that confirm the potential of these resources. The four samples were categorized into two distinct groups based on their initial properties. Samples A and C were identified as high-grade magnetite concentrates (Blast Furnace grade) with an initial iron content of approximately 67% Fe. In contrast, Samples B and D were low-grade ores with only ~31% Fe and very high silica content (~48%). Detailed mineralogical analysis using XRD and automated mineralogy confirmed that magnetite (Fe₃O₄) is the primary valuable mineral and quartz (SiO₂) is the main impurity, with minor amounts of other complex silicates and carbonates present. Advanced electron probe micro-analysis (EPMA) revealed the nature of trace impurities, showing that elements like magnesium and calcium are hosted in separate gangue minerals, while manganese substitutes for iron within the magnetite

and exists in external silicate phases. This detailed characterization was crucial for designing an effective beneficiation strategy.

The beneficiation study evaluated several processing options, including single-stage Low-Intensity Magnetic Separation (LIMS), double-stage LIMS, silica flotation, and combined circuits with LIMS and flotation. Across the magnetic separation, a two-stage LIMS process (at magnetic field strengths of 1,260 and 600 Gauss) after fine grinding proved to be the most robust and efficient process. For both Samples A and C, this process produced a final concentrate with higher impurities with reference to the target specification. For Sample A, after grinding to 15 μ m, the two-stage LIMS process yielded a concentrate with an iron grade of 71.02%Fe_(T), a low silica content of 1.07%, and an iron recovery of 96.0%. Similarly, for Sample C, the same process achieved a concentrate with a grade of 70.68%Fe_(T), 1.23% silica, and an iron recovery of 96.9%.

The reverse flotation of silica using amine as a collector was systematically optimized using a Response Surface Methodology with Central Composite Design (RSM-CCD). This statistical approach successfully modeled the complex, non-linear relationships between grind size and collector dosage. The resulting contour plots visually demonstrated the classic grade-recovery trade-off, where fine grinding combined with a high collector dosage yielded the highest grades but at the cost of lower recovery. While flotation could produce a high-purity concentrate (e.g., >71% $Fe_{(T)}$, <1.0% SiO_2), it consistently resulted in lower iron recoveries compared to the LIMS process under optimal conditions.

Optimum conditions for Sample A were achieved using a combination of LIMS and froth flotation, which produced a high-purity iron concentrate with 71.44% $Fe_{(T)}$ and silica content of 0.86%. However, the total iron recovery values were low. Similarly, Sample C also produced an iron concentrate with 71.37% $Fe_{(T)}$ with silica content of 0.86% with a low recovery. Although this process option produced a higher quality pure iron concentrate than LIMS alone, the product yield was significantly lower, which may not be economically viable.

The study found that flotation, as well as LIMS combined with flotation, could produce iron grade >71% $Fe_{(T)}$ with minimum gangue content (< 1%) when re-grinding the test samples to approximately 15-30 μ m. These methods were found to be the most effective and economically promising processing route when constrained to physical separation approaches. Both of these process options represent an optimal balance of product quality and process efficiency in terms of recovery.

NRRI's comprehensive experimental results and detailed analysis indicated that producing highpurity iron concentrates from Minnesota taconite resources is technically feasible and promising. Although the product quality parameters did not technically meet Form Energy's confidential purity specifications, refined Samples A and C were delivered to Form Energy for further testing. Form Energy test results remain confidential. However, Form Energy reported that the initial testing showed favorable electrochemical behavior at the beginning of life in iron-air battery cells. This positive result was consistent between the two materials sourced from the two different mines.

Based on these promising outcomes, the following steps are recommended to advance these technologies toward commercial application:

- 1. Develop process flowsheets with detailed material balance using both incumbent and enhanced beneficiation processes.
- 2. Conduct pilot-scale trials of the beneficiation process flowsheet to validate the benchscale results and demonstrate the process's scalability and robustness under continuous operation.

- 3. Generate a larger quantity of the high-purity iron concentrate with different impurity levels from the pilot trials for delivery to our industrial partner for direct testing and validation of its performance as an anode material in their iron-air battery systems.
- 4. Expand the investigation to include a wider range of Minnesota iron resources to assess the broader applicability of these findings and to identify other potential sources of feedstock such as a stockpile, tailings, and over-burden.
- 5. Perform a detailed techno-economic assessment of the recommended flowsheet to evaluate the capital and operating costs, and to determine the overall economic viability and competitiveness of producing battery-grade iron from Minnesota resources.
- 6. Research the use of high-purity iron oxide as a precursor material for other non-steelmaking industrial applications such as permanent magnets or alloys.

Introduction

Background

As the U.S. power grid transitions to a greater reliance on intermittent renewable energy, the need for effective energy storage has become paramount. In 2023, renewable sources accounted for a record 23% of US electricity generation, with solar and wind power leading this expansion (U.S. EIA, 2024). However, this growth presents a fundamental challenge: ensuring reliability when the sun isn't shining or the wind isn't blowing. While traditional lithium-ion batteries are well-suited for short-duration applications (typically 2–4 hours) to stabilize grid frequency, they are not an economically viable solution for addressing multi-day energy deficits. A report from the National Renewable Energy Laboratory (NREL) states that to achieve a fully decarbonized grid, the U.S. will require an estimated 120 to 350 gigawatts (GW) of long-duration storage capacity (NREL, 2023). This capability is the key for unlocking a net-zero electrical grid, enabling the storage of massive amounts of excess renewable energy and dispatching it over extended periods.

In the quest for effective long-duration storage, several battery technologies are emerging as front-runners. The focus is on systems that can store energy cost-effectively for durations of 10 hours to several days, utilizing earth-abundant and safe materials to bring levelized costs of storage down. The U.S. Department of Energy has set an aggressive target to reduce the cost of grid-scale, long-duration energy storage by 90% by 2030 (U.S. DOE, 2021).

Key leading options include:

- Iron-Air Batteries: This technology, being commercialized by companies like Form Energy, leverages the simple process of iron rusting (oxidation) and un-rusting. Its primary advantage is its extremely low-cost materials, with iron costing less than \$100 per ton, compared to thousands of dollars per ton for lithium. This allows for a projected storage system cost of less than \$20 per kilowatt-hour (kWh), a price point that makes multi-day storage economically feasible (Form Energy, 2021; Jackson et al., 2024; MIT Technology Review, 2022).
- <u>Flow Batteries:</u> These systems store energy in external tanks of liquid electrolyte, allowing for the independent scaling of power and energy capacity. Vanadium redox flow batteries are a mature technology within this category; however, their high cost, linked to the volatile price of vanadium, has been a significant barrier. Innovations in zinc-bromine and other organic chemistries aim to reduce costs and improve performance (Yao et al., 2021).
- Zinc-lon Batteries: Utilizing zinc, a metal that is significantly more abundant than lithium, these batteries offer a safer and lower-cost alternative. Many designs use non-flammable aqueous electrolytes. The global zinc-ion battery market is projected to grow from \$9.6 billion in 2023 to over \$14.5 billion by 2030, driven by its application in grid storage (MarketsandMarkets, 2023).
- <u>Sodium-Ion Batteries</u>: Functioning with a mechanism similar to lithium-ion batteries, this technology uses sodium, the sixth most abundant element in the Earth's crust. This approach avoids the supply chain issues associated with lithium while offering comparable performance for stationary storage, making it a strong candidate for reducing dependency on lithium-based chemistries (Yao, 2025).

Compared to these technology options, iron-air batteries are experiencing a renaissance, driven by a confluence of technological breakthroughs, surging demand for grid-scale storage, a strong push for domestic energy security, as well as the potential for lower-cost technology that is less

reliant on critical metals or other metals like Na or Zn. This emerging technology promises to be a cost-effective, safe, and sustainable solution for long-duration energy storage, a critical missing piece in the transition to a renewable energy-dominated future (Pillot, 2019). The market growth of the iron-air battery was analyzed by Data Insights Market (2024, **Figure 1**). A brief technical description of iron-air batteries is provided in the following section.

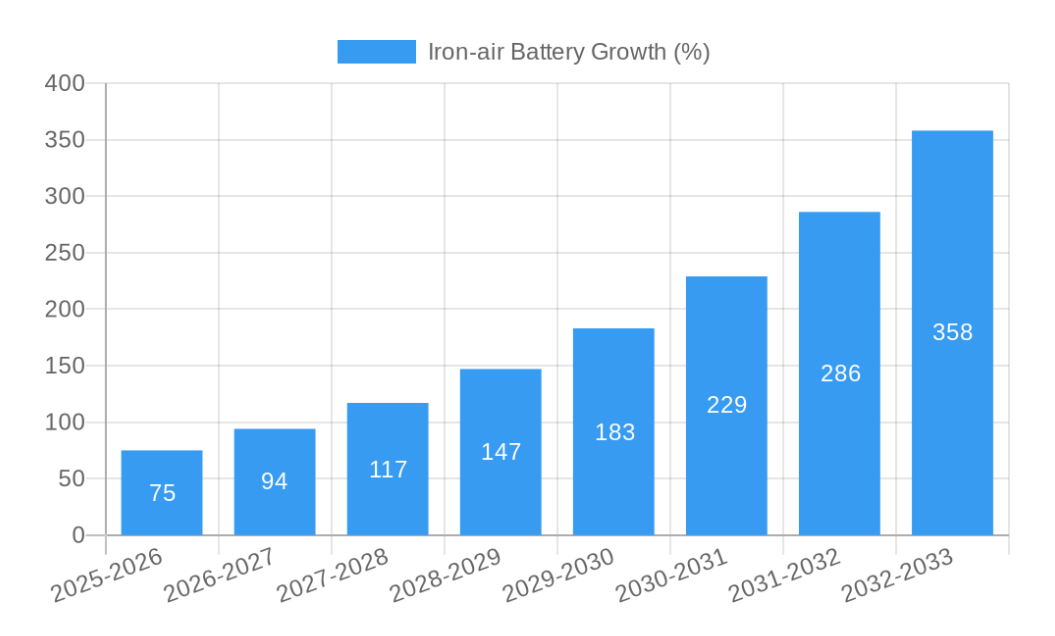


Figure 1. Opportunities in Iron-air Battery Market 2025–2033 (Data Insights Market, 2024).

Iron-Air Battery Technical Summary

The iron-air battery is a rechargeable metal-air system that uses iron as the anode and oxygen from ambient air as the cathode in an alkaline electrolyte, typically potassium hydroxide (KOH), offering a theoretical cell voltage of \sim 1.28 V. During discharge, metallic iron at the anode oxidizes to form iron (II) hydroxide and eventually magnetite (Fe $_3$ O $_4$, Equation 1), while at the cathode, oxygen from ambient air is reduced to hydroxide ions via a four-electron pathway (McKerracher et al. 2015, Equation 2). On charging, these reactions reverse, regenerating metallic iron and evolving oxygen (Equations 3 and 4). The cathode (air electrode), which reduces oxygen during discharge and evolves oxygen during charge, and the electrolyte (alkaline, KOH), facilitate ion transport and reaction kinetics (**Figure 2**).

Unlike zinc-air or lithium-air systems, iron-air batteries avoid dendrite formation, making them safer and more stable. Their energy density ranges from 50 to 110 Wh/kg, with a lifespan reaching up to 2000 cycles in recent prototypes. However, challenges remain in improving efficiency, suppressing hydrogen evolution, and developing cost-effective bifunctional air electrodes (McKerracher et al., 2015).

Discharge Cycle:

Figure 2. The unit iron-air cell with an anion membrane in an alkaline electrolyte, showing the main processes occurring in a) charge and b) discharge cycles (McKerracher et al., 2015).

Given the abundance, recyclability, and low cost of iron ore, iron-air batteries are particularly promising for grid-scale energy storage and renewable energy integration. Future research is focused on optimizing electrode materials, improving bifunctional catalysts, and developing scalable cell designs using additive manufacturing and advanced modelling.

Research Motivation

Specialized materials, including iron precursors, are required for efficient energy storage in the iron-air battery system. However, the materials available for this purpose, such as high-grade ore, are limited, precipitating the need to explore alternative iron sources. Therefore, a robust supply of iron feedstocks needs to be explored to satisfy this growing market.

The Minnesota iron mining industry contributes approximately 75% of the iron produced in the US for use in the steelmaking industry, with a capacity of approximately 40 million tons of iron oxide pellets annually from six mines (MN DNR, 2016). Taconite ore is crushed, ground in a wet mill into a fine powder approximately 40–70 microns in size, and the valuable iron minerals (e.g., magnetite and lesser amounts of hematite) are separated from the gangue impurity minerals (e.g., quartz, silicates, carbonates) using conventional wet techniques such as magnetic separation, hydroseparation, and froth flotation. The fine taconite concentrate is then filtered, combined with

a binder and typically a flux, pelletized, and sintered (fired) in an oxidizing environment at 1,200–1,315°C (2,200–2,400°F) to create an iron oxide (hematite) pellet, which is shipped via rail and ore boats to steelmaking facilities along the Great Lakes.

Two types of iron oxide pellets are produced: "blast furnace" (BF) grade and "direct reduction" (DR) grade. Each type contains residual impurities such as silica, which is found in the taconite itself, as well as binders and flux added in the pelletizing process, resulting in impurity concentrations of 4–6% SiO₂ and 2% SiO₂ for BF and DR pellets, respectively. Although this material could potentially be used directly in iron-air batteries, a higher purity feedstock is necessary to increase battery performance.

Project Team

The Natural Resources Research Institute (NRRI), a state-chartered applied research laboratory of the University of Minnesota hosted by the Duluth campus, has been conducting mineral processing research with mineral resources for decades. The NRRI team has specific expertise and capabilities to produce higher-purity iron concentrates than is produced today for the US steelmaking industry.

Form Energy is a leader in long duration energy storage using iron-air battery technology, with multiple demonstration projects throughout the US, including a 1.5 MW/150 MWh pilot project in Cambridge, Minnesota (Form Energy, 2024), and a 10 MW/1,000 MWh demonstration project in Becker, Minnesota (Form Energy, 2023).

NRRI and Form Energy share a mutual interest in developing a domestic supply chain of high-quality iron precursor materials for use in iron-air batteries. Therefore, both entities engaged the State of Minnesota to support research in this topic area.

Project Goal and Objectives

In 2024, the Minnesota Department of Commerce allocated a one-time appropriation to NRRI per Laws of Minnesota 2023, Chapter 60, Art. 10, subd. 2(p) (as amended in Minnesota Session Laws 2024, Chapter 126): [A] feasibility study to identify and process Minnesota iron resources that could be suitable for upgrading to long-term battery storage specifications.

The goal of the project was for NRRI to investigate the potential for Minnesota iron resources to be processed into a high-purity iron concentrate that could be suitable for use in Form Energy's iron-air battery technology. The following objectives were targeted in this study:

- 1. Identify two (2) Minnesota iron oxide resources and procure samples for testing,
- 2. Conduct bench-scale beneficiation studies to determine separation efficiency and concentrate quality, and
- 3. Feasibility testing by Form Energy of high-purity iron oxide for battery manufacturing if the iron concentrate achieved specific confidential quality targets.

Beyond the primary goal of investigating high-purity concentrate for iron-air battery testing, the data generated during this study would also enable NRRI and other stakeholders to investigate other end-use applications for Minnesota iron resources.

Creating an iron-based battery precursor material at the lowest cost was paramount. Therefore, a key constraint in this research was that the mineral processing testing would be limited to conventional physical separation techniques, such as rod/ball mill grinding, screening, magnetic separation, and froth flotation. Higher-cost extractive metallurgical approaches such as pyrometallurgy (e.g., smelting), hydrometallurgy (e.g., leaching and solvent extraction), or electrometallurgy (e.g., electrowinning) were considered out of scope in this study. Furthermore, the product was not pelletized but instead kept in the form of fine concentrate without binders, flux, or any other reagents being mixed with the material for battery testing.

Throughout this project, the following broader goals were also being considered:

- Produce high-purity iron oxide concentrate for non-steelmaking applications from Minnesota iron oxide resources.
- Develop sustainable, localized supply chains for battery-grade iron materials using Minnesota iron resources.
- Support Form Energy's advancement of long-duration energy storage through the use of domestic iron sources.

Experimental Methods

Iron Ore Test Samples

Four samples were received from two taconite mines located in the Central and Western portions of the Mesabi Iron Range located in northern Minnesota (Figure 3, Rao et al., 2022). Two samples were collected as a crude feed to the beneficiation plants and two as a "Blast Furnace" (BF) grade concentrate from each mine. The BF concentrate samples represent the final magnetic concentrates generated at each plant before undergoing flotation. The as-received samples were subjected to various characterization and beneficiation studies, explained in subsequent sections of this report. The four test samples acquired for this project were designated as Sample A, B, C, and D, and the details about the samples are highlighted in **Table 1**.

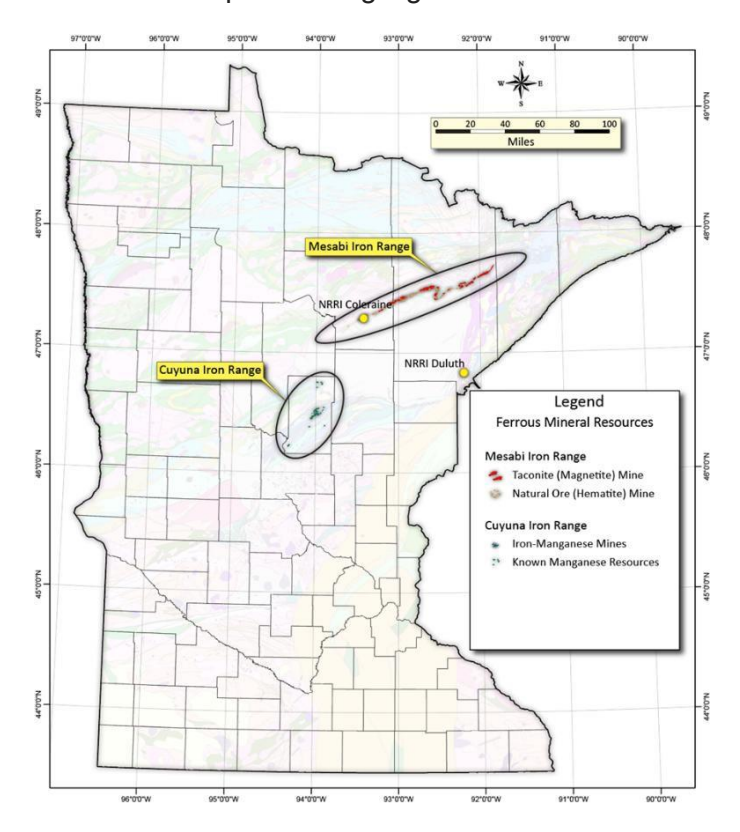


Figure 3. Location map of identified ferrous mineral resources in Minnesota (Rao et al., 2022).

Table 1. Sample details used in the project.

Sample Description	Sample Designate
Central Mesabi Flotation Feed	Sample A
Central Mesabi Rod Mill Feed	Sample B
Western Mesabi Plant Concentrate	Sample C
Western Mesabi SAG Mill Discharge	Sample D

Characterization Studies

A comprehensive characterization of iron samples is essential for designing an efficient and economically viable mineral processing flowsheet. This involves a multi-faceted approach that evaluates the physical, chemical, and mineralogical properties of each sample. Together, these analyses provide a complete picture of the material properties, potential processing challenges, and optimal methods for concentrating the iron and removing impurities. The detailed studies considered in this project are highlighted in **Figure 4**. Sample preparation for characterization starts with drying, grinding (as needed), and weighing, followed by the application of standardized analytical methods in accordance with or parallel to ISO or ASTM protocols. See Appendix A for detailed methodology and equipment.

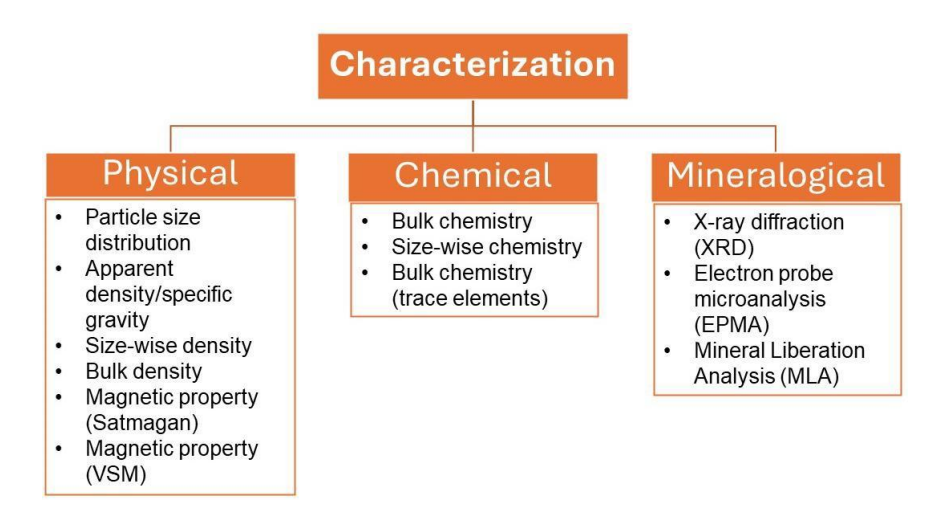


Figure 4. Characterization methods used in the project for analyzing iron ore samples at different stages.

Physical Characterization

Physical characterization was performed to assess key properties like particle size, density, and magnetism. These parameters are critical for designing the optimal flowsheet for material handling, comminution (crushing and grinding), and physical separation.

Chemical Characterization

Chemical analysis quantifies the total iron content to establish the sample purity (also known as "grade") and identifies the concentration of different deleterious elements such as silica, alumina, phosphorus, and sulfur that can negatively impact the battery manufacturing process and performance. All four as-received samples, as well as beneficiated products, were analyzed to understand the distribution of different elements.

Mineralogical Characterization

Mineralogy identifies the specific iron-bearing minerals (magnetite) as well as other associated gangue minerals. Various characterization techniques, such as XRD, EPMA, and Mineral Liberation Analysis (MLA), are employed to understand how iron-bearing minerals are interlocked with gangue minerals, which is crucial for designing the liberation and concentration strategy.

Comminution and Beneficiation Studies

Comminution (grinding) studies aimed to liberate the magnetite particles in Samples A and C were focused on the specific energy consumption in ball and vertical stirred media mills. Beneficiation (separation) studies were conducted using a low-intensity magnetic separator (LIMS) and flotation. Furthermore, liberation studies were conducted using the Davis Tube Tester after grinding at various time intervals, targeting different particle sizes. The as-received BF concentrate samples (Samples A and C) were subjected to this as well as beneficiation.

Rod Mill (Bench-Scale)

The bench scale rod mill was used to generate the requisite-sized feed material for LIMS and froth flotation separation testing. The rod mill is 21.3 cm (8.4 inches) in diameter by 35.6 cm (14.0 inches) in length with no lifters. The mill was loaded to approximately 39% volumetric loading with ninety-one (91) 1.3 cm (0.5 inch) diameter steel rods. The total rod charge weight was 28.2 kg (62.1 lbs.). The feed to the mill was targeted to be 50% (w/w).

Grindability Studies using Swiss Tower Mill

The grinding test was conducted to determine the particle size reduction characteristics and energy requirements of Sample A and C using an STM-VRM5 vertical stirred mill (**Figure 5**), which is a 5 L capacity vertical stirred mill. In addition, a modified Bond work index method was employed to generate the grindability data in a ball mill for comparative purposes.

Prior to the test, the mill was charged with ceramic grinding media (zirconia-based ceramic material) and configured for recirculation mode. The grinding media used was a 50/50% blend by weight of 4.0 and 5.0 mm high-density zirconium-aluminum oxide (ceramic beads). With a media material density of 4.7 g/cm³, the mill was charged with 6.45 kg of media, corresponding to a 40% charge level. A representative ore sample was prepared as a slurry with a target density of 40–55% solids by weight and placed in a mixing tank to ensure homogeneity. The system was calibrated to a target mill power of approximately 380–384 Watts, and the feed pump was set to deliver a specific solids throughput before the test commenced.



Figure 5. STM VRM5 experimental set-up at NRRI.

Once the system stabilized, the slurry was continuously fed and recirculated through the mill. The grinding process was timed, and at pre-determined intervals a 5-second sample of the entire slurry stream was collected from the mill discharge. This sampling procedure was repeated to generate a suite of products representing different grinding times. After the final sample was collected, the system was flushed, and all samples were weighed, dried, and prepared for particle size analysis. This procedure enables the creation of a size reduction curve versus a specific energy curve for the ore.

Grindability Studies using Ball Mill

The standard ball mill Bond Work Index (BWI) test was performed on Sample D. A modified ball mill BWI test was adopted for Samples A, B, and D to determine the specific energy consumption required for producing different target-sized milled products. Due to the fine nature of the asreceived material (Samples A, B, and C), a standard BWI test, which requires a feed crushed to minus 3.3 mm (6 mesh), could not be conducted. Therefore, a modified procedure was developed to create a suitable test feed. The bulk sample was first wet screened at 150 µm (100 mesh) to separate the coarse and fine fractions. The BWI test feed was then prepared by blending the screen oversize material with a small, controlled amount (500 grams) of the 150 µm screen undersize. This was done to simulate the effect of imperfect classification in a plant setting, where some fine material is always present in the mill feed. This non-standard feed preparation resulted in the test being performed on only a fraction of the original sample. Consequently, the "raw" BWI value calculated directly from the grinding test had to be mathematically adjusted. A correction factor, based on the mass proportion of the material used to create the test feed relative to the original sample, was applied to the initial result to derive a final, estimated BWI that was representative of the total composite material.

Liberation - Grinding Studies

The goal of magnetic separation testing was to further characterize the composite samples by determining their response to conventional magnetic separation techniques using a low-intensity magnetic field and to obtain baseline product quality data. Magnetic separation testing was conducted on both the as-received sample and various milled products. The grinding was carried out for different time intervals (3, 6, 9, and 12 minutes) in a small batch liberation ball mill and subjected to particle size analysis and magnetic separation in a Davis Tube Tester (Model: Davis Tube Tester OTB-602, Eriez, supplied). For each test condition, ten measurements were taken, and the average results were used for analysis. The magnetic and non-magnetic samples from each experiment are subjected to chemical analysis to understand the separation efficiency and liberation. The experimental procedure for liberation studies using Davis Tube Tester is illustrated in **Figure 6**.

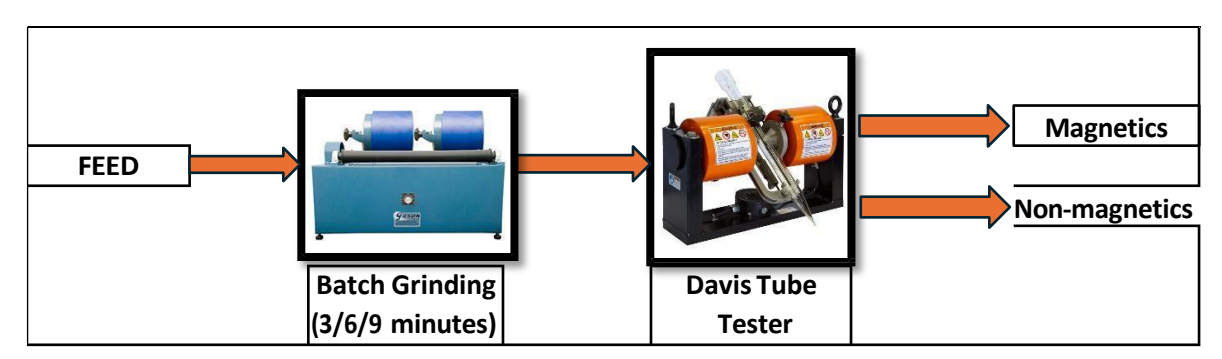


Figure 6. Experimental procedure for Liberation studies using Davis Tube Tester.

Low Intensity Magnetic Separation (Bench-Scale)

Bench-scale Low-Intensity Magnetic Separation (LIMS) tests were conducted to evaluate the samples' amenability to magnetic concentration. The experiments utilized a Stearns Magnetics (Model # 124-MS1005-1) electro-magnetic wet drum separator featuring a 30.5 cm by 38.1 cm drum, a concurrent tank design, and a maximum field intensity of 1260 Gauss (**Figure 7**).

The experimental procedure involved a double magnetic pass configuration to maximize the recovery of magnetic minerals. To specifically understand the separation behavior of magnetite, tests were performed at single and two-stage (magnetic field) with two distinct magnetic field intensities: a high setting of 1260 Gauss and a lower setting of 600 Gauss. The LIMS configuration for both single and double stages is shown in **Figure 8**. During each run, the feed slurry was maintained at 25% solids by weight, with additional flush water used to clean the concentrate. Following separation, the magnetic concentrate and non-magnetic tailings were collected, dried, and submitted for detailed chemical analysis of major and minor elements.



Figure 7. Wet low-intensity magnetic separator at NRRI.

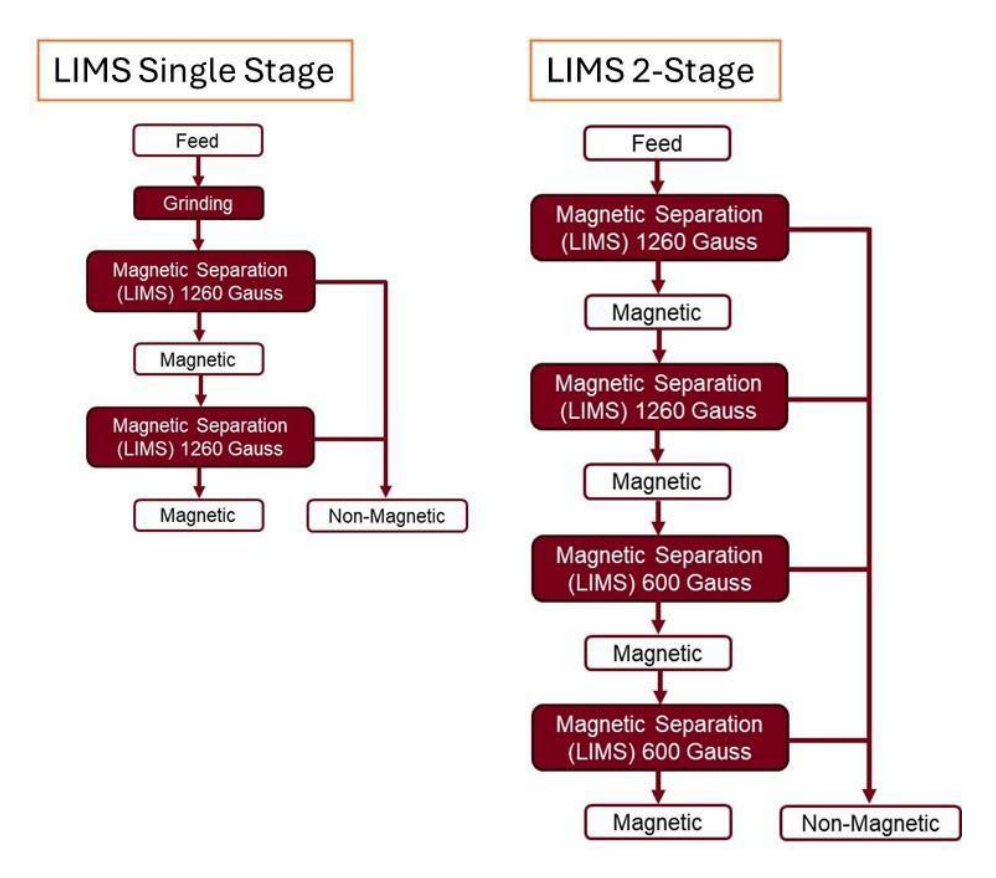


Figure 8. LIMS configuration considered for the present study.

Froth Flotation (Bench-Scale)

Bench-scale froth flotation tests were performed for both BF concentrates samples (Sample A and C) to evaluate the separation efficiency of the ore using a laboratory-scale Denver D12 mechanical cell, which was equipped with a 2 L tank and operated with natural air aspiration (**Figure 9**). The experimental program was designed to investigate the effects of collector dosage (at two levels) and particle size (at three levels) on silica flotation efficiency. For all tests, Evonik M100-7 was used as the collector, and MIBC was used as a frother. All other process parameters were kept constant, and their values are highlighted in **Table 2**. Additionally, an attempt was made to understand the separation efficiency when pre-concentrating the feed prior to flotation using a two-stage LIMS. The detailed test conditions, along with the results, will be discussed in the subsequent sections.

The procedure systematically evaluated two primary variables: the collector dosage was varied at two levels, while the feed particle size was tested at three different levels. Following each test, the resulting iron concentrate (underflow) and tailings (froth) were collected, dried, and weighed. Representative sub-samples were then prepared for chemical analysis to determine their grade and recovery. The specific parameters for each test are detailed alongside the results in subsequent sections.



Figure 9. Flotation experimental set-up at NRRI.

Table 2. Experimental and process conditions considered for the flotation tests.

Parameters	Process Conditions	
Collector	TOMAMINE M100-7	
Frother	MIBC	
Collector dosages	125 g/t	
Frother dosage	10 g/t	
рН	Natural	
Stages of flotation	5 (25 g/t each)	
Water	Coleraine, Minnesota, Tap water	
Slurry conditioning speed	1200 Rpm	
Slurry conditioning	2 minutes	
Collector conditioning	1 minute	
Frother conditioning	1 minute	
Flotation time	10 minutes total (2 minutes each stage)	
Air flowrate	100% open, naturally aspirated	

Results and Discussion

Characterization Results

The physical, chemical and mineralogical characterization was conducted on the four as-received samples as described in the Experimental Methods section. The description of the four samples can be found in **Table 3**.

Table 3. Sample details used in the project.

Sample Description	Sample Designate
Central Mesabi Flotation Feed	Sample A
Central Mesabi Rod Mill Feed	Sample B
Western Mesabi Plant Concentrate	Sample C
Western Mesabi SAG Mill Discharge	Sample D

Particle Size and Density Distribution

The as-received sample and the crushed sample (Sample B) were subjected to standard sieve analysis using the ASTM sieve series (**Figure 10. Particle** size distribution of four samples used in this project. The plots show that Samples A, C, and D are fine powders, with most of their particles smaller than 100 μ m; Sample D is the finest overall. In stark contrast, Sample B, a rod mill sample, is a much coarser material with particle sizes measured in mm. Key parameters (**Table 4**) include particle size data, where the D₅₀ and D₈₀ values indicate the point at which 50% and 80% of the material is passed through a given sieve. The data shows that Samples A and C are fine powders and similar, whereas Samples B and D are coarser due to being crude ore samples.

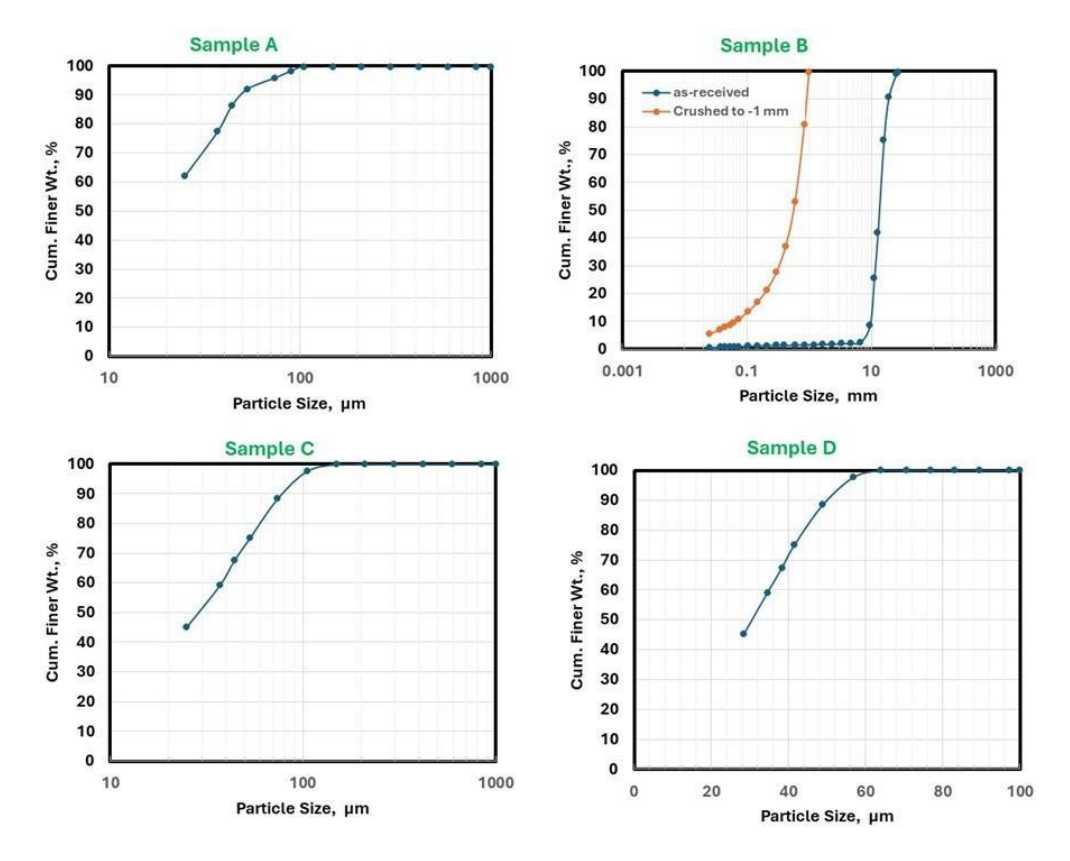


Figure 10. Particle size distribution of four samples used in this project.

Sample Details D_{80} (µm/mm) D_{50} (µm/mm) Sample A 39.0 µm 15.5 µm Sample B (As-received) 16.8 mm 13.5 mm Sample B (Crushed) 834.4 µm 563.5µm 29.2 µm Sample C 60.8 µm Sample D 360.6 µm 78.2 µm

Table 4. Sample details used in the project.

Similarly, the apparent density/specific gravity as well as the bulk density of the as-received samples were determined (**Table 5**). The specific gravity of pure magnetite is approximately 5.15 g/cm³, and high-grade magnetite ore typically has a specific gravity in the range of 4.8 to 5.1. The measured specific gravities for Sample A (4.87) and Sample C (4.89) fall squarely within this range, strongly suggesting they are composed of dense magnetite. In contrast, the lower specific gravity of Samples B and D (3.35) indicates that they are composed of a higher proportion of waste/gangue rock (gangue minerals such as silica or carbonates) and a significantly lower concentration of magnetite. The bulk densities further support this, with the denser, magnetite-rich samples (A and C) showing higher bulk densities than their less dense counterparts. Based on these results, Samples A and C are consistent with magnetite concentrate, while Samples B and D are typical taconite ore from the Mesabi Range.

Samples	Specific Gravity	Bulk Density (g/cc)
Sample A	4.87	2.14
Sample B	3.35	1.96
Sample C	4.89	2.31
Sample D	3.35	2.17

Table 5. Specific gravity and bulk density of the samples.

Magnetic Property Evaluation

Magnetic properties were evaluated using a Satmagan analyzer and calibrated with magnetite (**Table 6**). Further, oxidation ratios were calculated using the formula below.

Oxidation Ratio (%) =
$$100\% \times \frac{SatMagan (\%)}{Total Iron (Fe \%)}$$

The hysteresis curve was generated for a better understanding of the magnetic properties of these samples, and the curves were generated by applying a magnetic field strength up to 3 Tesla at room temperature. VSM analysis (**Figure 11**) reveals that the four taconite samples are primarily magnetite-based but differ significantly in their grade and mineralogical purity. Samples A and C show the highest saturation magnetization ($M_s \approx 7.2$ EMU), indicating a high concentration of magnetic material consistent with high-grade ore. In contrast, Sample B has the lowest grade ($M_s \approx 1.2$ EMU), while Sample D is a medium-grade ore ($M_s \approx 2.6$ EMU). The mass saturation magnetization of Samples A and C is higher than 93 EMU/g, which is as pure as magnetite crystal, reported to be approximately 92 EMU/g (Cullity et al., 2011).

Table 7 shows magnetic iron content, clearly separating the samples into two distinct groups. Samples A and C are high grade, with a high magnetite content of approximately 67% and a nearly complete oxidation ratio, indicating the iron content of the material is nearly all magnetite.

Table 6 Results	of the Satmagan	analysis of the samples.
I UNIC O. I COOUICO	or the odthiagan	andigolo of the barripico.

Samples	Satmagan (%)	Oxidation ratio (%)
Sample A	67.40	98.7
Sample B	19.41	62.3
Sample C	66.73	99.1
Sample D	20.08	66.5

Sample	Saturation Magnetization (M _s)	Remanent Magnetization (M _r)	Coercivity (H□)	Inference w.r.t. magnetite
А	~ 7.2 EMU	~ 0.2 EMU		High-grade, magnetically soft
В	~ 1.2 EMU	~ 0.1 EMU		Low-grade, magnetically soft
С	~ 7.2 EMU	~ 0.2 EMU		High-grade, mixed soft & hard phases
D	~ 2.6 EMU	~ 0.4 EMU		Medium-grade, magnetically harder

Table 7. Key magnetic properties from the hysteresis curve.

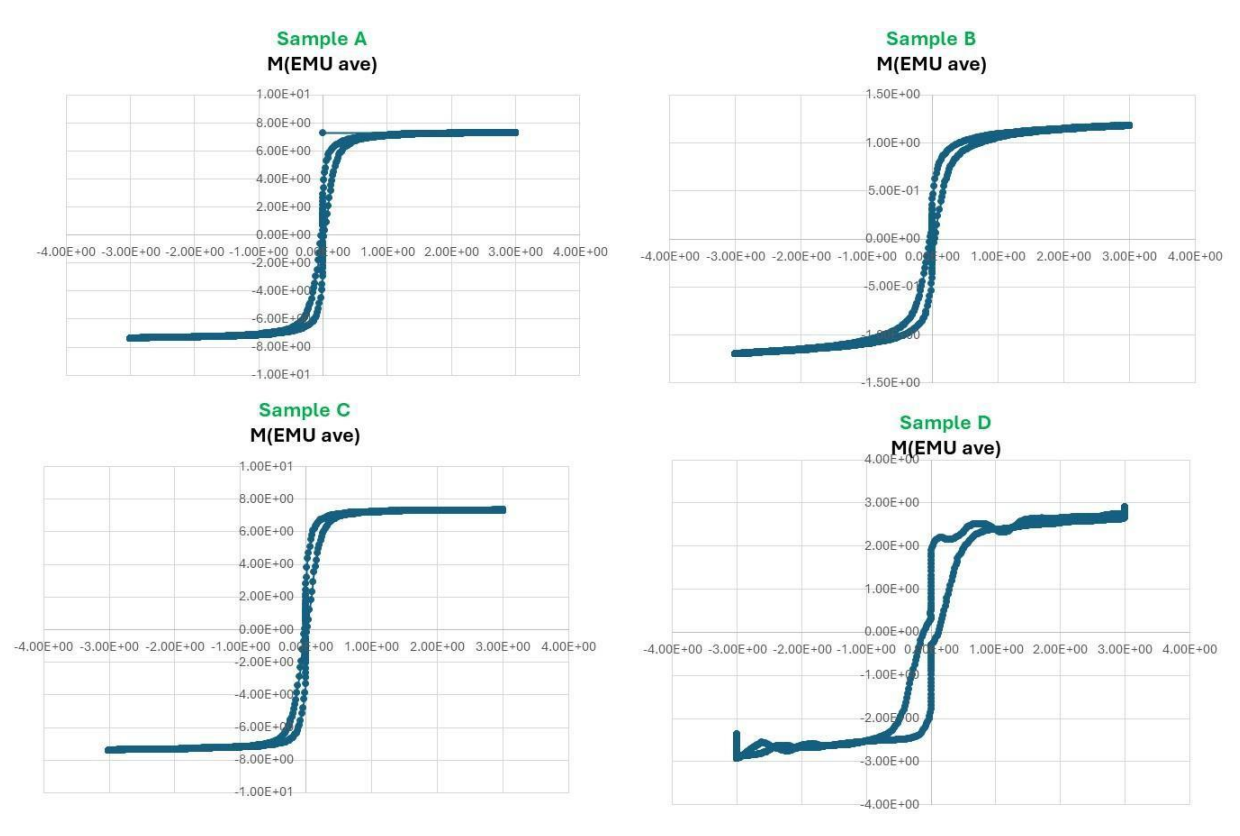


Figure 11. Hysteresis curve measured at room temperature for the as-received samples.

The initial mass magnetic susceptibility, calculated from the slope of the M-H curve, provides a clear measure of each sample's response to a magnetic field, directly correlating with its grade and magnetic hardness. Samples A and C show the highest susceptibility (approximately 0.06 EMU/Oe), indicating a strong magnetic response characteristic of high-grade, soft magnetite. In contrast, Sample B has the lowest susceptibility (approximately 0.01 EMU/Oe), a weak response consistent with its very low magnetite content. Sample D's moderate susceptibility (approximately 0.02 EMU/Oe) is lower than the high-grade samples because its magnetically harder nature resists changes in magnetization, resulting in a less steep initial slope.

Chemical Analysis

Chemical analysis of the as-received sample was initially carried out in-house (**Table 8**). This chemical analysis separates the samples into two distinct groups: Samples A and C are iron concentrates with high total iron (~67% Total Fe) and low impurities (~5%). In contrast, Samples B and D are taconite ores with low iron and high gangue content, and their positive Loss on Ignition (LOI) indicates the presence of volatile components, such as carbonates or hydroxide minerals. This contrasts with the negative LOI in A and C, which indicates the oxidation of magnetite during heating.

Camples							Assay V	/alue, %)					
Samples	Fe _(t)	SiO ₂	Al ₂ O ₃	CaO	MnO	MgO	TiO ₂	V ₂ O ₅	Na ₂ O	K ₂ O	Р	С	S	LOI
Sample A	67.82	4.49	BDL	0.2	0.12	0.3	0.01	BDL	BDL	0.017	0.009	0.17	0.006	-2.61
Sample B	31.18	48.79	0.3	1.47	0.6	2.38	0.02	BDL	0.012	0.08	0.021	1.0	0.009	2.64
Sample C	67.37	5.16	BDL	0.28	0.1	0.46	0.008	BDL	BDL	0.011	0.009	0.25	0.008	-2.25
Sample D	30.19	48.45	0.22	1.63	0.46	3.17	0.01	BDL	BDL	0.048	0.016	1.3	0.02	3.71

Table 8. Chemical analysis of as-received iron ore samples analyzed at NRRI.

BDL: Below detection level (Al₂O₃: 0.04%; V₂O₅: 0.09%; Na₂O: 0.006%)

LOI: Loss on Ignition at 950 °C

To analyze trace elements and metals, samples were sent to ALS Global, Reno, Nevada for detailed analysis (Appendix B), which revealed a clear correlation between the ore grade and the concentration of impurities. The high-grade concentrates (Samples A and C) contain low levels of minor, gangue-related elements such as Al₂O₃, CaO, MgO, and SiO₂. Conversely, the lower-grade mill feeds are enriched in these minor elements and also contain significantly higher concentrations of various trace elements, including barium (Ba) and moderate levels of critical elements/metals.

Size-wise Chemical Analysis

For a better understanding of the elemental distribution, size-wise analysis was carried out, with the results shown in **Table 9** to **Table 12**. **Table 9** shows that the chemical analysis of different particle size fractions of sample A follows a clear trend, where the material purity increases as the particle size decreases. The finest fraction (-25 μ m) contains the highest total iron (~70%) and the lowest total impurities (~3%), indicating that the valuable iron mineral is progressively liberated from the silica-rich waste rock in finer sizes. This conclusion was supported by the increasingly negative Loss on Ignition (LOI) values, which signify a higher concentration of magnetite, and a similar trend was observed in Sample C (**Table 10**).

Table 11 shows that for Sample B, the sample grade does not significantly improve with decreasing particle size until the material is very fine. Across the coarser and intermediate-sized fractions (from 410 down to $74\mu m$), the total iron (Fe_T) and gangue content remain relatively constant at approximately 30–33% and 45–55%, respectively. Only in the finer fractions below 74 μm do we see a slight increase in iron content, which then unexpectedly drops in the finest fraction

 $(-25 \mu m)$, suggesting the valuable mineral is not well liberated from the waste rock until extensive grinding is performed.

The chemical analysis of different particle size fractions of Sample D (**Table 12**) reveals that the sample grade remains consistent across a wide range of sizes and does not exhibit significant improvement with grinding. The total iron (Fe_T) content remains low, ranging from 27–36%, while the gangue content stays high at approximately 45–55% across nearly all fractions. This indicates that the valuable iron mineral is not effectively liberated from the silica-rich waste rock, even at finer sizes, and the unexpected drop in iron grade in the finest (-25 μ m) fraction suggests a complex mineralogy.

Table 9. Size-wise chemical analysis of Sample A.

Comples		Assay Value, %												
Samples	Fe _(t)	SiO ₂	Al ₂ O ₃	CaO	MnO	MgO	TiO ₂	V_2O_5	Na ₂ O	K₂O	Р	С	S	LOI
+74	54.01	20.25	0.12	0.9	0.98	0.35	0.015	BDL <	BDL	0.042	0.02	0.61	0.016	-0.19
-74+44	64.9	7.65	0.05	0.43	0.49	0.2	0.011	BDL	BDL	0.02	0.015	0.32	0.011	-1.9
-44+37	67.34	5	BDL	0.28	0.34	0.14	0.01	BDL	BDL	0.015	0.012	0.23	0.009	-2.39
-37+25	69.21	3.12	BDL	0.18	0.23	0.1	0.009	BDL	BDL	0.008	0.01	0.15	0.007	-2.68
-25	69.73	2.46	BDL	0.1	0.22	0.07	0.009	BDL	BDL	0.011	0.008	0.1	0.005	-2.89

BDL: Below detection level (Al₂O₃: 0.04%; V₂O₅: 0.09%; Na₂O: 0.006%)

LOI: Loss on Ignition at 950 °C

Table 10. Size-wise chemical analysis of Sample C.

Samples		Assay Value, %												
Samples	Fe _(t)	SiO ₂	Al ₂ O ₃	CaO	MnO	MgO	TiO ₂	V ₂ O ₅	Na ₂ O	K ₂ O	Р	С	S	LOI
+74	60.08	20.25	0.12	0.9	0.98	0.35	0.015	BDL	BDL	0.042	0.02	0.61	0.016	-0.19
-74+44	66.67	7.65	0.05	0.43	0.49	0.2	0.011	BDL	BDL	0.02	0.015	0.32	0.011	-1.9
-44+37	68.7	5	BDL	0.28	0.34	0.14	0.01	BDL	BDL	0.015	0.012	0.23	0.009	-2.39
-37+25	69.38	2.46	BDL	0.1	0.22	0.07	0.009	BDL	BDL	0.011	0.008	0.1	0.005	-2.89
-25	68.44	3.12	BDL	0.18	0.23	0.1	0.009	BDL	BDL	0.008	0.01	0.15	0.007	-2.68

BDL: Below detection level (Al₂O₃: 0.04%; V₂O₅: 0.09%; Na₂O: 0.006%)

LOI: Loss on Ignition at 950 °C

Assay Value, % **Samples** CaO MnO Р C S SiO₂ Al_2O_3 MgO TiO₂ V_2O_5 Na₂O K₂O LOI Fe_(t) 2.26 + 841 30.52 49.65 0.28 1.4 0.59 0.02 BDL 0.015 0.085 0.021 0.97 0.001 2.78 -841+595 30.82 49.65 0.27 1.41 0.59 2.24 0.018 **BDL** 0.014 0.083 0.02 0.99 0.002 2.75 -595+420 0.28 1.41 2.22 BDL 0.082 0.02 0.97 2.76 29.82 50.21 0.57 0.018 0.013 0.01 -420+297 30.04 49.67 0.3 1.48 0.59 2.29 0.019 **BDL** 0.013 0.084 0.02 1.01 0.003 2.87 -297+210 30.32 0.35 1.54 2.44 2.78 49.91 0.61 0.022 BDL 0.013 0.085 0.021 0.97 0.002 48.25 2.51 0.022 2.69 -210+149 30.94 0.36 1.58 0.023 BDL 0.014 0.96 0.013 0.6 0.09 -149+74 33.07 45.51 0.35 1.61 0.59 2.57 0.023 **BDL** NA NA NA 0.95 0.016 2.61 2.43 2.26 -74+44 35.22 43.37 0.32 1.58 0.58 0.021 BDL 0.014 0.075 0.018 0.93 0.014 -44+25 36.4 42.06 0.33 1.53 0.57 2.15 0.021 BDL 0.015 0.069 0.016 0.91 0.012 2.05

Table 11. Size-wise Chemical Analysis of Sample B.

BDL: Below detection level (Al₂O₃: 0.04%; V₂O₅: 0.09%; Na₂O: 0.006%)

0.47

48.69

28.72

LOI: Loss on Ignition at 950 °C; NA: Not analyzed due to insufficient sample volume

1.81

0.71

3.82

Table 12. Size-wise Chemical Analysis of Sample D.

0.027

BDL

0.015

0.096

0.026

1.23

0.015

3.83

Commiss							Assay V	alue, %)					
Samples	Fe _(t)	SiO ₂	Al ₂ O ₃	CaO	MnO	MgO	TiO ₂	V ₂ O ₅	Na ₂ O	K ₂ O	Р	С	S	LOI
+ 841	27.55	50.98	0.18	1.8	0.49	2.78	BDL	BDL	0.013	0.047	0.014	1.42	0.015	4.54
-841+595	27.74	50.98	0.19	1.82	0.5	2.79	0.006	BDL	0.012	0.047	0.014	1.44	0.014	4.52
-595+420	27.75	50.42	0.19	1.75	0.5	2.81	0.007	BDL	0.013	0.052	0.015	1.46	0.016	4.5
-420+297	27.42	51.16	0.21	1.77	0.51	2.87	0.007	BDL	0.013	0.053	0.015	1.49	0.02	4.55
-297+210	27.3	51.16	0.23	1.73	0.52	2.94	0.008	BDL	0.013	0.055	0.016	1.46	0.022	4.55
-210+149	28.04	50.29	0.23	1.68	0.51	2.94	0.009	BDL	0.012	0.052	0.016	1.43	0.023	4.41
-149+105	30.73	47.03	0.2	1.55	0.46	2.78	0.009	BDL	0.012	0.046	0.014	1.32	0.025	3.65
-105+74	34.15	43.66	0.18	1.38	0.41	2.5	0.008	BDL	0.011	0.043	0.014	1.23	0.025	2.92
-74+53	35.61	42.5	0.16	1.27	0.37	2.24	0.007	BDL	0.009	0.036	0.012	1.13	0.024	2.35
-53+44	36.12	42.64	0.15	1.19	0.35	2.09	0.007	BDL	0.009	0.034	0.011	1.04	0.022	2.1
-44+37	35.69	43.19	0.14	1.18	0.36	2.05	0.007	BDL	0.009	0.032	0.012	1.02	0.021	2.1
-37+25	34.76	44.74	0.14	1.2	0.36	1.99	0.008	BDL	0.008	0.031	0.011	1.02	0.02	2.16
-25	27.55	50.98	0.18	1.8	0.49	2.78	BDL	BDL	0.013	0.047	0.014	1.42	0.015	4.54

BDL: Below detection level (Al₂O₃: 0.04%; V₂O₅: 0.09%; Na₂O: 0.006%)

LOI: Loss on Ignition at 950 °C; NA: Not analyzed due to insufficient sample volume

X-ray Diffraction (XRD) Results

X-ray diffraction (XRD) analysis for the as-received sample **Figure 12** to **Figure 15** revealed the mineral composition of the four samples, and clearly separated them into two distinct groups. The patterns for Samples A and C are dominated by intense peaks corresponding to magnetite (Fe_3O_4) , with only a minor amount of quartz (SiO_2) and other impurities present, indicating that both are magnetite concentrates. Conversely, the patterns for Samples B and D show the opposite, with very strong quartz peaks and only minor peaks for magnetite, indicating they are silica-rich crude ore. The other minerals present in these samples include hematite, a secondary iron mineral. The other major gangue minerals in these samples were minnesotaite and talc, with minor mineral phases including apatite, dolomite, ankerite, siderite, greenalite, stilpnomelane, and chromite.

Further, the semi-quantification of mineral phases via Rietveld refinement (**Table 13**) indicates that Samples A and C are magnetite concentrates, with magnetite (Fe_3O_4) as the dominant phase (87.5% and 82.8%, respectively) and quartz as the primary impurity. In contrast, Samples B and D are crude ores, with Sample D being predominantly quartz (57.7%) and Sample B being a complex mixture containing significant amounts of quartz, minnesotaite, and various carbonate minerals.

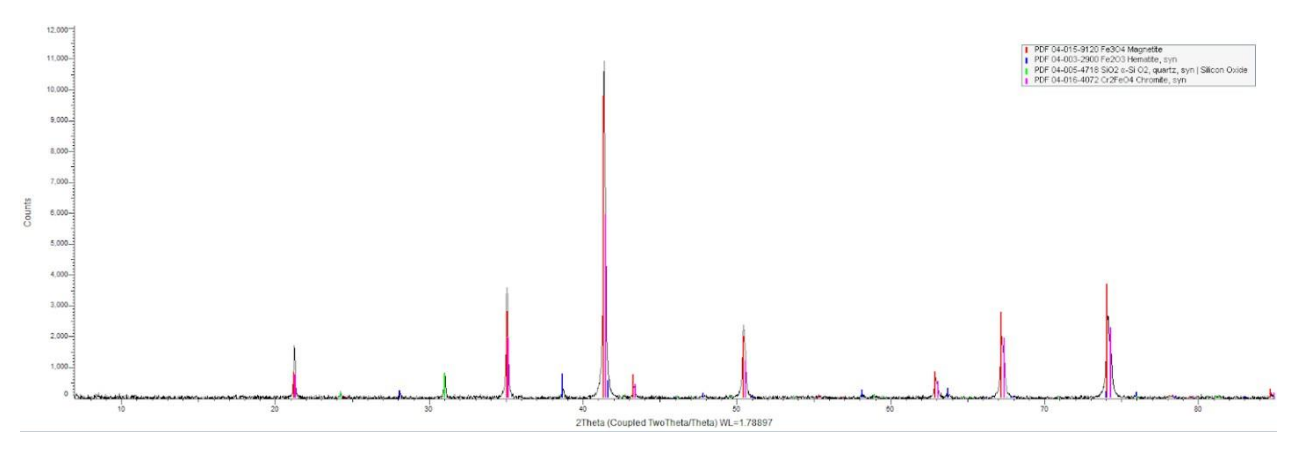


Figure 12. X-ray diffraction pattern of as-received Sample A.

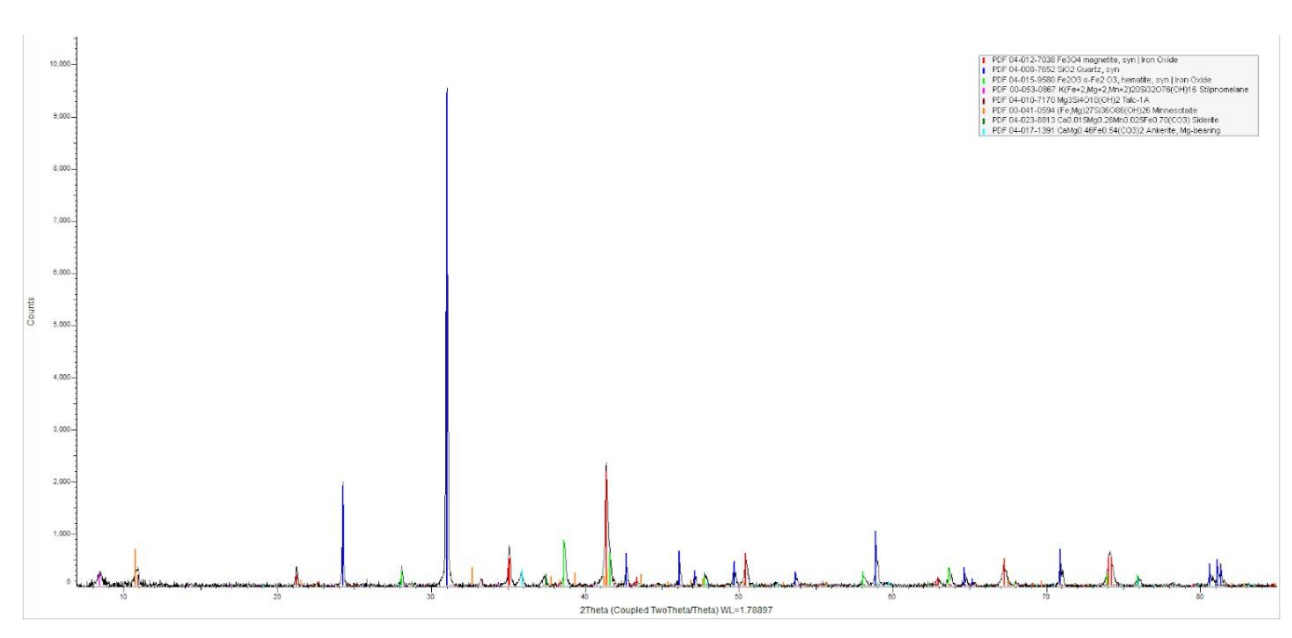


Figure 13. X-ray diffraction pattern of as-received Sample B.

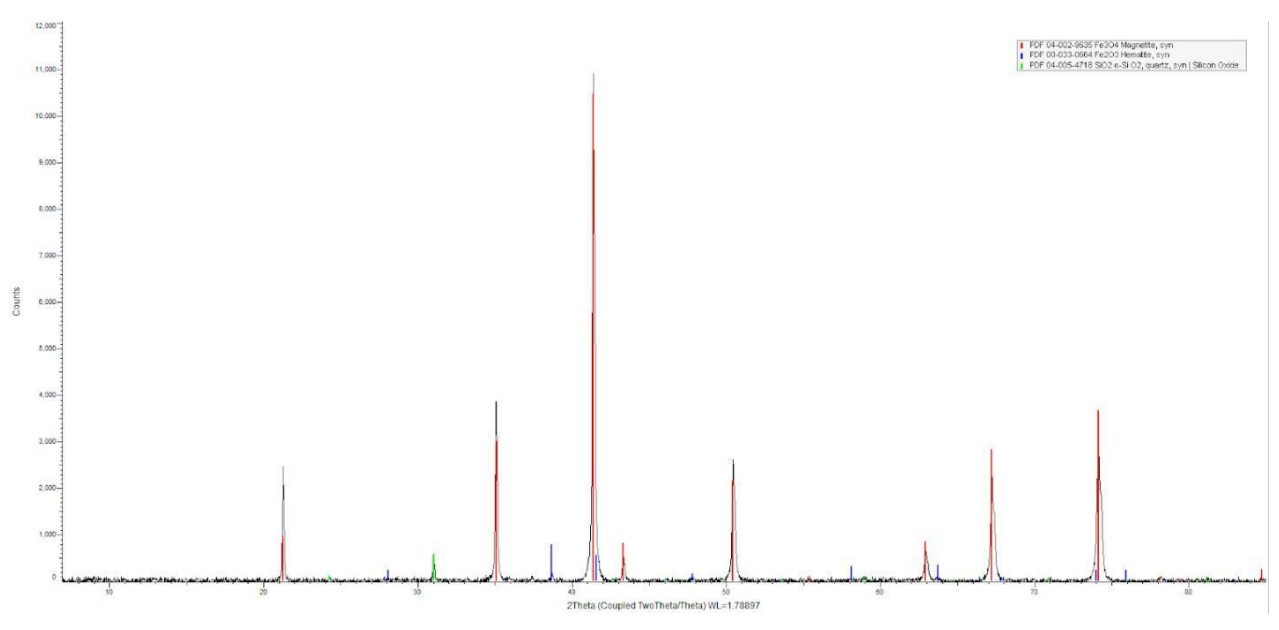


Figure 14. X-ray diffraction pattern of as-received Sample C.

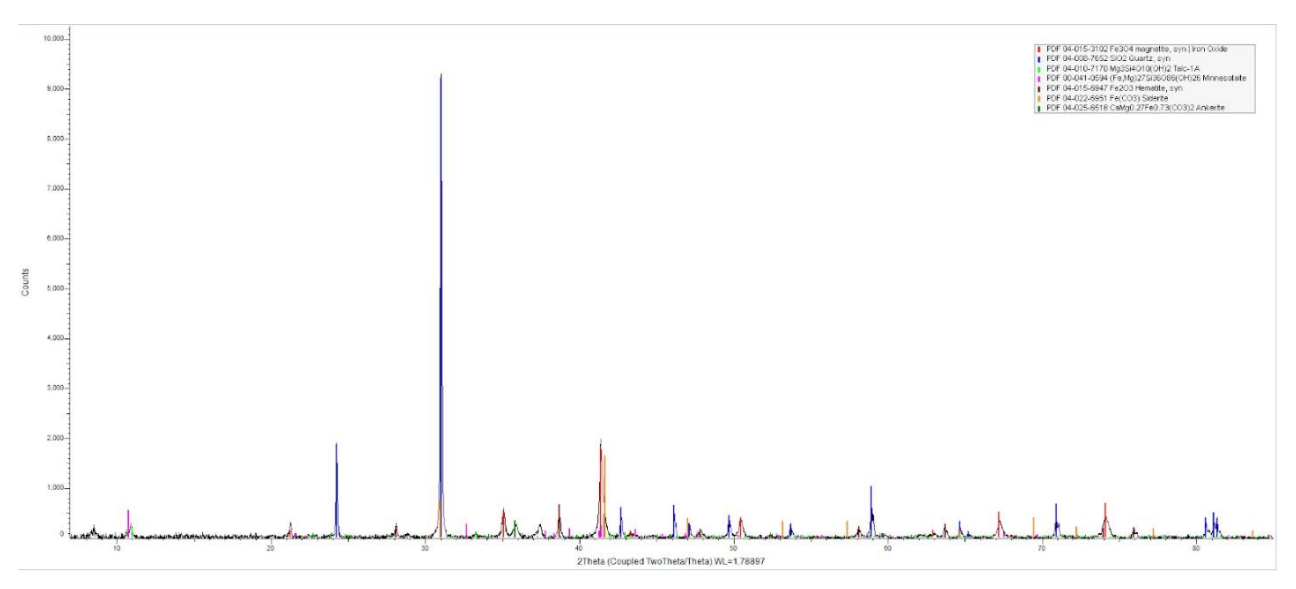


Figure 15. X-ray diffraction pattern of as-received Sample D.

Table 13. Semi-quantification of mineral phases by Rietveld refinement method.

Minonele	Obamical Famoula		Abundar	ice, wt.%	
Minerals	Chemical Formula	Sample A	Sample B	Sample C	Sample D
	Major Pha	ises			
Magnetite	Fe_3O_4	87.5	60.3	82.8	20.9
Hematite	Fe_2O_3	6.1	8.9	4.8	6
Quartz	SiO ₂	5.8	19.7	6.8	57.7
Minnesotaite	Fe ₃ Si ₄ O ₁₀ (OH) ₂		6	4.1	
Talc	Talc $Mg_3Si_4O_{10}(OH)_2$				6.8
	Minor Pha	ises			
Apatite	Ca ₅ (PO ₄) ₃ (OH,Cl,F)				4.9
Dolomite	CaMg(CO ₃) ₂				3.5
Ankerite	CaFe(CO ₃) ₂		2.6		
Siderite	FeCO ₃		2.1		
Greenalite	$(Mg_3Si_2O_5(OH)_4)$	0.2		0.2	
Stilpnomelane	$(K(Fe^{2+},Mg,Fe^{3+})_8(Al,Si)_{12}(O,OH)_{27} $ $nH_2O)$				0.3
Chromite	ite FeCr ₂ O ₄			1.3	

The XRD analysis was carried out for different size fractions of these four samples (**Table 14** to **Table 17**), revealing distinct liberation characteristics. For Samples A and C, the concentration of magnetite dramatically increases in the finer size fractions, reaching over 90% in particles smaller than 37 μ m (400 mesh), while quartz, the main impurity, decreases, indicating excellent liberation of magnetite. In contrast, Samples B and D show poor liberation, as magnetite abundance remains low and quartz remains the dominant mineral across nearly all size fractions, with no significant grade improvement even after fine grinding.

Table 14. Size-wise XRD analysis and semi-quantification of mineral phases in Sample A.

Cita fraction um		Abı	undance, wt.%	
Size fraction, µm	Magnetite	Hematite	Quartz	Talc / Minnesotaite
+53	49	12.1	31.7	7.2
-53+44	69.2	11.7	11.5	7.6
-44+37	80.8	11.1	8.2	
-37+25	91.7	4.2	4	
-25	93	4.9	2.1	

Table 15. Size-wise XRD analysis and semi-quantification of mineral phases in Sample B.

			Ak	oundance, wt.%			
Size fraction, µm	Magnetite	Hematite	Quartz	Talc/ Minnesotaite	Ankerite	Dolomite	Pyrite
+ 841	17.3	10.9	64.1	5.4		2.3	
-841+595	18	11.2	65.4	5.3			
-595+420	17	10.7	66.8	5.5			
-420+297	17	10.6	65.6	6.8			
-297+210	17.7	9.7	62.4	6.6	3.6		
-210+149	18.4	9.5	60.2	8.2	3.7		Trace
-149+74	22	9.3	55.4	9.4	3.9		Trace
-74+44	23.2	9.5	54	8.8	4		0.4
-44+25	25.9	9.2	53.9	7	4		0.1
-25	16.1	8.7	50.7	19.9	4.5		0.1

Table 16. Size-wise XRD analysis and semi-quantification of mineral phases in Sample C.

Size fraction, µm		Abundance, wt.%											
Oize maction, pin	Magnetite	Hematite	Quartz	Talc	Greenalite	Ankerite	Siderite						
-74	68.5	6.7	17.6	4.8			2.4						
-74+44	84.9	3	7.1	2.7	8.0	1.5							
-44+37	92.6	2.7	4.8										
-37+25	92.6	3.9	3.5										
-25	90.7	5.2	4.1										

Table 17. Size-wise XRD analysis and semi-quantification of mineral phases in Sample D.

0:			Ab	undance, wt.%		
Size fraction, µm	Magnetite	Hematite	Quartz	Talc / Minnesotaite	Ankerite	Siderite
+ 841	16.3	6.6	62.3	7.6	4.3	2.9
-841+595	16.9	6.4	61.3	7.6	4.7	3.1
-595+420	16.4	6	61.7	7.4	4.8	3.6
-420+297	16.4	6.4	61.9	7.1	4.6	3.6
-297+210	15.2	7	61.2	8.5	4.6	3.6
-210+149	16.8	6.3	59.4	9.1	4.5	3.9
-149+105	20.5	6.2	57.6	7.3	4.7	3.7
-105+74	24.9	5.7	54.8	8	3.6	3
-74+53	27.3	5.2	52.4	8.7	3.9	2.6
-53+44	27.8	5.1	54.7	6.4	3.5	2.6
-44+37	27.7	4.3	53.2	8.3	3.7	2.8
-37+25	30.9	3.2	56.3	4	3	2.5
-25	17.7	3.9	42.9	27.5	4.6	3.4

Electron Probe Micro-Analysis Results

The Electron Probe Micro-analysis (EPMA) study was designed to conduct a detailed mineralogical and chemical characterization of the taconite samples at a microscopic level. The analysis involved creating elemental maps to visualize the spatial distribution of elements within particles and performing point analysis to determine the precise chemical composition of the different mineral phases present. A primary objective is to use this data to establish a geochemical correlation with reference to magnetite to determine the concentration of impurity elements within the magnetite mineral. To investigate how properties change with particle size, the study was conducted on the sample after it was split into two distinct size fractions: a coarser fraction with a particle size of +25 μ m (+500 mesh) and a finer fraction with a particle size of -25 μ m (-500 mesh).

Appendix C explains the EPMA scatter plot, which provides a microscopic chemical analysis, showing the relationship between iron (Fe) and silica (Si) content at hundreds of individual points on the ore particles. Detailed correlations are further discussed in Appendix C.

For better visualization, the silica content in the magnetite grain is evaluated statistically and interpreted in the sample as a composite (**Table 18**). Additionally, silicon distribution in magnetite grains derived from EPMA point analysis was plotted for quantification (**Figure 16**), illustrating the purity distribution of magnetite grains within the taconite ore by plotting the cumulative mass percentage of magnetite against its internal silica (SiO₂) content. The curve shows that approximately 65% of the total magnetite mass is of high purity, containing less than 0.8% SiO₂. As the silica content increases, the curve rises steeply, indicating that the remaining 35% of the magnetite mass contains progressively higher levels of silica impurities. This analysis is crucial for understanding the ore's liberation characteristics, as it quantifies the extent to which the valuable magnetite is contaminated with finely intergrown or substituted silica. Additionally, it was evident that less than 25% of the magnetite mass has less than 0.1% Si contamination.

 Table 18. Summary of the point analysis of magnetite in Sample C.

Si Content Range (% Si)	+ 25 µm (Wt.%)	- 25 μm (Wt.%)	Composite (Wt.%)
≤ 0.1 % Si	25	18.8	23.1
0.1 – 0.2 % Si	25	22.5	24.2
0.2 – 0.3 % Si	18.75	15.0	17.6
0.3 – 0.4 % Si	12.5	12.5	12.5
0.4 – 0.5 % Si	10	8.8	9.6
> 0.5 % Si	8.75	22.5	13.0

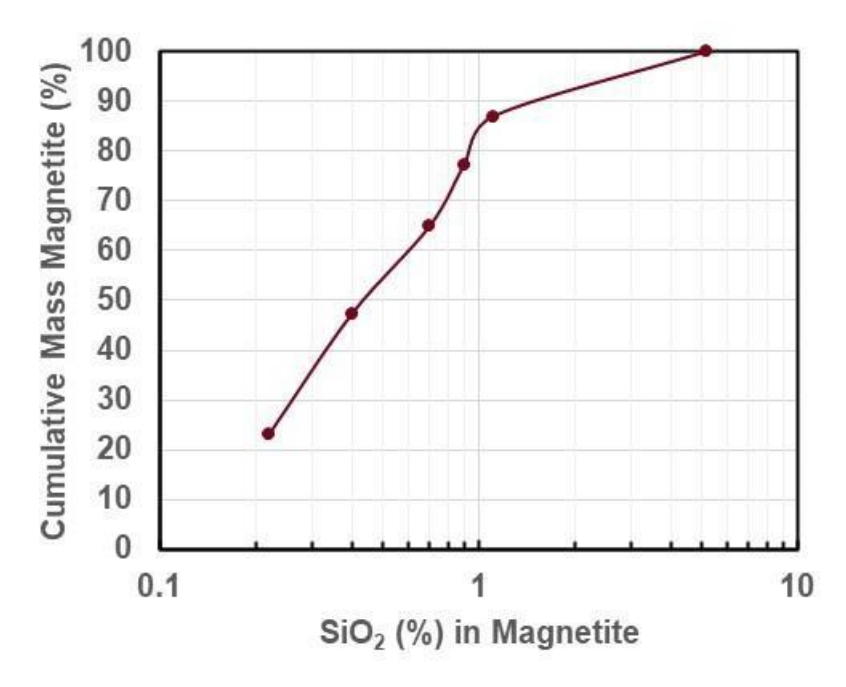


Figure 16. Silicon deportment in magnetite grains in Sample C.

Further, the distribution of titanium (Ti), zinc (Zn), manganese (Mn), calcium (Ca), magnesium (Mg), sodium (Na), potassium (K), phosphorous (P), sulfur (S), and chlorine (Cl) as trace impurities within the taconite ore, based on microscopic EPMA data, were analyzed (Appendix C).

Table 19 summarizes the preceding geo-chemical and micro-chemical analyses of various elemental impurities within the taconite ore. Silicon (Si) is the primary impurity and exists in a separate quartz phase that dilutes the magnetite, as shown by its strong negative correlation with iron. Manganese (Mn) is the only element that clearly substitutes for iron directly within the magnetite crystal lattice. Other elements like titanium (Ti), calcium (Ca), phosphorus (P), and sulfur (S) exist as distinct micro-inclusions of different minerals (ilmenite, carbonates, apatite, and sulfides, respectively) within the ore.

Table 19. Summary of the geo-chemical correlations and behavior.

Element	Relevance to Magnetite	Approx. Max. Concentration	Geochemical Behavior
Silicon (Si)	Primary Impurity	1.0%	Shows a strong negative correlation with Fe, indicating it is from a separate silicate (quartz) phase diluting the magnetite.
Manganese (Mn)	Substitution	0.035%	Shows a positive correlation with Fe, indicating it substitutes for iron directly within the magnetite crystal lattice.
Titanium (Ti)	Internal Inclusion	0.035%	Has no correlation with Fe but a negative one with Si, indicating it's in separate micro-inclusions (ilmenite) within the magnetite.
Magnesium (Mg)	Complex	0.04%	Highly scattered, suggesting a mix of minor substitution for Fe and presence in separate silicate micro-inclusions.
Calcium (Ca)	External Inclusion	0.095%	Highly scattered with no correlation to Fe or Si, indicating it's in separate carbonate micro-inclusions.
Sodium (Na)	External Inclusion	0.09%	Highly scattered with no correlation to Fe or Si, indicating it's in separate silicate (feldspar/amphibole) micro-inclusions.
Potassium (K)	External Inclusion	0.05%	Highly scattered with no correlation to Fe or Si, indicating it's in separate silicate (feldspar/mica) micro-inclusions.
Zinc (Zn)	External Inclusion	0.035%	Highly scattered with no correlation to Fe or Si, indicating it's in separate sulfide (sphalerite) microinclusions.
Phosphorus (P)	External Inclusion	0.04%	Highly scattered with no correlation to Fe or Si, indicating it's in separate phosphate (apatite) microinclusions.
Sulfur (S)	External Inclusion	0.04%	Highly scattered with no correlation to Fe or Si, indicating it's in separate sulfide (pyrite) microinclusions.
Chlorine (CI)	Trace Fluid/Contaminant	0.045%	Highly scattered with no correlation to Fe or Si, suggesting it is trapped in fluid inclusions or is a processing artifact.

Electron Probe Micro-Analysis Results - Mineral Analysis

Several images were processed using Energy-Dispersive X-Ray Spectroscopy (EDS), analyzing over 100 points on each sample. Typical data was chosen for further visualization and interpretation. **Figure 17** show a Backscattered Electron (BSE) image from an Electron Probe Micro-analysis (EPMA) of a polished cross-section of the taconite ore particles. In this type of image, the brightness of each mineral corresponds to its average atomic number, allowing for the clear identification of different phases. In this ore, the bright white grains are magnetite (Fe_3O_4), as iron is the heaviest major element present, and the dark gray particles are minerals with a lower average atomic number, corresponding to silicates and other gangue minerals, such as quartz (SiO_2). The black areas are the epoxy resin used to mount the polished particles for analysis. The red numbered spots (1 through 15) indicate the precise locations where further EDS chemical analysis was performed, providing their exact elemental composition. This allows us to confirm the identity of the minerals, quantify impurities within a single grain, and identify microscopic inclusions.

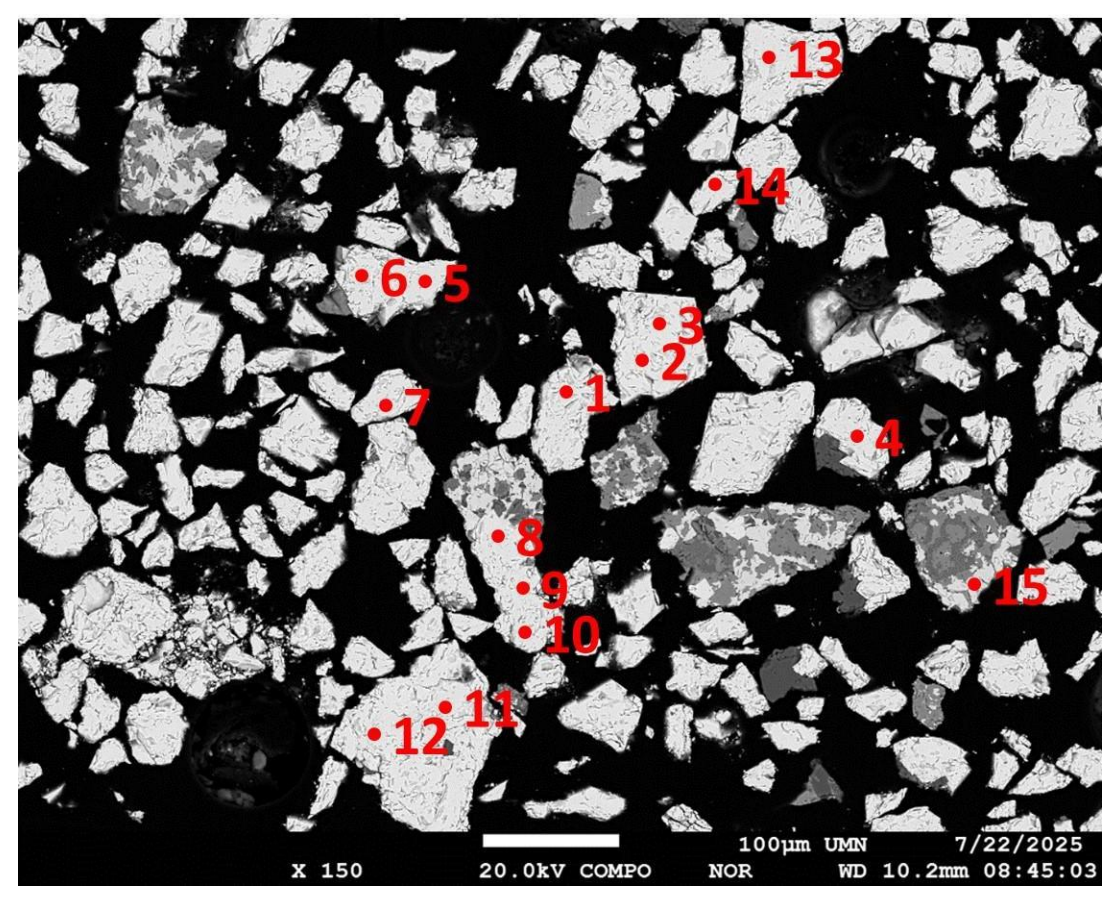


Figure 17. Backscattered image (BSE) of particles of coarser size fraction (+25 μm) of Sample C.

Table 20 summarizes EMPA point analysis of the BSE image shown in **Figure 17**, confirming the identity of the primary minerals based on their appearance and chemical signature. The bright white, angular particles with very high iron content (~71.4–71.9% Fe) are identified as pure magnetite, while the dark grey particles with high silica content are confirmed to be quartz. The analysis also reveals the nature of impurities and incomplete liberation, showing that some magnetite grains contain elevated titanium (as titaniferous magnetite or ilmenite micro-inclusions) or have silicate micro-inclusions containing aluminum, potassium, and sodium. Finally, the study identifies un-liberated particles, where an intermediate iron and silica signature confirms that magnetite and quartz are still physically locked together.

Analysis Point #	Micrograph Appearance	Key Chemical Signature	Identified Mineral
8, 9, 10, 11, 12	Bright White, angular	Very high Fe (71.4 – 71.9%), low Si	Magnetite (Fe ₃ O ₄)
3, 6	Dark Gray, irregular	Very high Si, high O, low Fe	Quartz / Chert (SiO ₂)
1, 5, 13, 14	Bright White	High Fe, but also elevated Ti	Titaniferous Magnetite or Magnetite with Ilmenite (FeTiO ₃) micro-inclusions
2, 4	Bright White	High Fe, but also elevated Al, K, Na	Magnetite with attached silicate micro- inclusions (e.g., feldspar)
15	Intergrown Bright & Gray	Intermediate Fe and Si	An un-liberated particle of intergrown Magnetite and Quartz

Table 20. Summary of EPMA point analysis of the image depicted in Figure 17.

Some particles were selected to investigate the inclusion of different elements in the magnetite. **Figure 18** provides a detailed micro-analysis of magnetite particles in the taconite ore, combining a micrograph (BSE image) with elemental analysis to identify specific minerals at a microscopic scale. This micro-analysis identifies the primary iron mineral as pure magnetite (Fe_3O_4), based on its characteristic iron and oxygen signature. The study also characterizes the nature of the associated gangue and impurity minerals, identifying complex silicate inclusions containing silicon, manganese, and iron (likely minnesotaite). Furthermore, the analysis reveals the presence of trace impurities, such as very small iron-nickel sulfide inclusions, identified as pentlandite. Results illustrated in **Figure 18** can be summarized as follows:

- The feed sample is primarily magnetite and quartz. Trace elements are hosted in various micro-inclusions, with manganese substituting for iron in magnetite and elements like sulfur and nickel residing in separate sulfide mineral particles.
- The sample shows good liberation, with many individual particles of pure magnetite and pure quartz.
- There is clear evidence of interlocking, where particles consist of both magnetite and quartz. These composite grains are the main reason for the residual silicon impurity in the magnetite concentrate

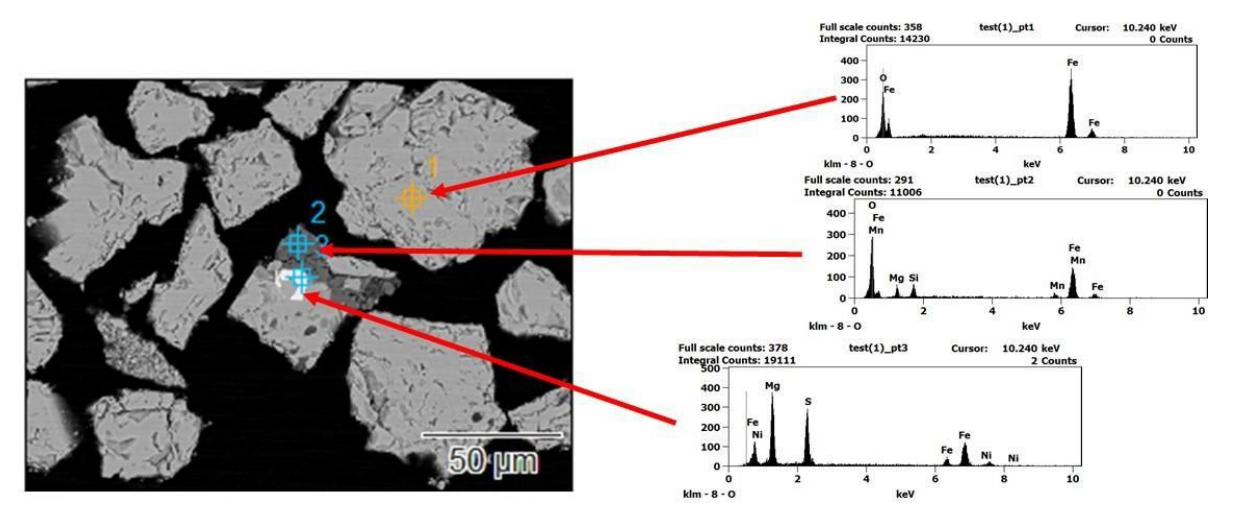


Figure 18. EPMA analysis of magnetite particles along with EDS data.

Some particles were selected for the point analysis, and the micrograph along with EDS analysis is shown in **Figure 19**. The micro-analysis provides a detailed identification of the various mineral phases present in the taconite ore. The EPMA data confirms that the bright white particles (Points 1, 4, 6) are high-purity magnetite, with an iron content very close to its theoretical value. The dark grey particles (Points 2, 5) are confirmed to be quartz, which is the primary silica gangue. The analysis of the intermediate-grey, un-liberated phases (Points 3, 7, 8) identifies them as complex iron-rich silicates like minnesotaite or stilpnomelane, which also contain manganese (Mn) substituting for iron. This characterization effectively distinguishes between the liberated valuable minerals, the waste rock, and the complex, intergrown silicate gangue. The following observations are summarized.

- The presence of particles where magnetite is physically interlocked with quartz and iron silicates is the main barrier.
- Elements like manganese are chemically locked within the magnetite crystal structure and cannot be removed by physical means

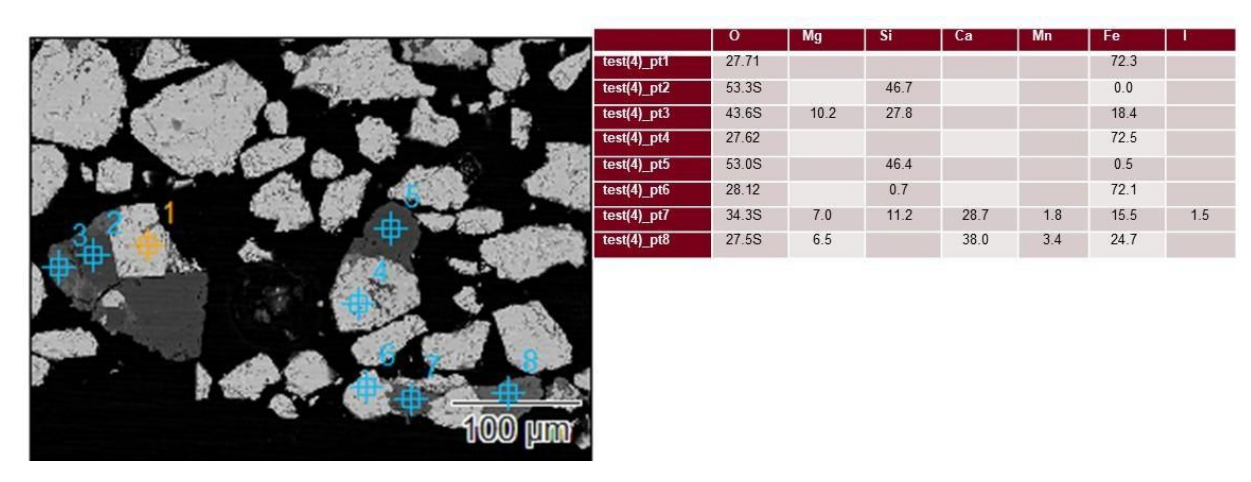


Figure 19. EPMA analysis of magnetite and other associated particles along with EDS data.

Electron Probe Micro-Analysis Results – Elemental Mapping

EPMA elemental maps (**Figure 20**) provide a powerful visual representation of how different elements are distributed across the ore particles, complementing the previous point analysis by showing the texture and association of the minerals. The analysis confirms a clear separation between the valuable iron and the gangue elements. These elemental maps visually confirm the findings from the point analysis:

- The ore consists of well-defined magnetite and quartz particles, along with complex silicate gangue minerals containing magnesium and manganese that are intergrown with the primary ore.
- Among minerals, magnetite, quartz, and iron-silicate (rich in Mg and Mn) are prominent. These particles are well-liberated particles of both magnetite and quartz.
- The Mn and Mg contamination in the magnetite may not be from substitution within the magnetite itself but from these complex iron-silicate minerals, such as: stilpnomelane/ minnesotaite, that are physically interlocked with the magnetite.

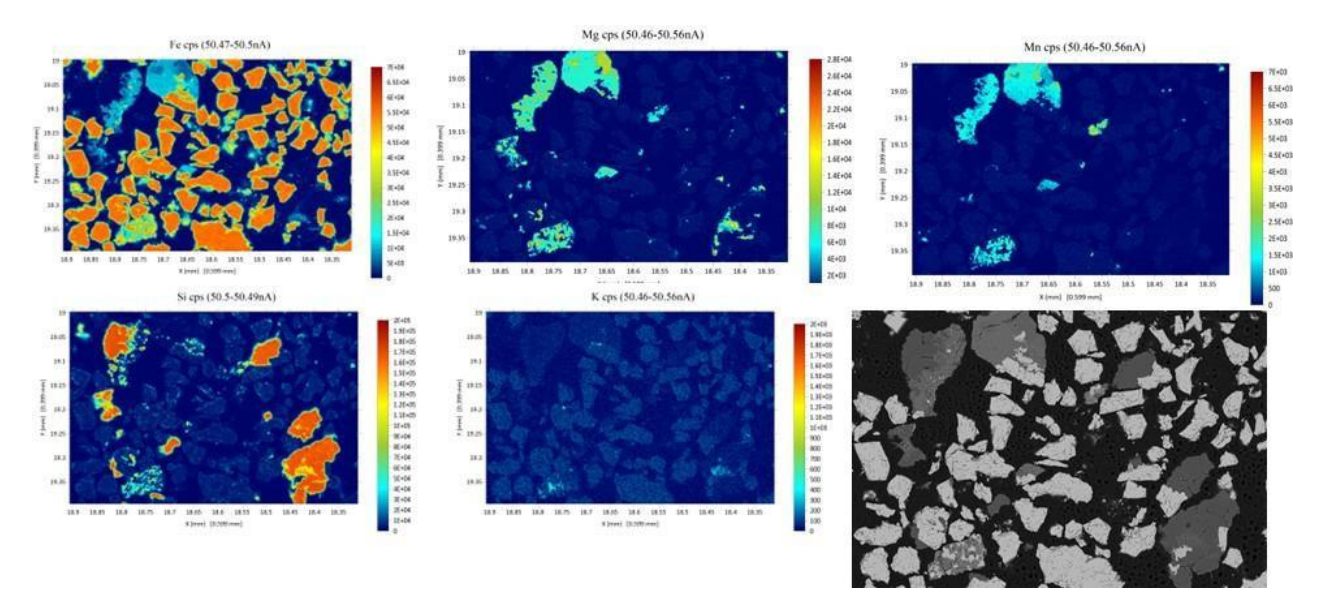


Figure 20. Elemental mapping 1 of particles of Sample C.

A second EPMA map series (**Figure 21**) shows that iron is confined to the bright magnetite grains, while the silicon (Si) map highlights the separate quartz and silicate particles. The maps visually confirm that while many particles are liberated (either pure magnetite or pure quartz), some are complex intergrowths where the two are in close contact. The maps for magnesium (Mg), manganese (Mn), and calcium (Ca) are particularly insightful, revealing that these elements are not trace impurities spread throughout the ore but are major components of specific complex gangue minerals. All three elements are shown to be concentrated together in the same large, multi-phase particles (the intermediate-grey grains in the reference image). In summary:

• EPMA maps powerfully illustrate the nature of the un-liberated particles in this ore, showing that the main challenge in mineral processing is the separation of magnetite from complex Ca-Mg-Mn-Fe silicate gangue minerals.

• The mapping envisaged on the abundance of fully liberated, high-purity magnetite particles and interlocked particles of magnetite physically fused with an iron-silicate mineral (stilpnomelane, minnesotaite, ankerite).

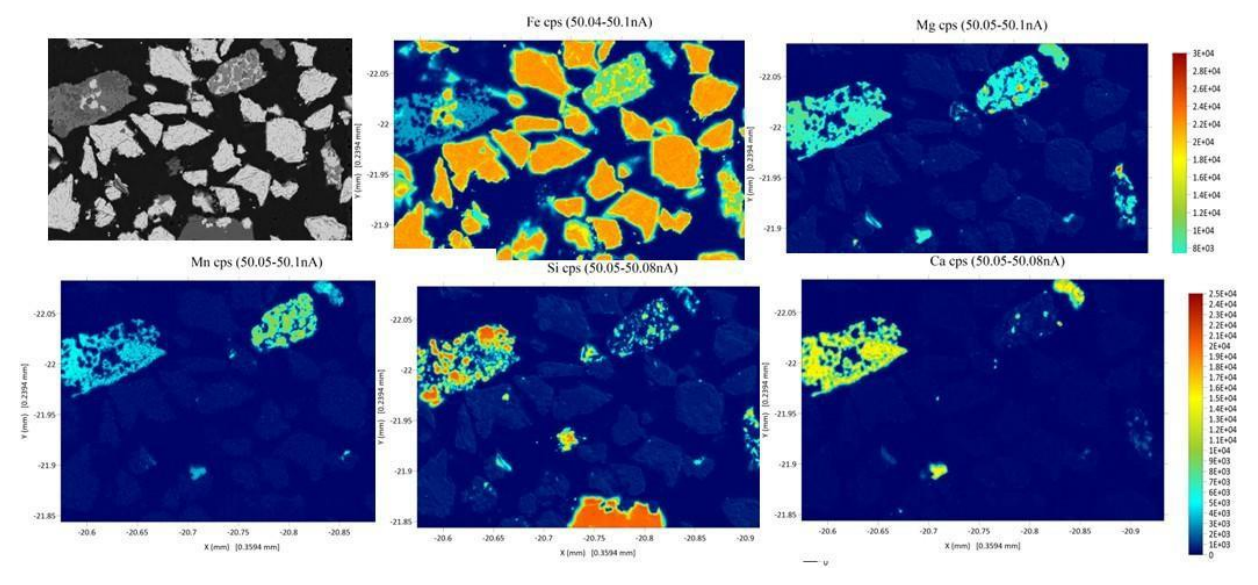


Figure 21. Elemental mapping 2 for particles of Sample C.

Electron Probe Micro-Analysis Results – Summary

Table 21 summarizes data from the EPMA studies on the correlation and role of different elements in magnetite separation. The ore consists primarily of magnetite (Fe_3O_4) as the host mineral for iron (Fe), with quartz (SiO_2) being the main impurity. These two minerals are physically separate, requiring fine grinding for liberation, as shown by the clear mixing line between pure magnetite and quartz in chemical scatter plots. The behavior of other elements is more complex; manganese (Mn) exhibits dual behavior, both substituting for iron within the magnetite lattice and acting as a major component in separate silicate gangue minerals. Magnesium (Mg), however, does not substitute for iron and is found exclusively as an external inclusion, hosted in distinct silicate and carbonate grains where it is often co-located with manganese and calcium.

Table 21. Summary of EPMA analysis of Sample C.

Element (Symbol)	Role / Relevance to Magnetite	Approx. Max. Concentration (Wt %)	Geochemical Behavior
Silicon (Si)	Primary Impurity	1.0%	Shows a strong negative correlation with Fe, indicating it is from a separate silicate (chert) phase diluting the magnetite.
Manganese (Mn)	Substitution	0.035%	Shows a positive correlation with Fe, indicating it substitutes for iron directly within the magnetite crystal lattice.
Titanium (Ti)	Internal Inclusion	0.035%	Has no correlation with Fe but a negative one with Si, indicating it's in separate micro-inclusions (ilmenite) within the magnetite.
Magnesium (Mg)	Complex Outsider	0.04%	Highly scattered, suggesting a mix of minor substitution for Fe and presence in separate silicate micro-inclusions.
Calcium (Ca)	External Inclusion	0.095%	Highly scattered with no correlation to Fe or Si, indicating it's in separate carbonate micro-inclusions.
Sodium (Na)	Outsider (External Inclusion)	0.09%	Highly scattered with no correlation to Fe or Si, indicating it's in separate silicate (feldspar/amphibole) microinclusions.
Potassium (K)	Outsider (External Inclusion)	0.05%	Highly scattered with no correlation to Fe or Si, indicating it's in separate silicate (feldspar/mica) micro-inclusions.
Zinc (Zn)	Outsider (External Inclusion)	0.035%	Highly scattered with no correlation to Fe or Si, indicating it's in separate sulfide (sphalerite) micro-inclusions.
Phosphorus (P)	Outsider (External Inclusion)	0.04%	Highly scattered with no correlation to Fe or Si, indicating it's in separate phosphate (apatite) micro-inclusions.
Sulfur (S)	Outsider (External Inclusion)	0.04%	Highly scattered with no correlation to Fe or Si, indicating it's in separate sulfide (pyrite) micro-inclusions.
Chlorine (CI)	Trace Fluid/Contaminant	0.045%	Highly scattered with no correlation to Fe or Si, suggesting it is trapped in fluid inclusions or is a processing artifact.

Beneficiation Results

Liberation and Magnetic Separation Results

The liberation grinding studies were carried out with as-received material as well as grinding at different size intervals (3, 6, and 9 minutes) in a ball mill. The key results of the particle size distribution are given in **Figure 22** and **Figure 23** for Samples A and C, respectively. **Figure 22** and **Figure 23** show the particle size distribution for Samples A and C after different grinding intervals, revealing a significant difference in their grinding characteristics. For both samples, increasing the grinding time from as-received to 9 minutes grinding time effectively reduced the overall particle size, shifting the distribution curves to the finer size. However, the comparison

shows that Sample A grinds much finer than Sample C. This indicates that Sample A is softer and has a higher grindability, producing a finer product with the same amount of grinding effort.

For better understanding, the D_{80} of the size distribution for each test are given in **Table 22**, which confirms that the particle size (D_{80}) of both consistently decreased with increased grinding time. The data clearly show that Sample A is significantly finer than Sample C at every stage; it starts finer (40 µm vs. 58.9 µm) and remains much finer after 9 minutes of grinding (20.3 µm vs. 39.4 µm). For both samples, the most effective size reduction occurs within the first 3 minutes, indicating that Sample A has a higher overall grindability. Specific energy consumption (S_E) was determined using an advanced grinding mill (stirred media mill). It was found that the S_E for Sample A was 20.5 kWh/t while reducing the particle size from 67µm to 32µm. Similarly, the measured S_E value for Sample C is 14 kWh/t for grinding particle size from 39µm to 12µm.

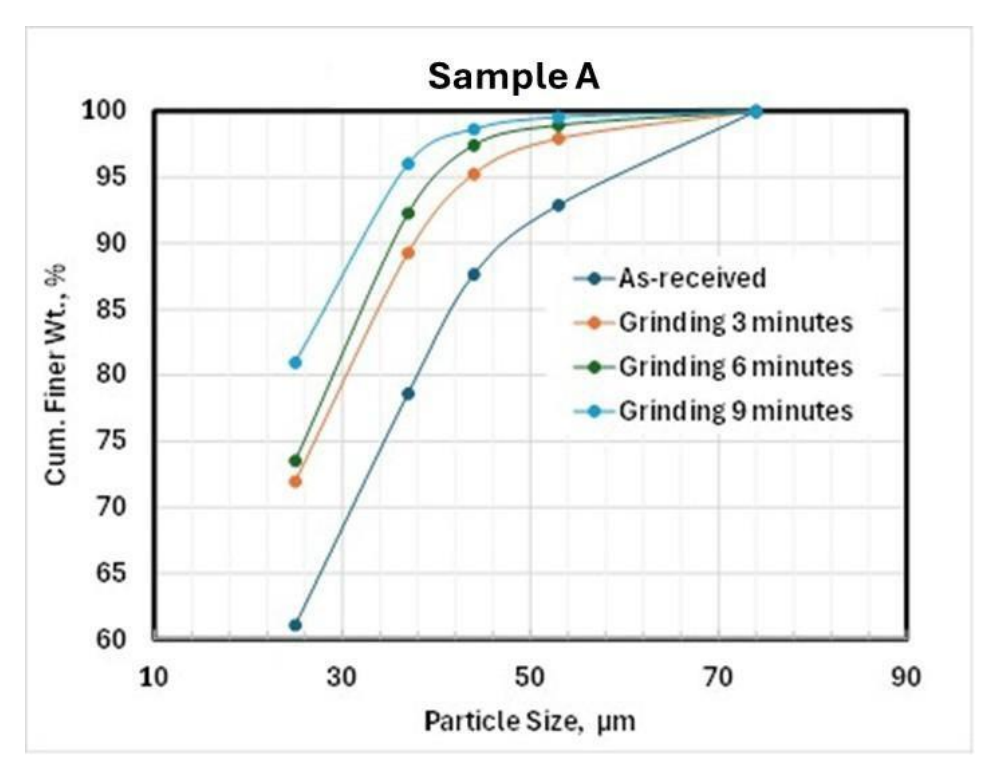


Figure 22. Particle size distribution of the mesh of grind studies at three different grinding intervals for Sample A.

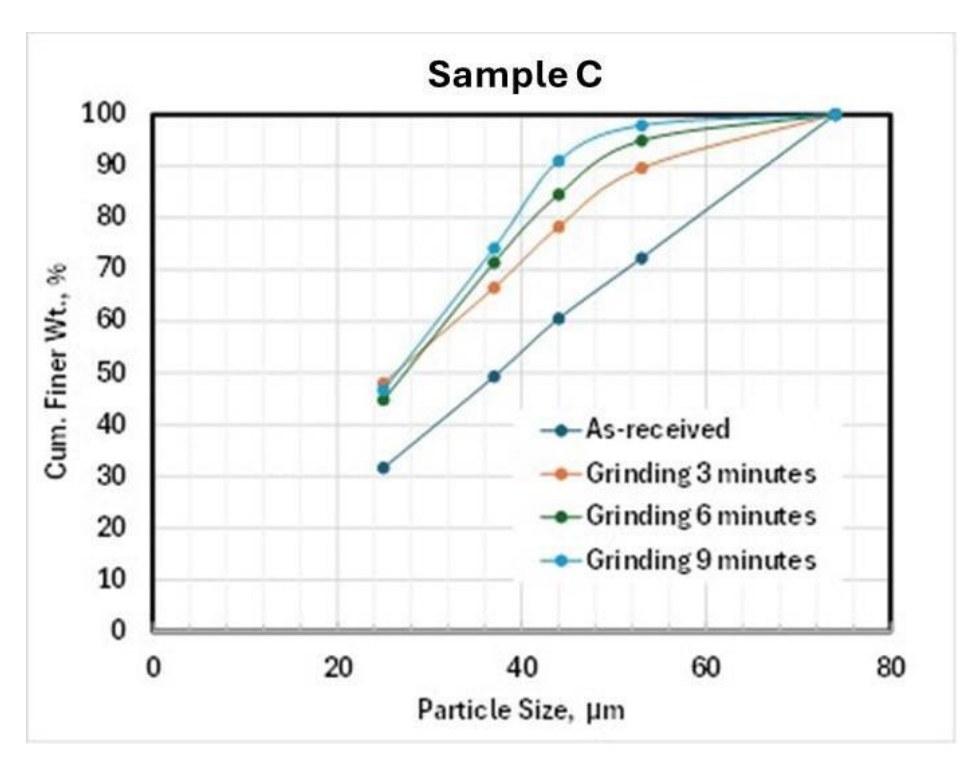


Figure 23. Particle size distribution of the mesh of grind studies at three different grinding intervals for Sample C.

Sample As-received Grinding 3 minutes Grinding 6 minutes	D ₈₀ (μm)									
Sample	Sample A	Sample C								
As-received	40 µm	58.9 µm								
Grinding 3 minutes	26.1 µm	45.4 µm								
Grinding 6 minutes	24.2 µm	41.6 µm								
Grinding 9 minutes	20.3 μm	39.4 µm								

Table 22. Results on particle size of milled samples.

Magnetic separation results in the Davis Tube Tester indicate that grinding enhances mineral liberation, improving product quality. Three-batch liberation grinding followed by Davis Tube magnetic separation was carried out, and the average values were considered for discussion, highlighted in **Table 23** and **Table 24**. Due to the lower volume of the non-magnetic fraction, it was not subjected to chemical analysis. Compared to the feed grade of Fe_(t): 67.82% for Sample A (**Table 23**), the magnetic fraction after grinding for 9 minutes showed a notable enrichment in Fe_(t) to 71.12% and a reduction in other gangue components, indicating efficient gangue rejection. The saturation magnetization (SatMag) values increased with the grinding time, which confirms the improvement in the liberation of magnetite particles in the sample. However, the weight recovery of the magnetic fraction slightly decreased (from 98.9.7% to 95.9%) with longer grinding, reflecting a trade-off between grade and yield.

Similarly, magnetic separation using the Davis Tube Tester was studied for Sample C and the results in **Table 24** show that grinding effectively improves the grade of the magnetic concentrate by removing gangue impurities. As grinding time increased to 9 minutes, the total iron content

(Fe(t)) increased from 70.14% to 70.98%, while the gangue content decreased significantly from 2.5% to 1.5%. A key finding is that the Satmagan value remains constant at a very high 71.37% across all grinding intervals, indicating that the magnetic mineral itself is nearly pure magnetite. Therefore, the benefit of grinding this sample is not to improve the quality of the magnetite, but it may be applicable to other iron-bearing minerals.

Table 23. Results of the Davis Tube tests at different grinding times for Sample A.

	Mass				Assay V	'alue (%)				Satmagan			
	pull, wt%	Fe _(t)	SiO ₂ ,%	Al_2O_3	CaO	MgO	MnO	TiO ₂	V_2O_5	(%)			
As-received	98.9	69.1	3.41	BDL	0.18	0.2	0.09	0.009	BDL	68.6			
Grinding at 3 min	96.3	70.34	1.81	BDL	0.11	0.13	0.06	0.009	BDL	70.6			
Grinding at 6 min	95.2	70.86	1.77	BDL	0.09	0.1	0.05	0.009	BDL	71.1			
Grinding at 9 min	95.9	71.12	1.21	BDL	0.08	0.09	0.05	0.009	BDL	71.2			
Feed Sample		67.82	4.49	BDL	0.2	0.12	0.3	0.01	BDL	66.9			
	BDL: Below detection level (Al ₂ O ₃ : 0.04%; V ₂ O ₅ : 0.09) *SatMagan: Saturation Magnetization calibrated with magnetite (71.37% Fe)												

Table 24. Results of the Davis Tube tests at different grinding times for Sample C.

	Mass		Assay Value (%)													
	pull, wt%	Fe _(t)	SiO ₂ ,%	Al_2O_3	CaO	MgO	MnO	TiO ₂	V_2O_5	(%)						
As-received	97.4	70.14	2.14	BDL	0.14	0.18	0.06	0.007	BDL	71.37						
Grinding at 3 min	95.9	70.34	1.92	BDL	0.11	0.16	0.05	0.007	BDL	71.37						
Grinding at 6 min	95.8	70.74	1.61	BDL	0.08	0.12	0.04	0.006	BDL	71.37						
Grinding at 9 min	96.0	70.98	1.29	BDL	0.07	0.1	0.03	0.006	BDL	71.37						
Feed Sample		67.35	5.08	BDL	0.28	0.1	0.46	0.008	BDL	66.7						
BDL: Below detection	n level (Al ₂ O	3: 0.04%; \	/ ₂ O ₅ : 0.09)													
*SatMagan: Saturati	on Magnetiza	ation calibr	ated with m	agnetite (7	'1.37% Fe)											

Magnetic Separation using Low-Intensity Magnetic Separation (LIMS)

Magnetic separation was carried out in a single stage (with two magnetic pass configurations) at a magnetic field intensity of 1,250 Gauss, as well as double stages (with two magnetic pass configurations) with 1,260 and 600 Gauss. The feed rate and slurry pulp density were kept constant at 12 l/h and 25% solids w/w, respectively. The separation studies in LIMS were carried out by varying the particle size of the feed. The results of the as-received and ground to different sizes (D_{80} of 30 and 15 μ m) for Sample A are tabulated in **Table 25**.

As the ore is milled finer, from as-received down to 15 μ m, the iron grade (Fe_(t)) of the magnetic concentrate increases from 68.7% to 70.81%, while the silica impurity is significantly reduced from 3.88% to 1.52% SiO₂. This improvement in grades comes with a slight and acceptable decrease in iron recovery, which remains very high at 96.9% at the finest grind. The effectiveness of the process is best shown by the silica distribution, where grinding to 15 μ m allows for 68.5% of the total silica to be rejected to the non-magnetic tailings, compared to only about 16% in the as-received sample.

Similarly, sample C was subjected to a single-stage magnetic separation using LIMS (**Table 26**). As the ore is milled finer from as-received down to 15 μ m, the iron grade (Fe(t)) of the magnetic concentrate increases from 69.19% to 70.56%. More importantly, the gangue impurity is reduced drastically by more than 50% This substantial improvement in grade is achieved while maintaining an excellent iron recovery, which remains very high at 97.3% even at the finest grind. The effectiveness of fine grinding is best illustrated by the silica distribution: grinding to 15 μ m results in 73.5% of the total silica to be rejected to the non-magnetic tailings, a vast improvement over the 42.7% rejection in the as-received sample.

Table 25. Results on magnetic separation in a single-stage LIMS for Sample A

Products	Mass Pull						Ass	ay Value	e (%)						Distributi (%	ion Value %)
	(%)	Fe _(t)	SiO ₂	Al ₂ O ₃	CaO	MgO	MnO	TiO ₂	V ₂ O ₅	Na ₂ O	K ₂ O	Р	С	S	Fe _(t)	SiO ₂
								A	s-recei	/ed sam	ole					
Magnetics	97.53	68.7	3.88	0.09	0.26	0.27	0.13	0.011	BDL	BDL	0.012	0.008	0.14	0.008	98.80	84.28
Non-magnetics	2.47	37.38	35.1	0.5	1.71	2.86	0.88	0.044	BDL	0.013	0.012	0.047	1.39	0.027	1.20	15.72
								N	/lilled to	P ₈₀ 30 µ	ım					
Magnetics	94.21	70.39	1.92	BDL	0.1	0.15	0.07	0.009	BDL	BDL	0.01	0.006	0.08	0.006	97.78	40.29
Non-magnetics	5.79	28.39	35.1	0.41	2.34	2.77	1.02	0.033	BDL	0.012	0.095	0.055	1.66	0.034	2.22	59.71
								N	/lilled to	P ₈₀ 15 µ	ım					
Magnetics	92.8	70.81	1.52	BDL	0.07	0.11	0.05	0.009	BDL	BDL	0.011	0.005	BDL	0.004	96.9	31.5
Non-magnetics	7.2	29.02	44.28	0.38	2.41	2.86	1.01	0.035	BDL	0.014	0.098	0.07	1.59	0.033	3.1	68.5
BDL: Below Detection	Limit (Al ₂ O ₃ : 0.04%;	V ₂ O ₅ : 0.009	%; Na ₂ O:0.	006% C:0.	14%	•	•			•	•	•				·

 Table 26. Results on magnetic separation in a single-stage LIMS for Sample C.

Duadeseta	Mass						Ass	ay Value	(%)							oution e (%)
Products	Pull (%)	Fe _(t)	SiO ₂	Al ₂ O ₃	CaO	MgO	MnO	TiO ₂	V ₂ O ₅	Na ₂ O	K₂O	Р	С	S	Fe _(t)	SiO ₂
							As-rece	ved samp	ole							
Magnetics	95.44	69.19	3.1	BDL	0.19	0.27	0.08	0.007	BDL	BDL	0.007	0.008	NS	NS	98.02	57.34
Non- magnetics	4.56	27.4	45.14	0.33	2.23	3.71	0.72	0.02	BDL	0.01	0.069	0.037	1.9	0.033	1.98	42.66
							Milled to	Ρ ₈₀ 30 μ	m							
Magnetics	91.97	70.6	1.75	BDL	0.08	0.13	0.05	0.007	BDL	NS	NS	NS	NS	NS	96.38	31.19
Non- magnetics	8.03	26.29	45.07	0.31	2.66	3.8	0.88	0.028	BDL	0.012	0.063	0.051	NS	NS	3.62	68.81
							Milled to	Ρ ₈₀ 15 μ	m							
Magnetics	92.9	70.56	1.49	BDL	0.06	0.11	0.04	0.008	BDL	0.037	0.006	0.004	BDL	0.005	97.3	26.5
Non- magnetics	7.1	25.85	46.75	0.34	2.86	4.16	1.01	0.032	BDL	0.031	0.074	0.06	2.29	0.045	2.7	73.5
BDL: Below D	etection Lir	nit (Al ₂ O ₃ :	0.04%; V2	O5: 0.00	9%; Na2	O:0.006	% C:0.1	4%; NS: N	lot avail	able due	to insuffici	ent samp	le			

Further two stage magnetic separation for both samples was carried out at two different magnetic field strengths of 1,260 and 600 Gauss. The results of the separation for both the ores are tabulated in **Table 27** (Sample A) and **Table 28** (Sample C). By grinding the ore from as-received down to 15 μ m (P80), the final magnetic concentrate's iron grade (Fe_T) increases substantially from 68.84% to 71.02%. Concurrently, the silica impurity is drastically reduced, falling from 3.37% to 1.07%. Crucially, this significant upgrade in quality is achieved while maintaining a high iron recovery, which remained stable at 96.0% even at the finest grind. The effectiveness of the double-stage process is best demonstrated by the results of finer grinding to 15 μ m, after which only 21.6% of the total silica reports to the final concentrate, meaning nearly 80% is successfully rejected to the two non-magnetic tailings streams. Similarly, the single-stage LIMS separation of Sample C (**Table 28**), when milled to 15 μ m, yields a high-grade concentrate with an iron grade of 70.56% and an iron recovery of 97.3%. The final gangue (silica) grade in the concentrate is also low at 1.49%. The process effectively removes waste material by rejecting 73.5% of the total silica to the non-magnetic tailings.

The double-stage LIMS separation results for both Sample A and Sample C demonstrate that fine grinding to 15 µm is highly effective at producing a high-purity iron concentrate by rejecting a wide range of impurities. For Sample A, this process achieves an iron grade of 71.02% with a silica impurity of just 1.07%, while Sample C reaches an iron grade of 70.68% with 1.23% silica. Crucially, the process is also very efficient at rejecting other major gangue elements for both samples. For instance, in the final concentrate of Sample A, CaO is reduced to 0.06% and MgO to 0.08%. A similar strong rejection is seen in Sample C, where CaO drops to 0.04% and MgO to 0.09%. This significant purification is achieved while maintaining outstanding iron recoveries of 96.0% for Sample A and 96.9% for Sample C, indicating a highly efficient separation process for all major gangue components.

Table 27. Results on magnetic separation in a two-stage LIMS for Sample A.

Products	Mass Pull						Ass	say Value	: (%)							bution ie (%)
Floudets	(%)	Fe _(t)	SiO ₂	Al ₂ O ₃	CaO	MgO	MnO	TiO ₂	V ₂ O ₅	Na ₂ O	K₂O	Р	С	s	Fe _(t)	SiO ₂
							As-rece	ived samp	ole							
Magnetics	94.8	68.84	3.37	BDL	0.2	0.2	0.09	0.009	BDL	BDL	0.015	0.009	BDL	BDL	96.2	71.1
Non- magnetics 1	4.2	37.38	35.1	0.48	1.73	2.85	0.82	0.042	BDL	0.02	0.127	0.051	1.24	0.02	3.42	20.17
Non- magnetics 2	1.1	34.8	37.14	0.5	1.95	1.95	0.92	0.056	BDL	0.019	0.117	0.056	1.58	0.33	0.4	8.7
							Milled to	ο Ρ ₈₀ 30 μ	m							
Magnetics	92.7	70.52	1.77	BDL	0.1	0.1	0.05	0.008	BDL	BDL	0.009	0.005	BDL	0.004	96.4	36.5
Non- magnetics 1	6.2	28.39	35.1	0.36	2.28	2.7	0.94	0.033	BDL	0.018	0.111	0.062	1.54	0.027	2.22	59.71
Non- magnetics 2	1.2	44.19	28.71	0.38	1.92	2.28	0.84	0.049	BDL	0.017	0.101	0.057	1.39	0.035	1.0	38.3
							Milled to	ο P ₈₀ 15 μ	m							
Magnetics	91.7	71.02	1.07	BDL	0.06	0.08	0.05	0.009	BDL	BDL	0.007	0.005	BDL	0.004	96.0	21.6
Non- magnetics 1	7.2	29.02	44.28	0.38	2.41	2.86	1.01	0.035	BDL	0.014	0.098	0.07	1.59	0.033	3.1	68.5
Non- magnetics 2	1.2	54.21	17.21	0.29	1.03	1.37	0.44	0.035	BDL	0.014	0.064	0.044	0.89	0.021	0.9	9.9
BDL: Below D	etection L	imit (Al ₂ O	3: 0.04%;	V ₂ O ₅ : 0.0	09%; Na	a ₂ O: 0.00	6%; C:0.	14%; NS:	Not avai	lable due	to insuffici	ent sampi	le			

Table 28. Results on magnetic separation in a two-stage LIMS for Sample C.

Products	Mass Pull						Ass	say Value	(%)							bution ue (%)
Products	(%)	Fe _(t)	SiO ₂	Al ₂ O ₃	CaO	MgO	MnO	TiO ₂	V ₂ O ₅	Na ₂ O	K₂O	Р	С	s	Fe _(t)	SiO ₂
							As-recei	ved samp	le							
Magnetics	94.8	69.09	2.65	BDL	0.15	0.24	0.07	0.007	BDL	BDL	0.008	0.008	0.15	0.007	97.2	48.7
Non- magnetics 1	4.17	24.45	50.62	0.38	2.47	4.25	0.83	0.031	BDL	0.011	0.069	0.039	1.93	0.031	3.42	20.17
Non- magnetics 2	1.1	39.77	31.25	0.37	2.1	3.08	0.87	0.047	BDL	0.013	0.063	0.039	2.08	0.039	0.9	8.5
							Milled to	Ρ ₈₀ 30 μι	m							
Magnetics	92.3	70.76	1.55	BDL	0.1	0.13	0.04	0.008	BDL	0.007	0.008	0.006	BDL	0.003	97.0	27.6
Non- magnetics 1	6.5	24.19	47.28	0.33	2.75	4.05	0.91	0.026	BDL	0.017	0.077	0.053	2.29	0.022	2.3	67.3
Non- magnetics 2	1.2	39.31	29.86	0.4	2.1	3.31	0.77	0.056	BDL	0.017	0.08	0.056	1.96	0.042	0.7	5.1
							Milled to	Ρ ₈₀ 15 μι	m							
Magnetics	92.4	70.68	1.23	BDL	0.04	0.09	0.03	0.006	BDL	BDL	0.006	0.005	BDL	0.006	96.9	21.6
Non- magnetics 1	7.1	25.85	46.75	0.34	2.86	4.16	1.01	0.032	BDL	0.031	0.074	0.06	2.29	0.045	2.7	73.5
Non- magnetics 2	0.5	46.69	24.59	0.31	1.53	2.52	0.59	0.046	BDL	0.01	0.054	0.042	1.56	0.028	0.3	4.9
BDL: Below D	etection L	.imit (Al₂O	3: <mark>0.04%;</mark>	V ₂ O ₅ : 0.0	09%; Na	20: 0.00	6%; C: 0.	14%; NS:	Not ava	ilable due	to insuffic	ient samp	le			

Froth Flotation Results

Froth flotation experiments were carried out by varying the particle size of P_{80} (45, 30, and 15 µm) as well as collector dosage (125, 93.75 and 62.5 g/t) and keeping all other variables constant. This study employed a Response Surface Methodology (RSM) using a Central Composite Design (CCD) to systematically investigate the effects of two key flotation variables: mesh of grind (particle size) and collector dosage to float silicate-bearing gangue minerals as a float fraction. This methodology involves a structured set of experiments, including factorial points (testing high/low combinations), axial points (testing extreme values), and central points (testing midrange values) to map out the process response, as shown in **Figure 24**. The primary advantage of this design is its efficiency in gathering detailed information from a limited number of tests, which allows for the development of a predictive mathematical model. This model can identify not only the individual and interactive effects of the variables but also, crucially, can determine the optimal operating conditions for maximizing flotation performance by accounting for non-linear (curved) responses. For the present investigation, the design of experiments, along with test conditions, are tabulated in **Table 29**.

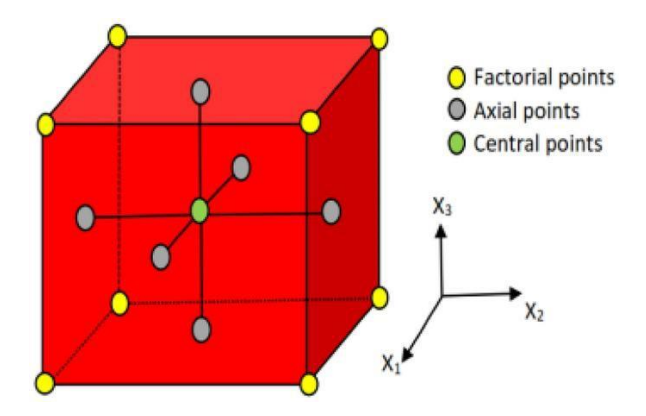


Figure 24. RSM-CCD experimental design.

Table 29. Design of experiment	considered for the flotation	tasts along with tast conditions
Table 23. Design of experiment	. Considered for the notation	lesis, along with lest conditions.

Test No	Pattern	Mesh of grind, micron	Collector dosage (g/t)
1		15	62.5
2	-+	15	125
3	+-	45	62.5
4	++	45	125
5	a0	15	93.75
6	A0	45	93.75
7	0a	30	62.5
8	0A	30	125
9	0	30	93.75
10	0	30	93.75

Experimental Results - Sample A

Table 30 presents the results of a designed flotation experiment (RSM) for Sample A, systematically evaluating the impact of grind size and collector dosage on separation performance. The data reveals a clear trade-off between the quality (grade) and quantity (recovery) of the concentrate. Finer grinding (e.g., to 15 µm) consistently produces a higher-grade concentrate with an iron content >71% and silica impurity below 1.2%. However, this improvement in grade generally comes at the cost of lower iron recovery, a trend that is also strongly influenced by the collector dosage. The wide range of outcomes, from a high iron recovery of 94.7% with a coarse grind to a high iron grade of 71.25% at the expense of recovery, demonstrates the complex interactions that this experimental design is intended to map and optimize. Further, a grade-recovery correlation was plotted and shown in **Figure 25**.

In addition to managing the primary iron-silica separation, the flotation results for Sample A also demonstrate the effectiveness of the process in rejecting various minor gangue elements. Similar to silica, the concentrations of other major gangue components like calcium oxide (CaO), magnesium oxide (MgO), and manganese oxide (MnO) in the final concentrate are significantly reduced with finer grinding; for example, grinding to 15 μ m lowers CaO and MgO content to 0.12% each, compared to over 0.20% with a coarser grind at 45 μ m. The flotation process is exceptionally effective at removing minerals containing alumina, vanadium, and sodium, as their concentrations are consistently below detection limits. Furthermore, deleterious elements such as phosphorus (P) and sulfur (S) are also kept at extremely low levels (typically less than 0.005%).

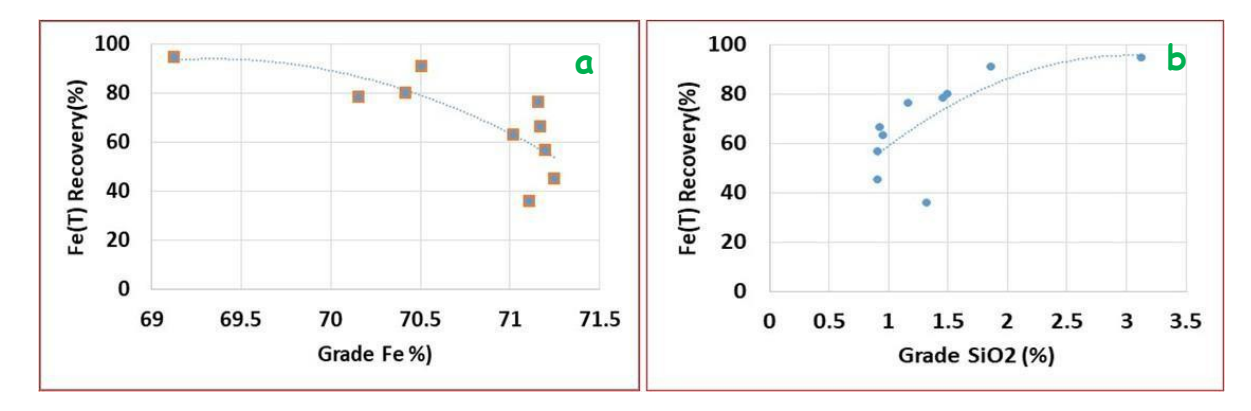


Figure 25. Grade-recovery correlation for iron and silica content in the flotation concentrate/underflow for Sample A.

For a better understanding of the kinetics of the flotation of silica, froth recovery curves for each stage are plotted for each experiment (for example, Test 1, **Figure 26**). The flotation kinetics data reveals a significant difference in the flotation rate and cumulative recovery of silicates across the five stages. The initial stages (1 and 2) show very slow kinetics and low recovery, while the later stages (4 and 5) exhibit much faster flotation rates, particularly within the first 60 seconds, and achieve a significantly higher cumulative removal of the floated gangue material with high entrainment of concentrates (magnetite). Similar plots for each test are shown in Appendix D.

These kinetics data indicate that the flotation rate and the total amount of floated material consistently increase from Stage 1 to Stage 5, with the latter stages always showing the fastest kinetics, but this may be due to more entrainment of magnetite into froth. The primary difference between the plots is the overall flotation performance, where some test conditions result in a low cumulative float of only a few percent, while others achieve a much higher removal of gangue, with the cumulative float reaching up to 18%. This variation directly reflects the different grind

sizes and collector dosages used in the experimental design, demonstrating their strong influence on the efficiency of silicate flotation.

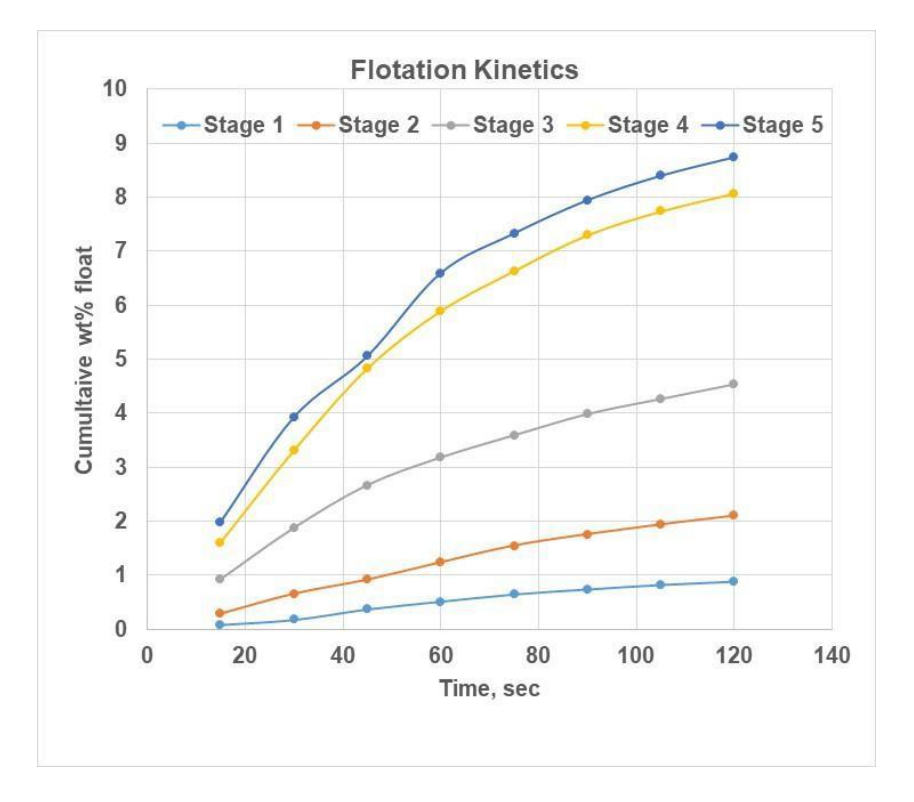


Figure 26. Kinetics curve for froth recovery of each stage of flotation (NRRI Test 1) for Sample A.

Table 30. Results of the flotation concentrate/underflow for Sample A.

NRRI	Test		Mesh of	Collector	Mass	Assay Value (%)									Distrib Value					
Test No.	No	Pattern	grind, micron	dosage (g/t)	Pull (%)	Fe _(t)	SiO ₂	Al ₂ O ₃	CaO	MgO	MnO	TiO ₂	V ₂ O ₅	Na ₂ O	K₂O	Р	C	s	Fe _(t)	SiO ₂
9	1		15	62.5	72.68	71.16	1.17	BDL	0.12	0.12	0.07	0.007	BDL	BDL	0.008	0.005	BDL	0.003	76.26	18.94
10	2	-+	15	125	43.04	71.25	0.91	BDL	0.09	0.09	0.06	0.006	BDL	BDL	0.006	0.004	BDL	0.003	45.22	8.72
2	3	+-	45	62.5	92.86	69.13	3.13	BDL	0.21	0.22	0.11	0.009	BDL	BDL	0.011	0.008	0.16	0.006	94.65	64.73
1	4	++	45	125	75.67	70.26	1.46	BDL	0.15	0.15	0.08	0.007	BDL	BDL	0.009	0.007	0.13	0.005	78.28	24.61
8	5	a0	15	93.75	53.97	71.2	0.91	BDL	0.1	0.09	0.06	0.007	BDL	BDL	0.008	0.004	BDL	0.003	56.66	10.94
3	6	A0	45	93.75	77.12	70.42	1.50	BDL	0.16	0.17	0.09	0.008	BDL	BDL	0.01	0.006	0.18	0.005	80.07	25.76
5	7	0a	30	62.5	87.68	70.51	1.86	BDL	0.16	0.17	0.09	0.007	BDL	BDL	0.011	0.007	NS	NS	91.15	36.32
4	8	0A	30	125	34.28	71.11	1.32	BDL	0.08	0.09	0.05	0.007	BDL	BDL	0.006	0.004	BDL	0.004	35.94	10.08
6	9	0	30	93.75	63.31	71.17	0.93	BDL	0.11	0.11	0.06	0.007	BDL	BDL	0.007	0.005	BDL	0.003	66.43	13.11
7	10	0	30	93.75	60.27	71.02	0.96	BDL	0.1	0.11	0.06	0.007	BDL	BDL	0.007	0.005	BDL	0.003	63.12	12.89
		0 Detection I												BDL	0.007	0.005	BDL	0.003		63.12

BDL: Below Detection Limit (Al₂O₃: 0.04%; V₂O₅: 0.009%; Na₂O: 0.006%; C: 0.14%; P: 0.003%; S: 0.003%

Statistical Analysis – Sample A

Table 31 and **Table 32** present statistical models from the Response Surface Methodology (RSM) analysis, quantifying how the mesh of grind (A) and collector dosage (B) influence the key performance indicators of the flotation process for Sample A. The significance of each factor is determined by its "Prob>|t|" value (p-value), where values less than 0.05 indicate a statistically significant effect. Prior to analysis, the diagnostic plot (correlation between actual and prediction) for all the studied responses are shown in **Figure VIII** (Appendix C). These figures are used to validate the statistical models that were developed from experimental data. Each plot compares the predicted values from the model (on the x-axis) against the actual measured values from the experiments (on the y-axis). A strong, reliable model will have its data points falling closely along the red diagonal line, a relationship that is quantified by a high R-squared (Rsq) value.

The models for Silica Rejection (Rsq = 0.97), Silica Grade (Rsq = 0.95), Mass Pull (Rsq = 0.90), Iron Grade (Rsq = 0.89), and Iron Recovery (Rsq = 0.89) are all shown to be robust and highly predictive. Their high R-squared values and significant p-values (<0.05) indicate that the mathematical models accurately capture the relationships between the process variables (grind size, collector dosage) and these specific outcomes. The tight clustering of the data points around the diagonal line for these four responses confirms their reliability.

This analysis clearly illustrates the fundamental trade-off between concentrate grade and iron recovery and shows that the factors that significantly increase iron recovery, namely a coarser grind (A) and a lower collector dosage (B), are the same factors that simultaneously *decrease* the final iron grade. This classic metallurgical conflict is evident in the significant, opposing, estimates for variables A and B on the Fe Grade and Fe recovery models. The mass pull to the concentrate is also significantly affected, mirroring the recovery trend where coarser grinds increase the mass pull, and higher dosages decrease it.

Similarly, the analysis of silica grade in the underflow and silica rejection to the froth reveals a more complex system. While a finer grind (A) and a higher collector dosage (B) are both statistically significant factors that improve silica removal, their effects are not purely linear. Crucially, the models for both the silica grade in the concentrate and silica rejection to the tailings show significant interaction effects (A*B) and a quadratic effect for dosage (B²). This means the effectiveness of the collector dosage depends on the grind size, and its impact is curved, indicating that an optimal dosage exists to maximize silica rejection without overdosing the system.

Table 31. Parameter estimate as well as other model parameters along with statistical data for mass pull, grade ($Fe_{(T)}$, SiO_2) of flotation concentrate/underflow for Sample A.

	Mass	Pull (W	(t.%)	F	e _(T) (%)		Si	O ₂ (%)		
Term	Estimate	t Ratio	Prob> t	Estimate	t Ratio	Prob> t	Estimate	t Ratio	Prob> t	
Intercept	59.9	11.04	0.0004*	71.13	507.13	<.0001*	0.99	7.00	0.0022*	
A: Mesh of grind, micron	12.66	3.41	0.0270*	-0.65	-6.78	0.0025*	0.52	5.31	0.0060*	
B: Collector dosage (g/t)	-16.71	-4.50	0.0108*	0.28	2.99	0.0403*	-0.42	-4.23	0.0133*	
(A*B): Mesh of grind, micron*Collector dosage (g/t)	3.12	0.68	0.5312	0.235	2.00	0.1158	-0.35	-2.96	0.0416*	
(A ²): Mesh of grind, micron*Mesh of grind, micron	7.37	1.24	0.2833	-0.34	-2.23	0.0899	0.16	1.00	0.3747	
(B ²): Collector dosage (g/t)*Collector dosage (g/t)	2.80	0.47	0.6620	-0.34	-2.23	0.0899	0.54	3.47	0.0257*	
Model type	2 nd ord	ler quad	Iratic	2 nd ord	der quad	ratic	2nd ord	er quadr	atic	
Standard Deviation		9.093			0.235		0.238			
Correlation Coefficient	0.90				0.95		0.95			
Significant Parameters		A, B			A, B		A, B, A*B, B ²			

Table 32. Parameter estimate as well as other model parameters along with statistical data for recovery $Fe_{(T)}$, rejection of SiO_2 of flotation concentrate/underflow for Sample A.

Term	Recovery	Fe _(T) (%)		Rejec	tion SiO₂(%)		
Term	Estimate	t Ratio	Prob> t	Estimate	t Ratio	Prob> t	
Intercept	62.93	11.07	0.0004*	87.2	31.43	<.0001*	
A: Mesh of grind, micron	12.47	3.21	0.0325*	-12.75	-6.73	0.0025*	
B: Collector dosage (g/t)	-17.11	-4.40	0.0117*	12.78	6.73	0.0025*	
(A*B): Mesh of grind, micron*Collector dosage (g/t)	3.67	0.77	0.4837	7.48	3.22	0.0323*	
(A ²): Mesh of grind, micron*Mesh of grind, micron	7.29	1.17	0.3070	-5.75	-1.89	0.1315	
(B ²): Collector dosage (g/t)*Collector dosage (g/t)	2.47	0.40	0.7124	-10.6	-3.49	0.0252*	
Model type	2 nd order q	uadratic		2 nd ord	der quadratio	;	
Standard Deviation	9.513			4.64			
Correlation Coefficient	0.89	9		0.97			
Significant Parameters	A, I	3		A, B, A*B, B ²			

Contour plots (**Figure 27**) can be used to visualize the results of the Response Surface Methodology, illustrating how the mesh of grind (x-axis) and collector dosage (y-axis) interact to affect the key flotation responses. The plots clearly demonstrate the fundamental trade-off between concentrate grade and iron recovery. The highest iron grade (>71.25%) and the lowest silica impurity (<1.00%) are both achieved in the same region: at a fine grind (around 15 μ m) combined with a high collector dosage (>110 g/t). Conversely, the highest iron recovery (>90%) is found in the opposite corner of the experimental space, requiring a coarse grind (>40 μ m) and a low collector dosage. These plots are essential for process optimization, as they allow for the identification of operating conditions that provide the best balance between achieving a high-purity product and maximizing the recovery of the valuable mineral.

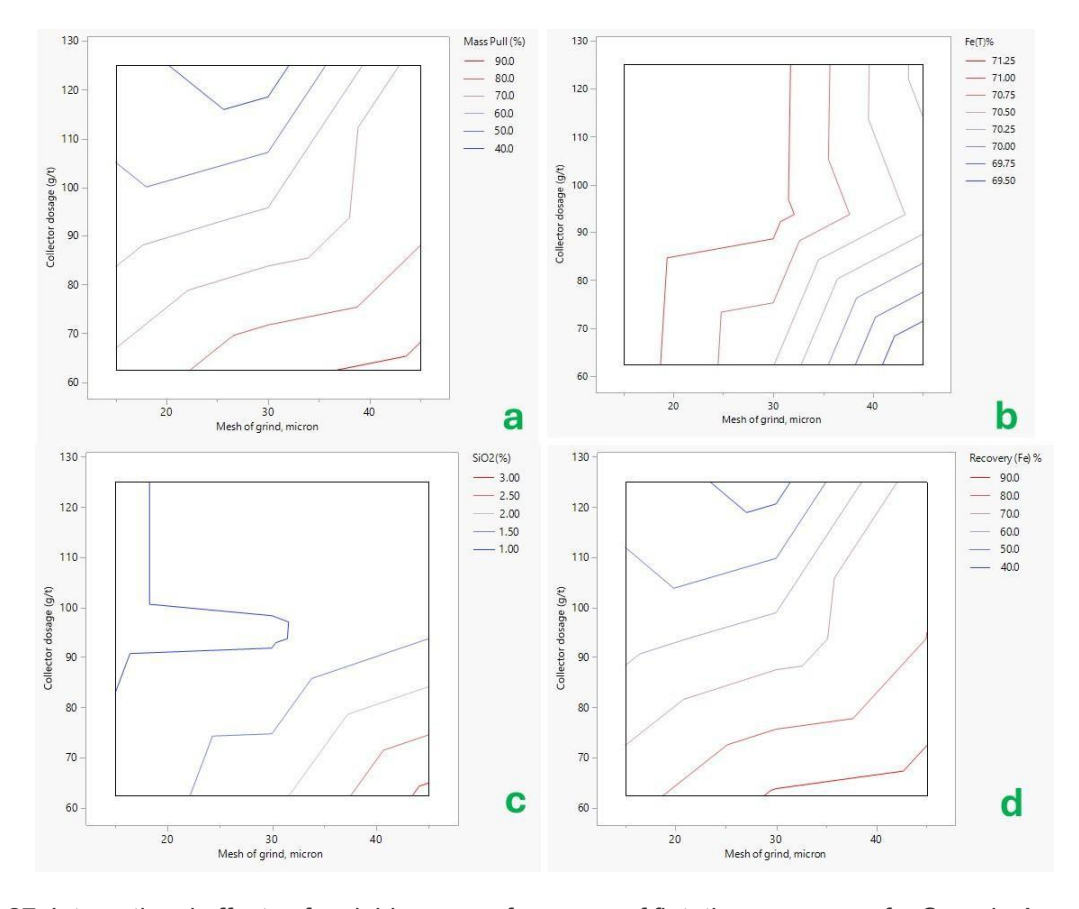


Figure 27. Interactional effects of variables on performance of flotation responses for Sample A.

Experimental Results - Sample C

A series of flotation tests was conducted with Sample C using the design of experiments described above for Sample A. The results (**Table 33**) reveal a distinct trade-off between the concentrate grade and the recovery of iron, driven by the variations in grind size and collector dosage. The highest iron grade of 71.07% Fe (Test 2) was achieved with a fine grind (15 μ m) and high collector dosage, but this resulted in a lower iron recovery of 74.8%. Conversely, the highest iron recovery of 95.56% (Test 3) was obtained with a coarse grind (45 μ m), but this came at the expense of a lower grade (68.01% Fe) and a high silica impurity of 4.21%.

The experiment successfully identified conditions that provide an excellent balance between these competing objectives. Notably, Test 1, which used a fine grind (15 μ m) with a low collector dosage, achieved a strong combination of a high iron grade (70.02%), low silica (1.64%), and a high iron recovery of 88.38%. The behavior of other minor gangue elements, such as CaO, MgO, and MnO, followed the same trend as silica; the conditions that promoted effective silica flotation also led to a more efficient rejection of these other impurities, resulting in a cleaner final concentrate across the board. Further, a grade-recovery correlation was plotted and is shown in **Figure 28**.

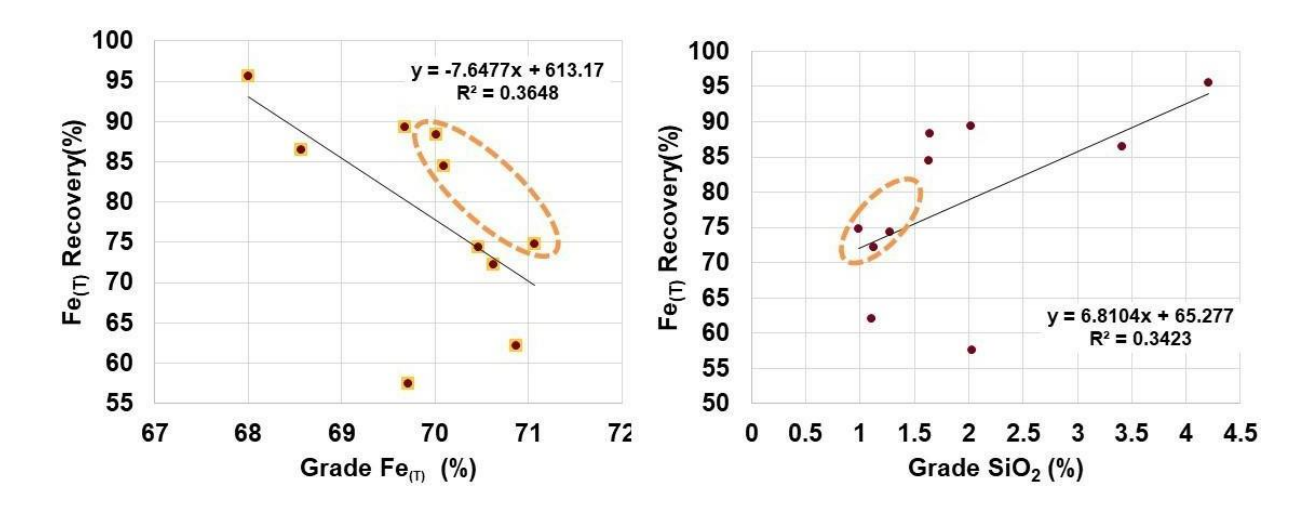


Figure 28. Grade-recovery correlation for iron and silica content in the flotation concentrate/underflow for Sample C.

For a better understanding of the kinetics of silica flotation, froth recovery curves for each stage are plotted for each experiment (for example, Test 1, **Figure 29**). The flotation kinetics show the cumulative weight percent of floated gangue (silicates) over a period of 120 seconds for five sequential flotation stages. The data clearly shows a progressive increase in both the rate and the total amount of floated material from Stage 1 through Stage 5. For example, after 120 seconds, Stage 1 removes less than 3% of the material, while the cumulative removal by Stage 5 exceeds 13%. This demonstrates that the later stages of the flotation process are the most aggressive due to entrainment of magnetite into the froth fraction in the final stages. The high overall cumulative float suggests that the conditions of Test 1 were very effective at promoting silica flotation.

The comparative analysis of flotation kinetics for tests 2 through 10 demonstrates how varying grind size and collector dosage create a wide spectrum of gangue removal efficiencies. Tests with aggressive kinetics, such as #4 and #8, show the fastest and most extensive silica flotation, resulting in a high-grade concentrate but often at the cost of poor iron recovery due to low selectivity. Conversely, tests with weak kinetics, like #2 and #5, result in poor gangue removal, yielding a lower-grade product but with higher iron recovery. A balanced kinetic profile, as seen in Test #7, represents an optimal condition in which gangue is effectively removed in a controlled manner, achieving a favorable balance between a high-grade final product and high recovery of the valuable magnetite.

A more complete froth flotation kinetic dataset and response models for Sample A can be found in Appendix D.

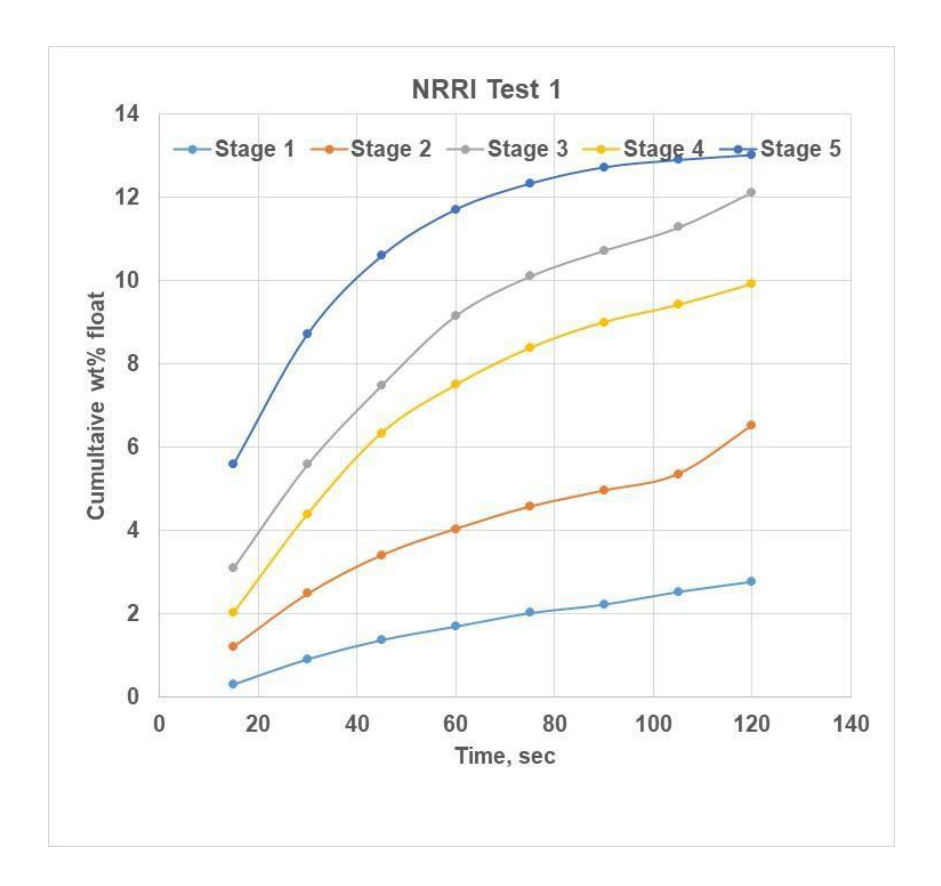


Figure 29. Kinetics curve for froth recovery of each stage of flotation (NRRI Test 1) for Sample C.

Table 33. Results of the flotation concentrate/underflow for Sample C.

NRRI	Test		Mesh of	Collector	Mass							Assay Va	lue (%)							bution ie (%)
Test No.	No	Pattern	grind, micron	dosage (g/t)	Pull (%)	Fe _(t)	SiO ₂	Al ₂ O ₃	CaO	MgO	MnO	TiO ₂	V ₂ O ₅	Na₂O	K20	Р	O	ø	Fe _(t)	SiO ₂
9	1		15	62.5	85.05	70.02	1.64	BDL	0.18	0.22	0.08	0.007	BDL	0.021	0.008	0.007	0.19	0.004	88.38	26.62
10	2	-+	15	125	70.92	71.07	0.99	BDL	0.09	0.09	0.06	0.006	BDL	BDL	0.01	0.006	BDL	0.003	74.81	13.40
2	3	+-	45	62.5	94.67	68.01	4.21	BDL	0.26	0.37	0.11	0.009	BDL	BDL	0.012	0.009	0.25	0.007	95.56	76.07
1	4	++	45	125	55.6	69.71	2.03	BDL	0.2	0.25	0.08	BDL	BDL	BDL	0.006	0.007	0.18	0.006	57.52	21.54
8	5	a0	15	93.75	68.89	70.63	1.13	BDL	0.14	0.15	0.06	0.006	BDL	0.027	0.007	0.006	0.14	0.004	72.21	14.86
3	6	A0	45	93.75	84.93	68.57	3.41	BDL	0.16	0.17	0.09	0.008	BDL	BDL	0.01	0.006	0.18	0.005	86.43	55.27
5	7	0a	30	62.5	86.36	69.68	2.02	BDL	0.2	0.25	0.12	0.008	BDL	BDL	0.009	0.008	0.22	0.005	89.31	33.29
4	8	0A	30	125	59.05	70.87	1.11	BDL	0.14	0.14	0.06	0.006	BDL	BDL	0.007	0.006	BDL	0.005	62.10	12.51
6	9	0	30	93.75	71.09	70.46	1.27	BDL	0.16	0.18	0.07	0.007	BDL	BDL	0.007	0.007	0.16	0.004	74.34	17.23
7	10	0	30	93.75	81.23	70.09	1.63	BDL	0.18	0.22	0.08	0.007	BDL	0.024	0.009	0.007	0.2	0.005	84.50	25.27
7		0	30	93.75	81.23	70.09	1.63	BDL	0.18				BDL		0.009	0.007	0.2	0.005	84	.50

BDL: Below Detection Limit (Al₂O₃: 0.04%; V₂O₅: 0.009%; Na₂O: 0.006%; C: 0.14%; P: 0.003%; S: 0.003%

Statistical Analysis – Sample C

Table 34 presents the statistical models from the Response Surface Methodology (RSM) analysis, quantifying how the mesh of grind (A) and collector dosage (B) influence the key performance indicators of the flotation process for Sample A. The significance of each factor is determined by its "Prob>|t|" value (p-value), where values less than 0.05 indicate a statistically significant effect. Prior to analysis, the diagnostic plot (correlation between actual and prediction) for all the studied responses are shown in **Figure XV** (Appendix D). These figures are used to validate the statistical models that were developed from experimental data. Each plot compares the predicted values from the model (on the x-axis) against the actual measured values from the experiments (on the y-axis). A strong, reliable model will have its data points falling closely along the red diagonal line, a relationship that is quantified by a high R-squared (Rsq) value.

Table 34 summarizes the robust statistical models for the flotation of Sample C, which effectively predict performance based on the mesh of grind (A) and collector dosage (B). All developed models show good to excellent correlation coefficients (R² from 0.87 to 0.98), indicating high reliability for prediction.

The models reveal that iron grade is significantly improved by both a finer grind (A) and a higher collector dosage (B), and it also shows a significant non-linear (quadratic) response to the grind size. In contrast, iron recovery is only significantly impacted by the collector dosage (B), with higher dosages leading to lower recovery; grind size was not a statistically significant factor for recovery in this model. The removal of silica (SiO₂) is governed by the most complex relationships, being significantly influenced by the linear effects of both grind and dosage, a significant interaction between the two (A*B), and a significant quadratic effect of the grind size (A²). This indicates that optimizing silica rejection requires careful consideration of these complex, non-linear effects, while managing iron recovery primarily involves controlling the collector dosage.

Contour plots for Sample C were developed (**Figure 30**) to better visualize the interaction effect of variables. The plots for Iron Grade (Fe%) and Silica Grade ($SiO_2\%$) show that the highest quality concentrate, with the highest iron and lowest silica, is produced in the top-left corner of the design space. This region corresponds to using a fine grind combined with a high collector dosage, a condition that maximizes the liberation and subsequent removal of silica impurities. Conversely, the plots for Iron Recovery (Fe%) and Mass Pull show that the highest recovery is achieved in the opposite, bottom-right corner. This region corresponds to a coarse grind and a low collector dosage, which is less selective and therefore minimizes the loss of valuable iron minerals to the tailing/froth. These plots serve as a powerful visual guide for selecting the optimal operating parameters that best balance the competing goals of producing a high-purity product and maximizing mineral recovery.

A more complete froth flotation kinetic dataset and response models for Sample C can be found in Appendix D.

Table 34. Results of parameter estimate, as well as other model parameters, along with statistics data for mass pull, grade ($Fe_{(T)}$, SiO_2), recovery ($Fe_{(T)}$ %) of flotation concentrate/underflow for Sample C.

	Mass	Pull (W	t.%)	i	Fe _(T) (%)		;	SiO ₂ (%)		Re	covery Fe (T)	[%)
Term	Estimate	t Ratio	Prob> t	Estimate	t Ratio	Prob> t	Estimate	t Ratio	Prob> t	Estimate	t Ratio	Prob> t
Intercept	75.27	18.99	<.0001*	70.25	645.26	<.0001*	1.5	10.21	0.0005*	78.43	19.40	<.0001*
A: Mesh of grind, micron	1.73	0.64	0.5592	-0.91	-12.17	0.0003*	0.98	9.80	0.0006*	0.69	0.25	0.8163
B: Collector dosage (g/t)	-13.42	-4.95	0.0077*	0.66	8.83	0.0009*	-0.63	-6.22	0.0034*	-13.14	-4.76	0.0089*
(A*B): Mesh of grind, micron*Collector dosage (g/t)	-6.24	-1.88	0.1333	0.16	1.78	0.1490	-0.38	-3.12	0.0357*	-6.12	-1.81	0.1447
(A ²): Mesh of grind, micron*Mesh of grind, micron	2.53	0.58	0.5923	-0.62	-5.17	0.0067*	0.73	4.51	0.0108*	1.88	0.42	0.6932
(B ²): Collector dosage (g/t)*Collector dosage (g/t)	-1.68	-0.39	0.7185	0.06	0.49	0.6491	0.02	0.12	0.9103	-1.74	-0.39	0.7149
Model type	2 nd or	der quad	ratic	2 nd or	der quadı	atic	2nd order quadratic			2 nd order quadratic		
Standard Deviation		6.64			0.182			0.25			6.76	
Correlation Coefficient	ion Coefficient 0.88		0.984				0.98		0.87			
Significant Parameters	В		A, B, A ²			A, B, A*B, A ²			A, B			

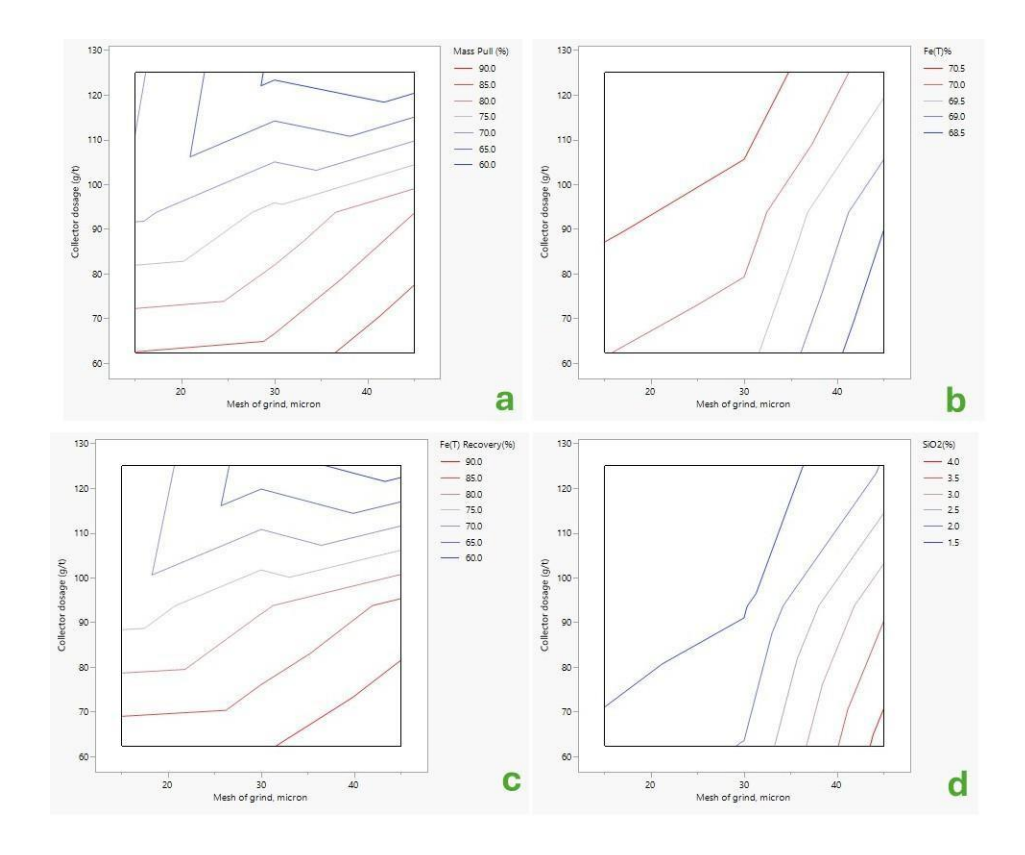


Figure 30. Interactional effects of variables on performance of flotation responses for Sample C.

Combination of Magnetic Separation and Flotation Results

Based on the above results, it was found that magnetic separation can be used to preconcentrate, but it may not achieve the high-purity iron oxide target as a stand-alone procedure. Thus, a combination of both magnetic separation and flotation was developed (**Figure 31**). The flotation conditions are similar to the earlier work, but deviated in the dosage, which was planned to facilitate the addition of two more stages, resulting in seven stages rather than five. A set of design of experiments was planned as per **Table 35** and executed for both Sample A and C. The results of the final concentrate for each are given in **Table 36** and **Table 37**, respectively.

Combined magnetic separation and flotation tests on Sample A (**Table 36**) demonstrate that this process is highly effective at producing an exceptionally high-purity concentrate under all tested conditions. Across different grind sizes and collector dosages, the final iron (Fe) grade was consistently very high, ranging from 70.6% to 71.5%, while the silica (SiO_2) impurity was kept very low at 0.84% to 1.2%. The primary difference between the test conditions was their impact on iron recovery, which ranged from 12.39% to a very high 69.94%. The optimal result was achieved in Test 5 (15 μ m grind, 125 g/t collector), which successfully combined a high iron grade of 71.41% with excellent silica rejection (97.8%), but the recovery was very low at 12.39%.

The results from the combined magnetic separation and flotation tests on Sample C show that the process consistently produced a very high purity concentrate but resulted in a severe trade-off between silica rejection and iron recovery, particularly at high collector dosages. Across all conditions, the final iron (Fe) grade was excellent, ranging from 70.1% to 71.5%, with the silica (SiO_2) impurity as low as 0.86%. However, the choice of operating parameters had a dramatic effect on efficiency. Conditions designed for maximum cleaning, such as in Test 5 (15 µm grind, 125 g/t collector), achieved a near-perfect silica rejection of 97.7% but at the cost of an extremely

poor iron recovery of only 14.9%. The most balanced performance was seen in tests with the lower collector dosage, such as Test 6, which provided a good compromise with 73.7% iron recovery and 86.2% silica rejection.

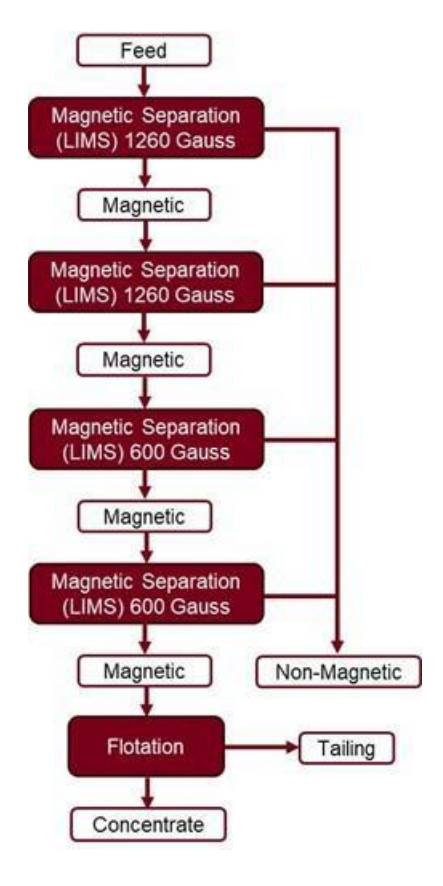


Figure 31. Experimental plan and process flow for the test work with a combination of both magnetic separation and flotation.

Table 35. Design of experiment (DOE) adopted for the combination of magnetic separation and flotation.

Test No	Mesh of grind (µm)	Collector dosage (g/t)
1	30	125
2	30	62.5
3	45	125
4	45	62.5
5	15	125
6	15	62.5

Table 36. Results of the combined studies using magnetic separation and flotation for Sample A.

Test	Mesh of	Collector	Mass						As	ssay Value	e (%)						Recovery	Rejection
No	grind, µm	dosage (g/t)	Pull (%)	Fe _(t)	SiO ₂	Al ₂ O ₃	CaO	MgO	MnO	TiO ₂	V ₂ O ₅	Na₂O	K₂O	Р	С	s	(%) Fe _(t)	(%) SiO ₂
1	30	125	7.92	71.46	0.88	BDL	0.08	0.06	0.04	0.006	BDL	0.01	0.011	0.005	BDL	0.003	8.35	98.45
2	30	62.5	64.19	71.33	0.93	BDL	0.08	0.06	0.04	0.007	BDL	0.009	0.011	0.004	BDL	BDL	67.51	86.70
3	45	125	26.05	70.57	1.05	BDL	0.16	0.12	0.06	0.006	BDL	BDL	0.008	0.005	BDL	BDL	27.11	93.91
4	45	62.5	66.98	70.82	1.2	BDL	0.16	0.13	0.07	0.007	BDL	BDL	0.009	0.006	BDL	BDL	69.94	82.10
5	15	125	11.77	71.41	0.84	BDL	0.06	0.05	0.03	0.006	BDL	BDL	0.007	BDL	BDL	BDL	12.39	97.80
6	15	62.5	70.24	71.35	0.98	BDL	0.09	0.07	0.04	0.007	BDL	BDL	0.007	BDL	BDL	BDL	73.9	84.67
DDI:	BDL: Below Detection Limit (AlaCa: 0.04%: VaCa: 0.000%: NaaCa: 0.006%: C: 0.14%: P: 0.003%: S: 0.003%																	

BDL: Below Detection Limit (Al₂O₃: 0.04%; V₂O₅: 0.009%; Na₂O: 0.006%; C: 0.14%; P: 0.003%; S: 0.003%

Table 37. Results of the combined studies using magnetic separation and flotation for Sample C.

T4	Mesh	Collector	Mass							Assay Valu	e (%)						B	Deiretien
Test No	of grind, µm	dosage (g/t)	Pull (%)	Fe _(t)	SiO ₂	Al ₂ O ₃	CaO	MgO	MnO	TiO ₂	V ₂ O ₅	Na₂O	K₂O	Р	С	s	Recovery (%) Fe _(t)	Rejection (%) SiO ₂
1	30	125	20.79	71.38	0.86	BDL	0.05	0.05	0.02	BDL	BDL	0.01	0.013	0.004	BDL	0.003	22.03	96.54
2	30	62.5	63.59	71.54	0.98	BDL	0.07	0.07	0.02	BDL	BDL	BDL	0.005	0.004	BDL	0.005	67.53	87.92
3	45	125	42.35	70.67	1.64	BDL	0.19	0.19	0.06	0.006	BDL	0.015	0.009	0.006	0.14	0.005	44.42	86.54
4	45	62.5	76.06	70.14	2.16	BDL	0.2	0.21	0.07	0.006	BDL	0.011	0.008	0.007	0.17	0.005	79.19	68.16
5	15	125	14.04	71.37	0.86	BDL	0.06	0.05	0.02	BDL	BDL	BDL	0.005	BDL	BDL	0.004	14.87	97.66
6	15	62.5	69.7	71.24	1.02	BDL	0.1	0.07	0.03	BDL	BDL	BDL	0.006	BDL	BDL	0.003	73.70	86.22
																		<u>i</u>

BDL: Below Detection Limit (Al₂O₃: 0.04%; V₂O₅: 0.009%; Na₂O: 0.006%; C: 0.14%; P: 0.003%; S: 0.003%

Beneficiation Results - Comparison Analysis

A compilation of the results comparing the concentrate quality for each of the beneficiation app8roaches is shown in **Table 38** and **Table 39**.

Table 38 compares different processing routes, such as flotation, single-stage LIMS, two-stage LIMS, and a combined circuit at three different grind sizes for Sample A. The results highlight the most effective route to balance concentrate grade with iron recovery for this specific sample. Across all grind sizes, magnetic separation (LIMS) consistently provides the highest iron recovery, typically exceeding 96%. The two-stage LIMS process is particularly effective; as the ore is milled finer, it significantly improves the concentrate grade without sacrificing recovery. At the optimal 15 µm grind, the two-stage LIMS circuit delivers high iron grade (71.02%) with a high iron recovery (96.0%), making it the most efficient and robust flowsheet for this sample. Further, the mineralogy of the magnetic separation products was carried out using XRD and found that magnetite is the major mineral in the magnetic fraction with minor quantities of quartz. Similarly, the non-magnetic fraction is segregated with quartz as the major phase along with other minor mineral phases. The XRD patterns for both the products are shown in Figure XVI and Figure XVII in Appendix E. In contrast, while flotation alone can also produce a high-grade concentrate (71.2% Fe_(T)), it does so at a severe cost to product yield, with iron recovery dropping to a poor 57% at the same fine grind. The combined LIMS-Two Stage with flotation circuit consistently produces the highest possible grade (over 71.4% Fe_(T) with only 0.84% SiO₂). The mineralogy of the concentrate (underflow) along with tailing (froth) was analyzed in XRD, and the patterns with identified minerals are shown in Figure XVIII and Figure XIX in Appendix E. This data confirms the presence of only magnetite peaks and tailing fraction with quartz as a major phase along with hematite and magnetite which lost due to poor selectivity. However, this ultra-high purity is achieved with a significant loss of iron, with recoveries reducing to ~9–12% weight recovery. This circuit, therefore, serves only to demonstrate the maximum achievable purity and may not be a viable production route due to low product yield.

Table 39 provides a detailed comparison of different mineral processing routes such as flotation, single-stage LIMS, two-stage LIMS, and a combined LIMS-flotation circuit at three different grind sizes for Sample C. The results clearly show how the choice of processing route and grind size impacts the final balance between concentrate grade and iron recovery. Across all grind sizes, magnetic separation (LIMS) consistently provides the highest iron recovery, typically exceeding 97%. A two-stage LIMS process proves to be the most effective overall flowsheet, consistently improving concentrate grade by rejecting more silica than a single-stage process, with only a minimal loss in recovery. In contrast, the performance of flotation alone is highly dependent on grind size; it is inferior to LIMS at coarse grinds but becomes very effective at producing a highgrade concentrate (~71.1% Fe_(T), 0.99% SiO₂) after fine grinding to 15 µm, though its iron recovery (~75%) remains significantly lower than the LIMS circuits. Further, mineralogical analysis of the magnetic separation products using XRD found that magnetite is the major mineral in the magnetic fraction with minor quantities of quartz. Similarly, the non-magnetic fraction is segregated with quartz as the major phase along with other minor mineral phases. The XRD patterns for both the products are shown in Figure XX and Figure XXI in Appendix E. The combined LIMS-Two Stage-Flotation circuit can produce the highest possible grade (over 71.3% Fe_(T) with only 0.86% SiO₂). The mineralogy of the concentrate (underflow) along with tailing (froth) was analyzed by XRD, and the patterns with identified minerals are shown in Figure XXII and Figure XXIII in Appendix E. The results are similar to those from Sample A. However, this ultra-high purity is achieved at a cost to efficiency, with the mass pull plummeting to ~14–20% and the associated iron recovery similarly low. This circuit, therefore, demonstrates the upper limit of concentrate quality achievable but may not be viable for bulk production due to low product yield. For an optimal balance of high grade and excellent recovery, the two-stage LIMS process after fine grinding (15 µm) stands out as the superior flowsheet for this sample.

Table 38. Comparison of the results achieved in three different processing routes at different particle sizes (Sample A).

D. J. J.	M B II (0()	Assay '	Value (%)	Distribution Value (%)			
Products	Mass Pull (%)	Fe _(t)	SiO ₂	Fe _(t)	SiO ₂		
Feed		67.82	4.49	100.0	100.0		
As-received Feed (45 µm)							
Flotation	75.67	70.16	1.46	78.28	24.61		
LIMS	97.53	68.7	3.88	98.80	84.28		
LIMS – Two Stage	94.8	68.84	3.37	95.4	71.1		
LIMS-Two stage and Flotation	26.05	70.57	1.05	27.11	6.01		
Feed milled to P ₈₀ 30 µm	00.04	74.47	0.00	00.40	40.44		
Flotation	63.31	71.17	0.93	66.43	13.11		
LIMS – Two Stage	94.21 92.7	70.39 70.52	1.92 1.77	97.78 96.4	40.29 36.5		
LIMS-Two Stage-Flotation	9.0	71.46	0.86	9.46	1.76		
Feed milled to P ₈₀ 15 μm							
Flotation	53.97	71.2	0.91	56.66	10.94		
LIMS	92.8	70.81	1.52	96.9	31.5		
LIMS – Two Stage	91.7	71.02	1.07	96.0	21.6		
LIMS-Two Stage-Flotation	11.77	71.41	0.84	12.39	97.80		

NRRI/TRC-2025/48 – Tripathy et al.

Table 39. Comparison of the results achieved in three different processing routes at different particle sizes (Sample C).

Bur durate	Mana Ball (0/)	Assay \	/alue (%)	Distribution Value (%)			
Products	Mass Pull (%)	Fe _(t)	SiO ₂	Fe _(t)	SiO ₂		
Feed		67.37	5.16	100.0	100.0		
As-received Feed (45 µm)							
Flotation	84.9	68.57	3.41	86.43	55.27		
LIMS	95.5	69.19	3.1	98.02	57.34		
LIMS – Two Stage	94.8	69.09	2.65	97.2	48.7		
LIMS-Two stage and Flotation	42.35	70.67	1.64	44.42	13.45		
Feed milled to 30 µm							
Flotation	71.09	70.46	1.27	74.34	17.23		
LIMS	93.5	70.35	1.82	97.7	32.7		
LIMS – Two Stage	92.3	70.76	1.55	97.0	27.6		
LIMS-Two Stage-Flotation	19.0	71.38	0.86	20.10	3.16		
Feed milled to 15 µm							
Flotation	70.9	71.07	0.99	74.81	13.40		
LIMS	92.9	70.56	1.49	97.3	26.5		
LIMS – Two Stage	92.4	70.68	1.23	96.9	21.7		
LIMS-Two Stage-Flotation	14.04	71.37	0.86	73.70	13.77		

Form Energy Battery Testing Results

NRRI's comprehensive experimental results and detailed analysis indicated that producing highpurity iron concentrates from Minnesota taconite resources is technically feasible and promising. Although the product quality parameters did not technically meet Form Energy's confidential purity specifications, refined Samples A and C were delivered to Form Energy, and their test results remain confidential. However, the initial testing showed favorable electrochemical behavior at the beginning of life in iron-air battery cells. This positive result was consistent between the two materials sourced from the two different mines.

Conclusions

This project conducted a comprehensive investigation to determine the feasibility of producing high-purity iron concentrate from two Minnesota taconite resources (from Central and Western Mesabi Range), designated as Sample A and Sample C, for use in advanced applications such as iron-air batteries. The study encompassed detailed geo-metallurgical characterization and a systematic evaluation of different beneficiation options, yielding several critical findings.

The initial characterization confirmed that both Sample A (head grade: 67.8% Fe_(T), 4.5% SiO₂) and Sample C (head grade: 67.4% Fe_(T), 5.2% SiO₂) are high-grade magnetite concentrates. The primary valuable mineral in both is magnetite (Fe₃O₄), and the principal gangue impurity is quartz (SiO₂). Advanced mineralogical analysis using EPMA revealed crucial differences in their liberation characteristics, as well as the gangue deportments within the magnetite grain in both samples.

The beneficiation study demonstrated that a two-stage Low-Intensity Magnetic Separation (LIMS) process, implemented after fine grinding, is the most effective option for producing a high-quality concentrate from both samples. The two-stage LIMS process produced a final concentrate for Sample A with an iron grade of 71.02%, a low silica content of 1.07%, and an iron recovery of 96.0%. For Sample C, the same process yielded a concentrate with an iron grade of 70.68% $Fe_{(T)}$, 1.23% silica, and an iron recovery of 96.9%. However, the remaining impurities may not be suitable for such a high-tech application precursor materials design. In addition, LIMS technology has difficulty separating ultrafine sized particles on a commercial scale.

The reverse flotation of silica was systematically investigated using a Response Surface Methodology (RSM) with Central Composite Design (CCD). This approach successfully mapped the effects of grind size and collector dosage, revealing the trade-off between concentrate grade and iron recovery. A concentrate grade of 71.2% $Fe_{(T)}$ with 0.91% silica was recovered at optimum conditions with a recovery of 56.6% for Sample A. Similarly, a concentrate with 71.07% iron with 0.99% silica was achieved at a recovery of 74.81% for Sample C.

The RSM was highly effective in developing robust predictive models, particularly for silica removal, with high correlation coefficients ($R^2 > 0.95$). A key finding from the models was the statistical significance of not only the primary variables but also their interactions (A*B) and quadratic (A^2 or B^2) effects. This confirmed that the relationship between the variables and the flotation response is complex and non-linear, making the RSM essential for identifying true optimal conditions.

The study explored a combined circuit of two-stage LIMS followed by flotation. This processing option demonstrated that it is possible to produce an ultra-pure concentrate with the absolute highest iron grade $(71.4\%Fe_{(T)})$ and lowest silica (0.85%). However, this was achieved with a

major loss of valuable minerals, with low iron recoveries of 10-20%. This confirms that while the ultimate purity limit is very high, the most effective approach is the more efficient two-stage LIMS circuit.

Although the product quality parameters did not meet Form Energy's confidential specification, our conclusion, based on the comprehensive experimental results and detailed analysis conducted in this study, is that producing a high-purity iron concentrate from the tested Minnesota taconite resources is technically feasible and highly promising.

In summary, this research has successfully established clear and effective metallurgical options to upgrade Minnesota taconite concentrates into a high-value technology-based application, iron product. The findings provide a strong technical foundation for advancing this opportunity, potentially establishing a new, domestic supply chain for a critical material for the growing energy storage market or as a potential feedstock in other non-steelmaking applications.

Based on these promising outcomes, the following steps are recommended to advance these technologies toward commercial readiness:

- 1. Develop process flowsheets with detailed material balance using both incumbent and enhanced beneficiation processes.
- 2. Conduct pilot-scale trials of the beneficiation process flowsheet to validate the bench-scale results and demonstrate scalability and robustness under continuous operation.
- 3. Generate a larger quantity of the high-purity iron concentrate with different impurity levels from the pilot trials for delivery to our industrial partner, for direct testing and validation of its performance as an anode material in their iron-air battery systems.
- 4. Expand the investigation to include a wider range of Minnesota iron resources to assess the broader applicability of these findings and to identify other potential sources of feedstock, such as a stockpile, tailings, and over-burden.
- 5. Perform a detailed techno-economic assessment of the recommended flowsheet to evaluate the capital and operating costs, and to determine the overall economic viability and competitiveness of producing battery-grade iron from Minnesota resources.
- 6. Research the use of the high-purity iron oxide as a precursor material for other non-steelmaking industrial applications, such as permanent magnets or alloys.

Acknowledgements

The authors would like to acknowledge and thank the following for their support and participation in this project:

- This project was made possible by a grant from the Minnesota Department of Commerce.
- Form Energy for collaborating throughout this project, namely Danielle Smith and Kasey Devlin.
- The Minnesota iron mining companies in the Central and Western Mesabi Range for donating test samples.
- The Natural Resources Research Institute (NRRI) teams, namely:
 - Sr. Leadership team, including Dr. Rolf Weberg, Dr. Patrick K. Schoff, Dr. Joel
 C. Hoffman, Mr. Tim White, and Mr. Kevin Kangas.
 - Mineral Processing & Metallurgy Staff Scientist Ms. Bailey Rohde.
 - o Process Mineralogists Dr. Rodney C. Johnson and Dr. Lysa Chizmadia.
 - Coleraine Analytical team, including Julie Mutchler, Quiana Busching, Greg Gargano, and Tyler Mendonsa.
 - Coleraine Operations team, including Pat Casey and Jeff Kinkel.
 - Coleraine Metallurgical Technician team, including Joe Cannella, Dan Carrigan, Eric Johnson, Donnie Reiser, Ben Stubbs, Melissa Wolfe, and others.
 - Quality, Health, Environmental, Safety & Training team, including Jean Cranston, Mike Bates, and Matt Johnson.
 - Finance, Grants, and Administrative teams, including Linda Klint, Julie Christopherson, Megan Gorder, Jesse LeMay, Lonnie Wodarz, and Robin Oberton.
- Dr. Jennifer Mitchell, Electron Microprobe Laboratory Manager at the University of Minnesota Characterization Facility for EMPA data.
- Dr. E. Dan Dahlberg, Professor of Physics at the University of Minnesota Twin Cities for VSM testing data.
- Solly Theron, Manager Quantitative Mineralogy, Hazen Research Inc., Denver, CO, for automated liberation data.
- ALS Global for geochemical data.
- Claudia Carranza, Director of University of Minnesota Duluth Sponsored Research Administration (SPA).

References

Cullity, B.D., and Graham, C.D. 2011. Introduction to magnetic materials. John Wiley & Sons.

Data Insights Market. 2024. Opportunities in Iron-air Battery Market 2025–2033, https://www.datainsightsmarket.com/reports/iron-air-battery-2029-1502121# < accessed on 17th Sept. 2025>

Form Energy. 2021. https://formenergy.com/great-river-energy-and-form-energy-break-ground-on-first-of-its-kind-multi-day-energy-storage-project/ https://formenergy.com/great-river-energy-and-form-energy-break-ground-on-first-of-its-kind-multi-day-energy-storage-project/ https://formenergy-storage-project/ <a href="https://formenergy-stora

Form Energy. 2023. https://formenergy.com/xcel-energy-receives-approval-to-build-multi-day-battery-storage-at-sherco-site/ https://formenergy.com/xcel-energy-receives-approval-to-build-multi-day-battery-storage-at-sherco-site/ https://formenergy.com/xcel-energy-receives-approval-to-build-multi-day-battery-storage-at-sherco-site/ https://formenergy.com/xcel-energy-receives-approval-to-build-multi-day-battery-storage-at-sherco-site/ https://formenergy.com/xcel-energy-receives-approval-to-build-multi-day-battery-storage-at-sherco-site/ https://formenergy-receives-approval-to-build-multi-day-battery-storage-at-sherco-site/ https://formenergy-receives-approval-to-build-multi-day-battery-storage-at-sherco-site/ https://formenergy-receives-at-sherco-site/ https://formenergy-receives-at-sherco-site/ https://formenergy-receives-at-sherco-site/ https://formenergy-receives-at-sherco

Form Energy. 2024. https://formenergy.com/great-river-energy-and-form-energy-break-ground-on-first-of-its-kind-multi-day-energy-storage-project/ https://formenergy.com/great-river-energy-and-form-energy-break-ground-on-first-of-its-kind-multi-day-energy-storage-project/ https://formenergy-storage-project/ <a href="https://formenergy-stora

French, B.M. 1968. Progressive contact metamorphism of the Biwabik Iron-formation, Mesabi Range, Minnesota. Minnesota Geological Survey, Bulletin 45, 103 p. https://conservancy.umn.edu/items/1cd2f75c-2667-4275-b9c2-cf978b7228df

Graber, T.A., and Boudreau, A.E. 2008. The distribution of trace elements in magnetite from the Duluth Complex and Biwabik Iron Formation, northeastern Minnesota, USA: Formation of zoned magnetite by fractional crystallization and subsolidus reequilibration. The Canadian Mineralogist 46:875–894 https://www.sciencedirect.com/science/article/abs/pii/S0273230007001389?via% 3Dihub

Jackson, S., Wilson, R., and Adamson, J. 2024. Breakthrough Low-Cost, Multi-Day Energy Storage, Oct. 29, 2024. https://www.iso-ne.com/static-assets/documents/100017/2024-10-29 etwg a05 iron-air battery technology and applications overview final 2.pdf

Markets and Markets. 2023. Zinc-ion Battery Market Report, Markets and Markets. https://www.marketsandmarkets.com/Market-Reports/zinc-battery-market-171978019.html https://www.marketsandmarkets.com/Market-Reports/zinc-battery-market-171978019.html https://www.com/marketsandmarkets.com/Market-Reports/zinc-battery-market-171978019.html <a href="https://www.com/marketsandmarkets.com/marketsandmarkets.com/marketsandmarkets.com/marketsandmarkets.com/marketsandmarketsandmarkets.com/marketsandmarkets.com/marketsandmarke

MIT Technology Review. 2022. Long-lasting grid battery, https://www.technologyreview.com/2022/02/23/1044962/grid-battery-iron-clean-energy/ https://www.technologyreview.com/2022/02/23/1044962/grid-battery-iron-clean-energy/ https://www.technologyreview.com/

McKerracher, R.D., Ponce de Leon, C., Wills, R.G.A., Shah, A.A., and Walsh, F.C. 2015. A review of the iron–air secondary battery for energy storage. ChemPlusChem 80:323–335.

McSwiggen, P.L., and Morey, G.B. 2008. Overview of the mineralogy of the Biwabik Iron Formation, Mesabi Iron Range, northern Minnesota. Regulatory Toxicology and Pharmacology 52.1:S11–S25. https://www.sciencedirect.com/science/article/abs/pii/S02732300 07001353

Minnesota Department of Natural Resources (MN DNR). 2016. https://files.dnr.state.mn.us/ lands minerals/mcc docs/2016 explore iron ore.pdf https://files.dnr.state.mn.us/

Morey, G.B. 1992. The Mesabi Iron Range. In Geology of Minnesota: A Centennial Volume (pp. 475–515). Minnesota Geological Survey.

- NREL. 2023. Storage Futures Study, National Renewable Energy Laboratory (NREL). https://www.nrel.gov/analysis/storage-futures <accessed on 3rd Oct. 2025>
- Pillot, C. 2019. The rechargeable battery market and main trends 2018–2030. Presented at the 36th annual international battery seminar & exhibit. Avicenne Energy.
- Rao, S., Mlinar, M., Hudak, G., Kangas, K., and Peterson, D., 2022. Opportunities offered by emerging hydrometallurgical technologies: Report to the Legislative-Citizen Commission on Minnesota Resources. Natural Resources Research Institute, University of Minnesota Duluth, Report of Investigations NRRI/RI-2022/10. 170 p.
- U.S. Department of Energy (DOE). 2021. Long Duration Storage Shot. https://www.energy.gov/sites/default/files/2021-07/Storage%20shot%20fact%20sheet_071321_%20final.pdf https://www.energy.gov/sites/default/files/2021-07/Storage%20shot%20fact%20sheet_071321_%20final.pdf https://www.energy.gov/sites/default/files/2021-07/Storage%20shot%20fact%20sheet_071321_%20final.pdf https://www.energy.gov/sites/default/files/2021-07/Storage%20shot%20fact%20sheet_071321_%20final.pdf https://www.energy.gov/sites/default/files/2021-07/Storage%20shot%20sheet_071321_%20final.pdf <a href="https://www.energy.gov/sites/default/files/default
- U.S. Energy Information Administration (EIA). 2024. Today in Energy. https://www.eia.gov/todayinenergy/ https://www.eia.gov/todayinenergy/<a href="https://www.eia.gov/todayin
- Yao, A., Benson, S.M., and Chueh, W.C. 2025. Critically assessing sodium-ion technology roadmaps and scenarios for techno-economic competitiveness against lithium-ion batteries. Nature Energy 10.3: 404–416.
- Yao, Y., et al. 2021. Assessment methods and performance metrics for redox flow batteries. Nature Energy 6: 582–588.
- Young, J. 2023. The Promise and Challenges of Flow Battery Technology, Battery Style. https://www.batterystyle.com/promise-challenges-flow-battery-technology/ accessed on 3rd Oct. 2025>

Appendices

Appendix A: Detailed Description of Analytical Methods

Physical Characterization

Physical characterization was performed to assess key properties like particle size, density, and magnetism. These parameters are critical for designing the optimal flowsheet for material handling, comminution (crushing and grinding), and physical separation.

Particle size distribution was determined by wet analysis using a vibratory shaker with ASTM standard sieves. The procedure was adapted for the material initial size: finer samples (A and C) were sieved from 74 μ m to 25 μ m (200 to 500 mesh), while coarser samples (B and D) were sieved over a wider range from 25.4 mm to 25 μ m (1 inch to 500 mesh). Following the initial analysis, Samples B and D (head samples) were crushed to below 1 mm (18 mesh) for subsequent characterization.

Similarly, the apparent density of the as-received BF concentrates samples (Samples A and C) was measured using a Quantachrome ULTRAPYC 1200e pycnometer, while the other two plant feed (also known as "head") samples (Samples B and D) were crushed to a particle size of below 1 mm and then measured for the same. Additionally, size-wise density was measured to gain a better understanding of the distribution of apparent density/specific gravity across different size intervals. Further, the bulk density of the as-received sample was measured by a standard laboratory method, and the results were recorded.

To determine the magnetic property, samples were measured using a Satmagan (Model No. 135) instrument, which had been calibrated against a standard magnetite sample, and the results were expressed with respect to the magnetite reference standard. Measurements were taken in duplicate, and the average value was reported. Similarly, magnetic susceptibility, as well as other properties, were analyzed through the hysteresis curve by analyzing the head samples in a vibrating sample magnetometer (VSM) of Model PAR155 (supplied by M/S. Lakeshore, USA) at the Physics Department of UMN-Twin Cities. Some separated products after magnetic separation were also measured in both techniques.

Chemical Characterization

Chemical analysis quantifies the total iron content to establish the sample purity (also known as "grade") and identifies the concentration of different deleterious elements such as silica, alumina, phosphorus, and sulfur that can negatively impact the battery manufacturing process and performance. All four as-received samples, as well as beneficiated products, were analyzed to understand the distribution of different elements.

The chemical analysis of iron ore involves using advanced instruments to determine the concentration of various elements and compounds. Most of the chemical analysis was carried out in-house at the NRRI Coleraine facility. The specific methods employed at NRRI Coleraine paralleled standard ISO or ASTM methodology. Total iron was measured via potentiometric titration with the Metrohm OMNIS Automated Titration System. Ferrous iron (Fe²⁺) was measured via colorimetric titration. Inductively Coupled Plasma Optical Emission Spectrometry (ICP-OES), Agilent Model No. 5800, was used for analyzing major and minor oxides. Oxides such as SiO₂, Al₂O₃, CaO, MgO, MnO, TiO₂, V₂O₅ were analyzed with a six-place Katanax SPEX X600 electric fluxer using LiMet/LiTet borate flux. Oxides such as Na₂O, K₂O, and Phos were analyzed via four-acid dissolution and ICP-OES finish. Carbon and sulfur were measured using a LECO analyzer, Model No. SC832DR, which combusts the sample and detects gases via infrared sensors. Loss

on Ignition (LOI) was determined by heating the sample at high temperatures (typically 950°C) in a muffle furnace to measure the weight loss due to volatile components.

In addition to in-house analyses, selected iron ore samples, including head (as-received) samples and flotation froth products, were analyzed at ALS Global, an external certified laboratory. ALS Global employed a comprehensive analytical package tailored for iron ore characterization. Major oxides and total iron were determined using fused disc XRF under the "Iron Ore Package" (ME-XRF21u), while Loss on Ignition (LOI) was measured by heating samples to 1000°C in a muffle furnace (OA-GRA05x). Trace elements were analyzed via fused bead preparation, acid digestion, and ICP-MS (ME-MS81™). These methods ensured high precision and compliance with international standards for geochemical analysis.

Mineralogical Characterization

Mineralogy identifies the specific iron-bearing minerals (magnetite) as well as other associated gangue minerals. Various characterization techniques, such as XRD, EPMA, and Mineral Liberation Analysis (MLA), are employed to understand how iron-bearing minerals are interlocked with gangue minerals, which is crucial for designing the liberation and concentration strategy.

XRD Analysis

The as-received feed samples, as well as other beneficiated products for XRD analysis, were ground to a particle size of -74 μm (-200 mesh). A portion of this material was further milled to approximately -37 μm (-400 mesh) using an agate mortar and pestle. XRD scans were collected from 5° to 70/90° 20 with a step size of 0.02°, a dwell time of 0.5 seconds, and operating conditions of 40 mA and 45 kV. The analyses were conducted using a Bruker D2 Phaser diffractometer at NRRI Coleraine. The background correction was applied, and phase identification was performed using DIFFRAC.SUITE software along with powder diffraction database (ICDD). The relative abundance of identified minerals was quantified through Rietveld analysis using Siroquant V4 (Sietronics).

Electron Probe Microanalyzer

The Electron Probe Microanalyzer (EPMA) was utilized to conduct a multi-faceted investigation of the ore samples as well as beneficiated products. The primary technique involved detailed point analysis to determine the precise quantitative chemical composition of various mineral phases (e.g., iron oxides, silicates, carbonates). This was complemented by elemental mapping, which visually illustrates the spatial distribution of key elements across individual particles, revealing crucial information about mineral intergrowths, textures, and liberation characteristics. The data gathered from these analyses, with a specific focus on the chemistry of magnetite, was then used to establish geo-chemical correlations, providing insights into the ore's formation conditions and geological history.

The analysis was performed using a JEOL JXA-8530F Plus Electron Probe Microanalyzer controlled by Probe for EPMA software at the CharFac facility, UMN-TwinCities. Prior to analysis, samples were mounted in epoxy, polished to a mirror finish, and carbon-coated to ensure electrical conductivity. The procedure involved using Backscattered Electron (BSE) imaging to locate and identify target mineral grains. All quantitative analyses were conducted using an accelerating voltage of 20 keV and a beam current of 20 nA, with a beam spot size of ~1µm and the dwell time of 10 seconds on-peak for each element. These specific parameters were chosen to generate a strong X-ray signal for accurate detection while minimizing potential damage to the sample from the electron beam.

For this EPMA analysis, the BF concentrate Samples A and C were first homogenized and riffle split to obtain representative sub-samples. Each sub-sample was then subjected to wet screening using a 500 mesh (25 μ m) sieve to separate the material into two size fractions: a coarse fraction (+25 μ m/+500 mesh) and a fine fraction (-25 μ m/-500 mesh). This resulted in four distinct subsamples for analysis: A (+500 mesh), A (-500 mesh), C (+500 mesh), and C (-500 mesh). Some beneficiated products were also analyzed to visualize the separation.

Automated Mineral Analysis

To quantitatively characterize the ore, BF concentrate Samples A and C were sent to Eagle Engineering, Butte, MT for automated mineralogical analysis. The analysis was performed using an Automated Mineralogy Identification and Characterization Analysis (AMICS) platform, a modern scanning electron microscope (SEM) based system that integrates the strengths of both Mineral Liberation Analysis (MLA) and QEMSCAN technologies. Consistent with other analytical preparations, each sample was separated into two size fractions: +25 μ m (+500 mesh) and -25 μ m (-500 mesh). The primary objectives were to determine the modal mineralogy, the degree of iron ore liberation, key mineral associations, and the average particle size for each fraction.

The AMICS system works by rastering an electron beam across polished sample sections with a fixed grid size of 2 μ m. At each point, the instrument collects energy-dispersive X-ray (EDS) and backscattered electron (BSE) signals, which are then automatically compared against a comprehensive mineral database to identify the phase. The analysis was conducted using an accelerating voltage of 25 kV and a probe current of 11 nA. To ensure the results were statistically robust, approximately 10,000 particles were analyzed for each sample. This procedure yielded quantitative data on mineral abundance, interlocking characteristics, and provided high-resolution images of representative particles.

NRRI/TRC-2025/48 – Tripathy et al. Appendix B - 70

Appendix B: Chemical Analysis of As-Received Iron Ore Samples (ALS Global)

Table 40. Chemical analysis of as-received iron ore samples, along with major, minor and trace elements analyzed at ALS Global.

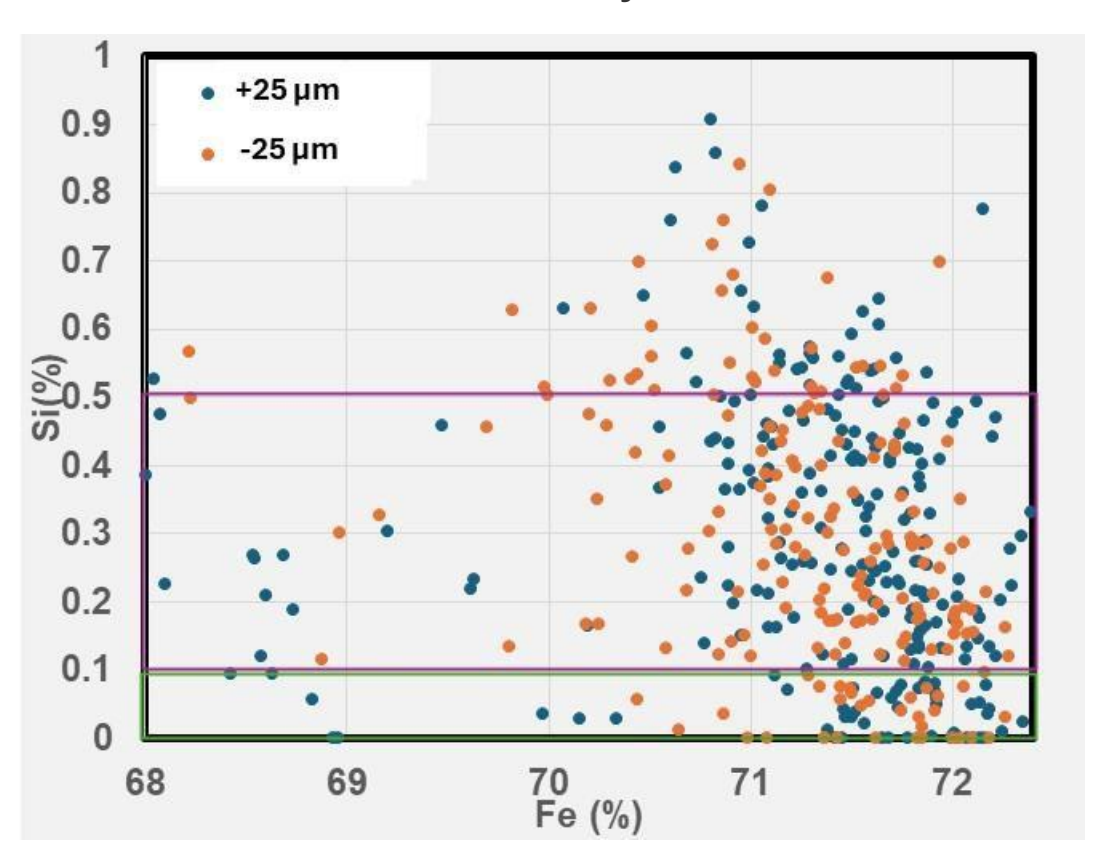
SAMPLE	Al ₂ O ₃	As	Ва	CaO	CI	Co	Cr ₂ O ₃	Cu	Fe	K ₂ O	MgO	Mn	Na₂O	Ni	Р	Pb	S	SiO ₂
DESCRIPTION	%	%	%	%	%	%	%	%	%	%	%	%	%	%	%	%	%	%
Sample A	0.06	0.002	0.004	0.24	0.006	0.001	0.024	0.004	67.88	0.02	0.32	0.091	0.024	0.007	0.015	0.004	0.012	4.62
Sample B	0.31	0.003	<0.001	1.47	0.004	<0.001	0.015	0.001	31.29	0.087	2.23	0.437	0.026	0.001	0.025	<0.001	0.018	47.5
Sample C	0.05	0.002	0.001	0.3	0.005	0.001	0.02	0.003	66.94	0.012	0.44	0.084	0.018	0.012	0.015	0.003	0.014	5.07
Sample D	0.24	0.002	<0.001	1.63	0.003	<0.001	0.004	0.002	30.27	0.049	3.04	0.356	0.023	0.001	0.021	<0.001	0.024	47.4

Table 41. Chemical analysis of as-received iron ore samples, along with major, minor and trace elements analyzed at ALS Global.

SAMPLE	Sn	Sr	TiO ₂	V	Zn	Zr	Total	LOI 1000	Ва	Ce	Cr	Cs	Dy	Er	Eu	Ga	Gd	Hf	Но	La
DESCRIPTION	%	%	%	%	%	%	%	%	ppm	ppm	ppm	ppm	ppm	ppm	ppm	ppm	ppm	ppm	ppm	ppm
Sample A	0.005	0.003	0.02	0.004	0.002	0.005	100.05	-2.6	11.7	3.1	146	0.24	0.27	0.23	0.06	0.9	0.28	0.07	0.08	2.1
Sample B	<0.001	0.002	0.02	0.001	0.001	0.003	99.82	2.69	18.5	5.1	93	1.26	0.52	0.44	0.15	1.2	0.57	0.1	0.12	2.6
Sample C	0.005	0.003	0.01	0.003	0.001	0.004	99.69	-2.18	8.8	2.8	84	0.1	0.21	0.16	0.05	0.6	0.19	<0.05	0.05	2.3
Sample D	<0.001	0.002	0.01	<0.001	<0.001	0.003	99.96	3.68	14.8	3.5	34	0.62	0.31	0.2	0.1	0.8	0.35	<0.05	0.08	1.7

Table 42. Chemical analysis of as-received iron ore samples, along with major, minor and trace elements analyzed at ALS Global.

SAMPLE	Lu	Nb	Nd	Pr	Rb	Sc	Sm	Sn	Sr	Ta	Tb	Th	Ti	Tm	U	٧	W	Υ	Yb	Zr	С	S
DESCRIPTION	Ppm	Ppm	ppm	ppm	ppm	ppm	Ppm	ppm	ppm	ppm	ppm	ppm	%	ppm	ppm	ppm	ppm	ppm	ppm	ppm	%	%
Sample A	0.04	1.24	1.2	0.3	0.7	<0.5	0.21	<0.5	5.1	<0.1	0.04	0.11	0.01	0.03	0.07	58	1.6	2.4	0.19	4	0.18	<0.01
Sample B	0.06	1.88	2.8	0.54	2.7	0.6	0.47	1.2	27.8	<0.1	0.07	0.17	0.01	0.05	0.09	23	2.2	4.8	0.31	6	1.02	<0.01
Sample C	0.02	0.5	1.2	0.3	0.4	<0.5	0.2	<0.5	4.6	<0.1	0.03	0.12	<0.01	0.02	0.07	60	1.6	1.7	0.13	3	0.27	<0.01
Sample D	0.02	0.52	1.6	0.34	1.3	0.5	0.27	<0.5	22.9	<0.1	0.06	0.14	0.01	0.03	0.08	12	1.5	3.3	0.18	4	1.32	<0.01



Appendix C: Electron Probe Micro-Analysis Results

Figure I. Correlation between total iron and silica content reported in magnetite grains for Sample C.

Figure I displays the EPMA (Electron Probe Micro-analysis) scatter plot of magnetite grains from Sample C, which provides a microscopic chemical analysis showing the relationship between iron (Fe) and silica (Si) content at hundreds of individual points on the ore particles. The data reveal that most of the magnetite is of high purity, but the finer particles (-25 μ m) tend to have a slightly higher degree of silica contamination. The following observations are summarized:

- The vast majority of the analyzed points are high in iron, clustering between 71% and 72.4% Fe. This is very close to the theoretical maximum of 72.4% Fe for pure magnetite, indicating a feasible option for a high-quality concentrate.
- Most of the high-iron mineral grains (magnetite) contain a low amount of silica, typically less than 0.5% Si. The data points with the highest iron content correspond to the lowest silica content (<0.1% Si), representing the purest magnetite grains.
- When comparing the two size fractions, the finer -25 μm particles show a noticeably higher frequency of mineral grains in the elevated silica range (0.1% to >0.5% Si) compared to the coarser fraction (+25 μm) particles. This suggests that the finer particles, while still high in iron, are more intimately intergrown with microscopic silicate impurities.

Additionally, a figure showing the silicon distribution in magnetite grains is plotted for quantification, as shown in **Figure II**. **Figure II**, derived from EPMA point analysis, illustrates the purity distribution of magnetite grains within the taconite ore by plotting the cumulative mass

percentage of magnetite against its internal silica (SiO_2) content. The curve shows that approximately 65% of the total magnetite mass is of high purity, containing less than 0.8% SiO_2 . As the silica content increases, the curve rises steeply, indicating that the remaining 35% of the magnetite mass contains progressively higher levels of silica impurities. This analysis is crucial for understanding the ore's liberation characteristics, as it quantifies the extent to which the valuable magnetite is contaminated with finely intergrown or substituted silica. Additionally, it was evident that less than 25% of the magnetite mass has less than 0.1% Si contamination.

Further, the distribution of titanium (Ti) as a trace impurity within the taconite ore, based on microscopic EPMA data, is analyzed, and the findings are shown in **Figure II**. The plots show that titanium content is generally very low across all analyzed points. The relationship between titanium and the main elements, iron (Fe) and silica (Si), reveals how impurities are distributed within the ore particles. The following observations are summarized from these two correlations:

- **Figure II**a depicts that the vast majority of analyzed points contain less than 0.02% Ti. There is no clear correlation between iron content and titanium content, meaning even the purest magnetite grains (with >71% Fe) can contain trace amounts of titanium.
- Similarly, Figure IIb reveals a weak positive correlation between titanium and silica.
 Points with higher silica content are more likely to also have detectable levels of
 titanium. This suggests that titanium impurities are often associated with silicate
 (gangue) mineral phases rather than being a direct substitution in the magnetite crystal
 structure.
- It is found that titano-magnetite inclusions are typically defined by a much higher concentration (Ti > 0.5%). Since all measured points fall well below this threshold, the analysis confirms that titanium exists only as a minor trace element in this ore and not as distinct titanomagnetite inclusions (McSwiggen et al., 2008).

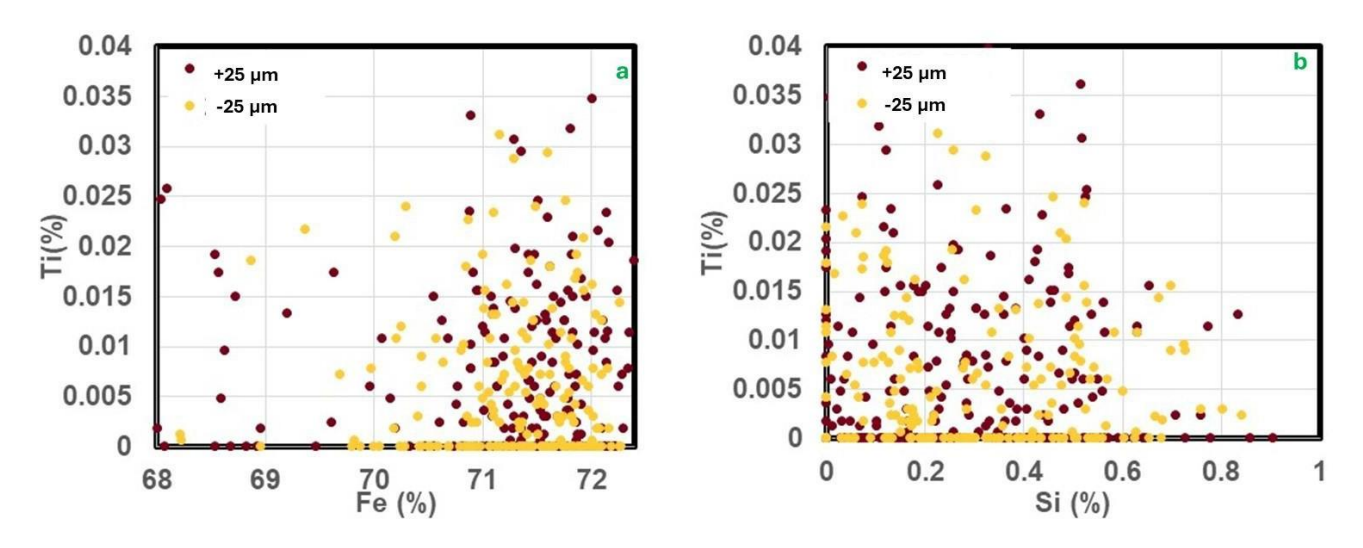


Figure II. Correlation between total iron and silica content with titanium reported in magnetite grains for Sample C.

Similar to titanium, zinc correlation in magnetite grain was analyzed from the EPMA data and the results are depicted in **Figure III**. This analysis details the distribution of zinc (Zn) as a trace impurity within the taconite ore, based on microscopic EPMA data comparing coarse (+25 µm)

and fine $(-25 \mu m)$ particles. The following observations are summarized from these two correlations.

- The data shows that zinc is present at very low concentrations, with the vast majority of analyzed points containing < 0.02% Zn.
- **Figure III**a shows no clear correlation between the iron (Fe) content and zinc content. This indicates that zinc is not significantly substituting for iron within the magnetite crystal lattice.
- **Figure III**b reveals a weak positive correlation between zinc and silica (Si). Points with higher silica content are more likely to contain detectable levels of zinc. This suggests the zinc impurity is primarily associated with the silicate (gangue) mineral phases rather than with the pure magnetite itself.
- In summary, the analysis confirms that zinc is a minor trace impurity in this ore and is more closely linked to the silicate gangue than to the magnetite.

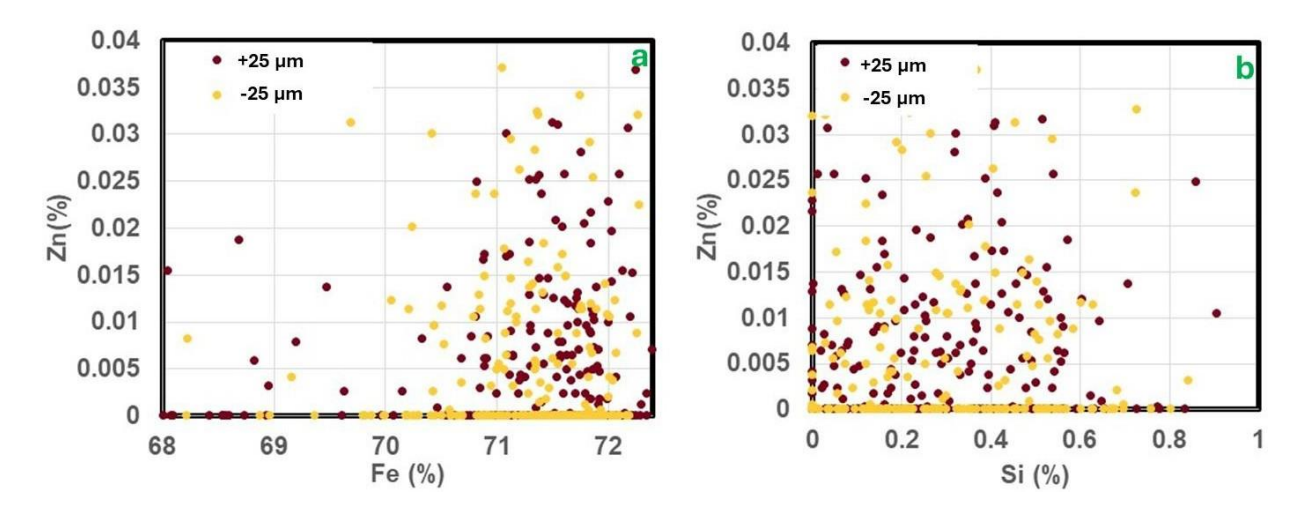


Figure III. Correlation between total iron and silica content with zinc reported in magnetite grains for Sample C.

The correlation of manganese in magnetite grain was analyzed from the EPMA data and the results are depicted in **Figure IV**. This analysis details the distribution of manganese (Mn) as a trace impurity within the taconite ore, based on microscopic EPMA data comparing coarse (+25 μ m) and fine (-25 μ m) particles. The following observations are summarized from these two correlations.

- Manganese is present as a minor trace element, with most analyzed magnetite grains containing < 0.025% Mn.
- **Figure IV**a shows no clear correlation between the iron (Fe) content and manganese content. This indicates that manganese does not systematically substitute for iron within the magnetite crystal structure. However, a few grains are found with Mn that is substituting for iron within the crystal lattice of the magnetite (Fe₃O₄). In mineralogy, it's common for elements with similar sizes and chemical properties to replace one another in a crystal structure. Manganese (Mn²⁺) can easily take the place of iron (Fe²⁺)

in the magnetite lattice (French, 2008; Graber and Boudreau, 2008; McSwiggen et al., 2008).

• **Figure IV**b reveals a weak positive correlation between manganese and silica (Si). Points with higher silica content are more likely to contain detectable levels of manganese, suggesting the manganese impurity is primarily associated with the silicate (gangue) mineral phases.

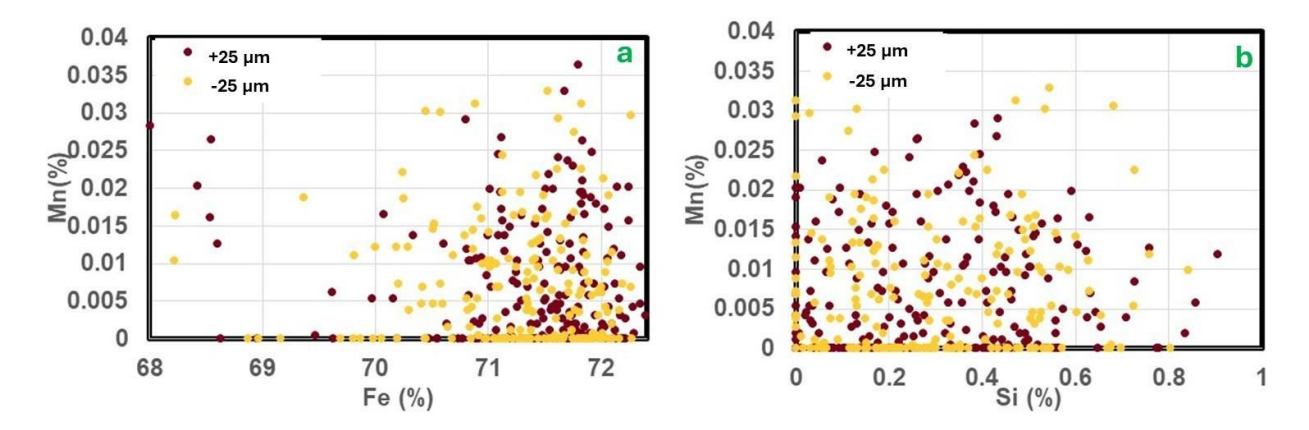


Figure IV. Correlation between total iron and silica content with manganese reported in magnetite grains for Sample C.

The correlation of calcium in magnetite grain was analyzed from the EPMA data and the results are depicted in **Figure V**. This analysis details the distribution of calcium (Ca) as a trace impurity within the taconite ore, based on microscopic EPMA data comparing coarse (+25 μ m) and fine (-25 μ m) particles. The following observations are summarized from these two correlations.

- Calcium is present as a minor impurity, with most analyzed points containing <0.04%
 Ca.
- **Figure V**a shows no clear correlation between the iron (Fe) content and calcium content. This indicates that calcium does not substitute for iron within the magnetite crystal structure.
- Figure Vb depicts a weak positive correlation between calcium and silica (Si). Points
 with higher silica content are more likely to contain detectable levels of calcium,
 suggesting the calcium impurity is primarily associated with the silicate (gangue)
 mineral phases.
- So, the Ca is present as separate, sub-microscopic mineral inclusions that are physically attached to or embedded within the magnetite grains.
- In taconite from Minnesota's Mesabi Range, these are likely tiny particles of calciumbearing minerals like carbonates (calcite, ankerite) or silicates (amphibole) (Morey, 1992).

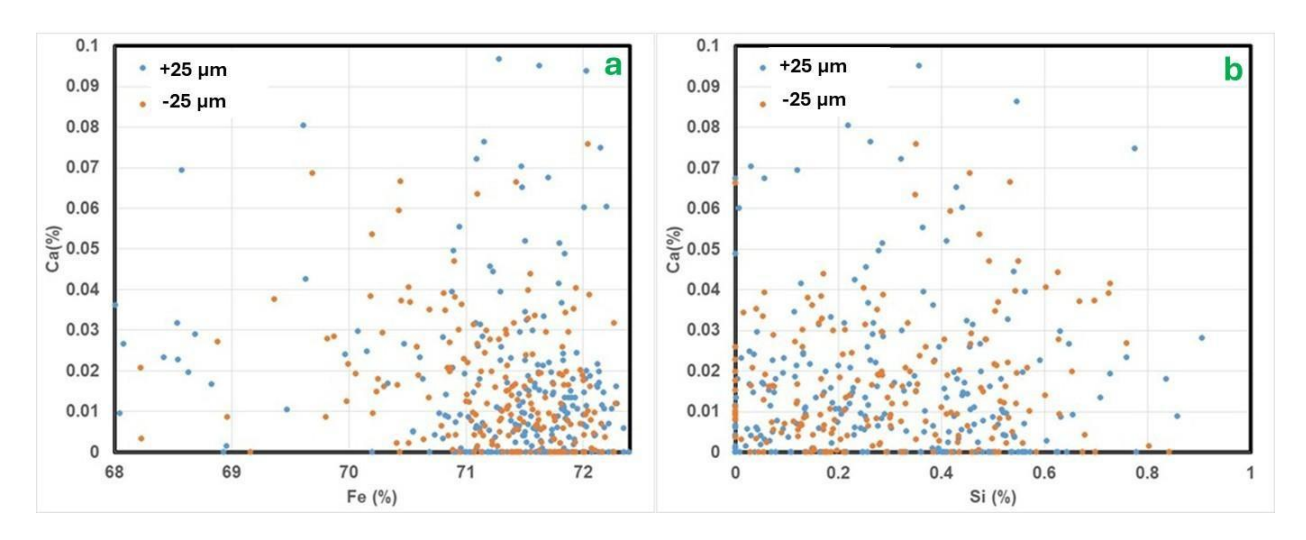


Figure V. Correlation between total iron and silica content with calcium reported in magnetite grains for Sample C.

The correlation of magnesium in magnetite grain was analyzed from the EPMA data, and the results are depicted in **Figure VI**. This analysis details the distribution of magnesium (Mg) as a trace impurity within the taconite ore, based on microscopic EPMA data comparing coarse (+25 μ m) and fine (-25 μ m) particles. The following observations are summarized from these two correlations.

- Magnesium is present at very low concentrations, with the vast majority of points analyzed showing at or trace levels of Mg.
- **Figure VI**a shows no correlation between the iron (Fe) content and magnesium content, confirming that magnesium is not present within the magnetite crystal structure.
- **Figure VI**b reveals a weak positive correlation between Mg and Si. The presence of magnesium is almost exclusively detected in points that also contain silica, strongly suggesting the magnesium impurity is part of the silicate (gangue) mineral phases.
- In summary, the analysis confirms that magnesium is a minor trace impurity in this ore
 and is entirely associated with the silicate gangue rather than the magnetite itself. Mg
 may be substituting for Fe in the magnetite lattice, but not as readily or uniformly as
 Mn. The magnetite grains may contain ultra-fine inclusions of other magnesiumbearing silicate minerals (like amphiboles or talc-like minerals) that are common in
 taconite (Morey, 1992).

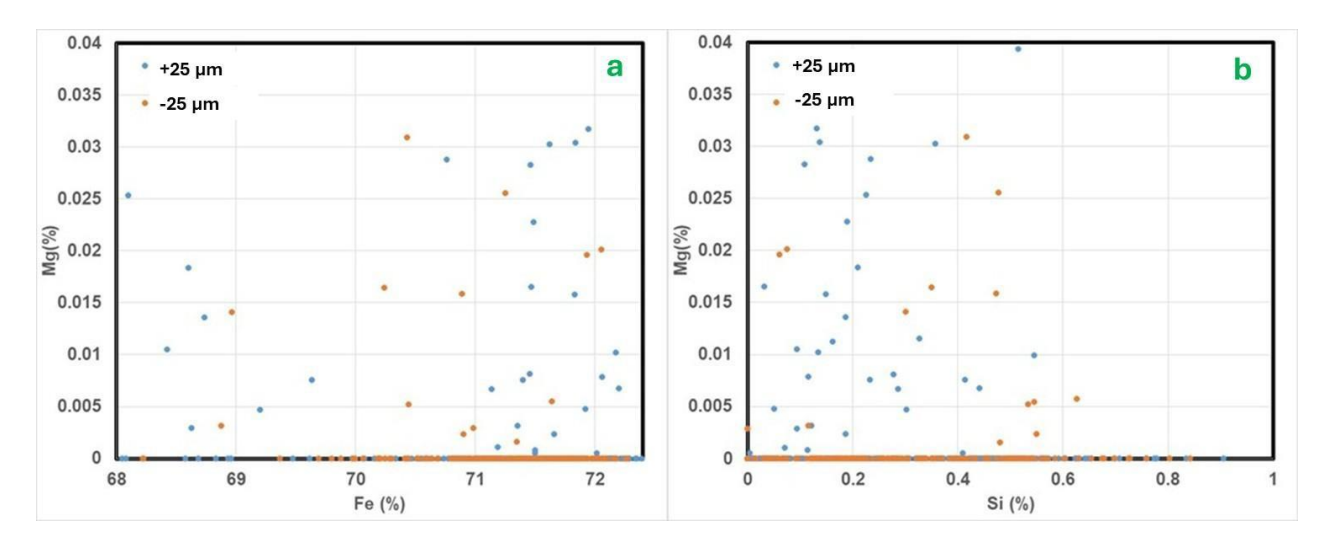


Figure VI. Correlation between total iron and silica content with magnesium reported in magnetite grains for Sample C.

The correlation of sodium in magnetite grain was analyzed from the EPMA data and the results are depicted in **Figure VII**. This analysis details the distribution of sodium (Na) as a trace impurity within the taconite ore, based on microscopic EPMA data comparing coarse (+25 µm) and fine (-25 µm) particles. The following observations are summarized from these two correlations.

- Sodium is present at very low concentrations, with the vast majority of analysed points containing trace-level Na.
- **Figure VII**a shows no correlation between the iron (Fe) content and sodium content, confirming that sodium is not present within the magnetite crystal structure.
- **Figure VII**b reveals a weak positive correlation between Na and Si. The presence of sodium is almost exclusively detected in points that also contain silica, strongly suggesting the sodium impurity is part of the silicate (gangue) mineral phases.
- In summary, the analysis confirms that sodium is a minor trace impurity in this ore and
 is entirely associated with the silicate gangue rather than the magnetite itself. Na is
 present as separate, sub-microscopic mineral inclusions that are physically attached
 to or embedded within the magnetite. In taconite from Minnesota's Mesabi Range,
 these are likely tiny particles of sodium-bearing silicate minerals, such as specific
 amphiboles (e.g., riebeckite) or feldspar group of minerals.

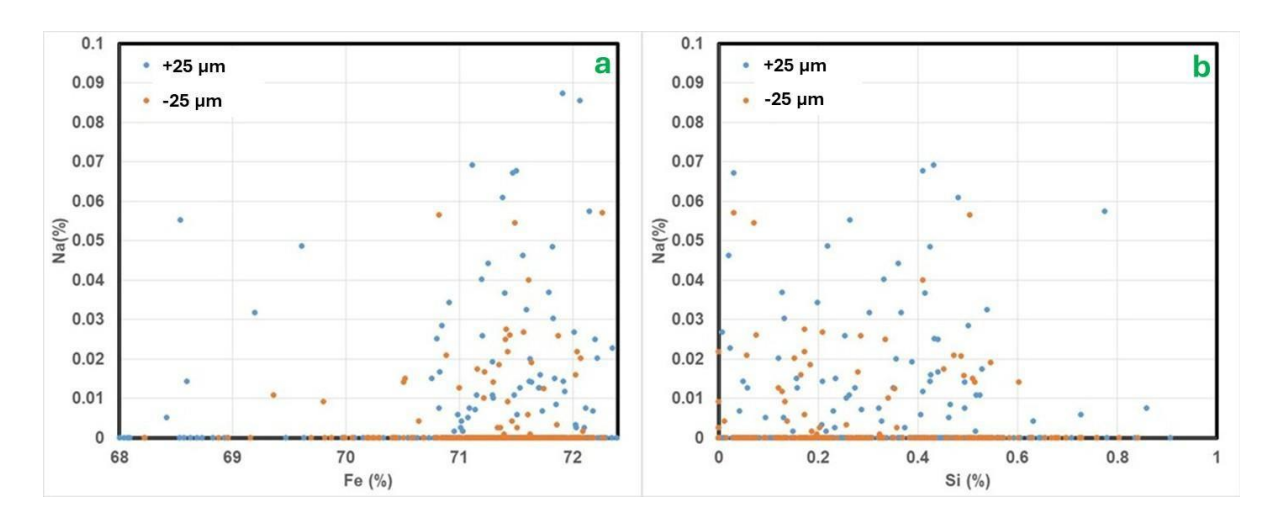


Figure VII. Correlation between total iron and silica content with sodium reported in magnetite grains for Sample C.

Similar correlations were observed for potassium, depicted in **Figure VIII**. In general, K is found in separate, microscopic particles of minerals like stilpnomelane or K-feldspar, which are remnants from the original taconite rock that were not fully liberated during processing.

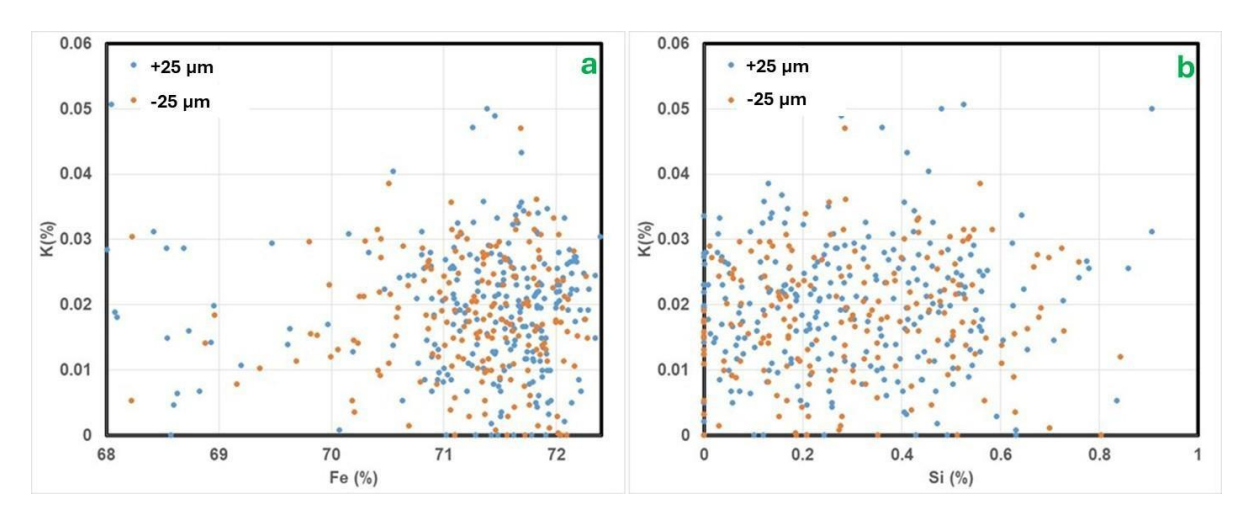


Figure VIII. Correlation between total iron and silica content with potassium reported in magnetite grains for Sample C.

The correlation of phosphorous (P) in magnetite grain was analyzed from the EPMA data and the results are depicted in **Figure IX**. This analysis details the distribution of phosphorous as a trace impurity within the taconite ore, based on microscopic EPMA data comparing coarse (+25 μ m) and fine (-25 μ m) particles. P is found in separate, ultra-fine mineral inclusions that are physically stuck to the outside of the magnetite grains. For phosphorus in the Mesabi Range, the source mineral is almost always apatite (Ca₅(PO₄)₃(F,Cl,OH)).

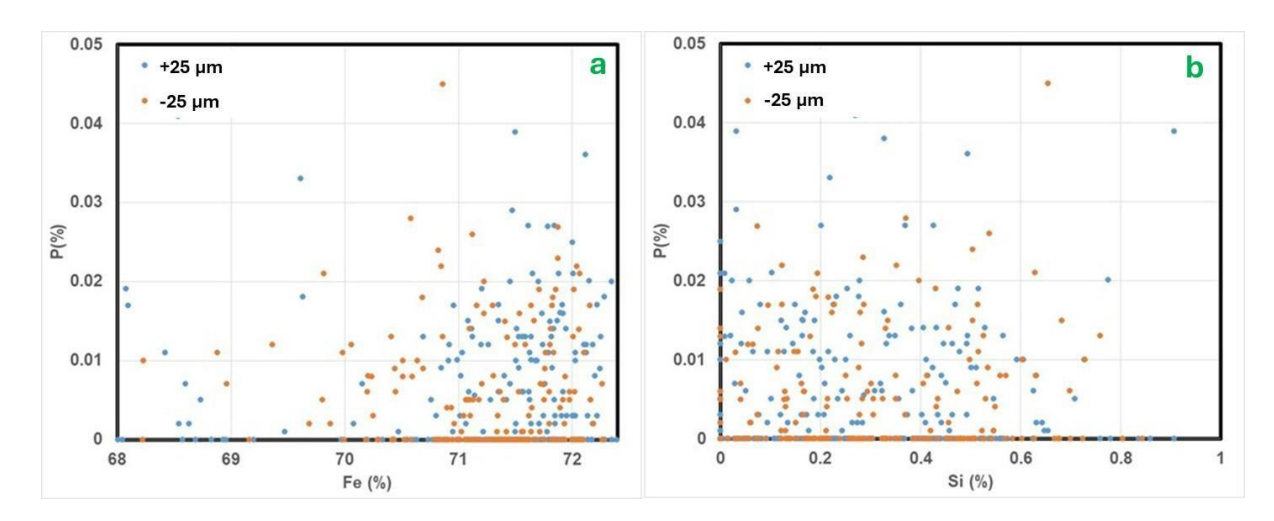


Figure IX. Correlation between total iron and silica content with phosphorous reported in magnetite grains for Sample C.

The correlation of sulfur (S) in magnetite grain was analyzed from the EPMA data and the results are depicted in **Figure X**. This analysis details the distribution of sulfur as a trace impurity within the taconite ore, based on microscopic EPMA data comparing coarse (+25 μ m) and fine (-25 μ m) particles. Sulfur is found in separate, ultra-fine mineral inclusions that are physically stuck to the outside of the magnetite grains. The source for sulfur is sulfide minerals, most commonly pyrite (FeS₂) or pyrrhotite. Figure Xa and b show highly scattered data with no correlation. The sulfur content is independent of both the magnetite's purity (Fe content) and the amount of chert impurity (Si content).

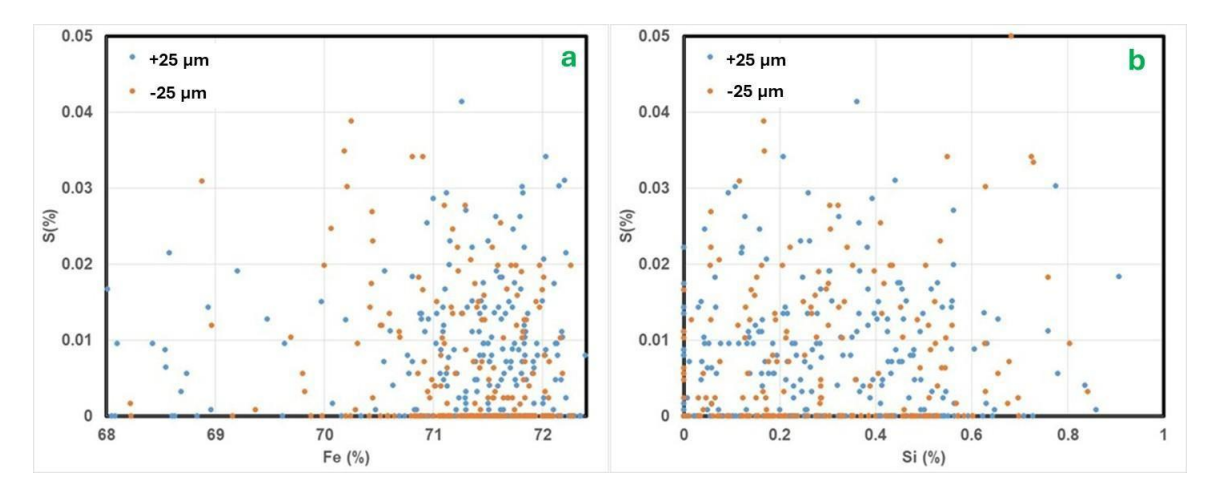


Figure X. Correlation of total iron and silica content with sulfur reported in magnetite grains for Sample C.

The correlation of chlorine in magnetite grain was analyzed from the EPMA data and the results are depicted in **Figure XI**. This analysis details the distribution of chlorine (CI) as a trace impurity within the taconite ore, based on microscopic EPMA data comparing coarse (+25 μ m) and fine (-25 μ m) particles. Solid minerals containing chlorine are rare in this geological setting. A more likely source is microscopic fluid inclusions, tiny pockets of ancient, salt-rich water that were

trapped within the magnetite grains as they crystallized. Another possibility is residual contamination from chlorine-based reagents used in the water during mineral processing.

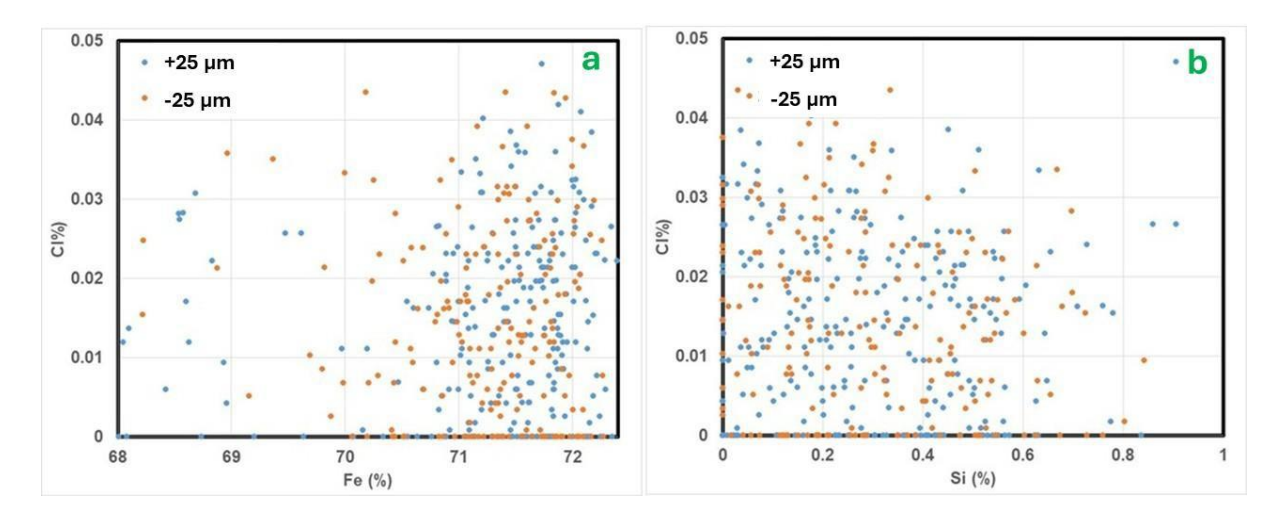


Figure XI. Correlation of total iron and silica content with chlorine reported in magnetite grains for Sample C.

Appendix D: Froth Flotation Kinetic Curves and Response Models for Samples A and C

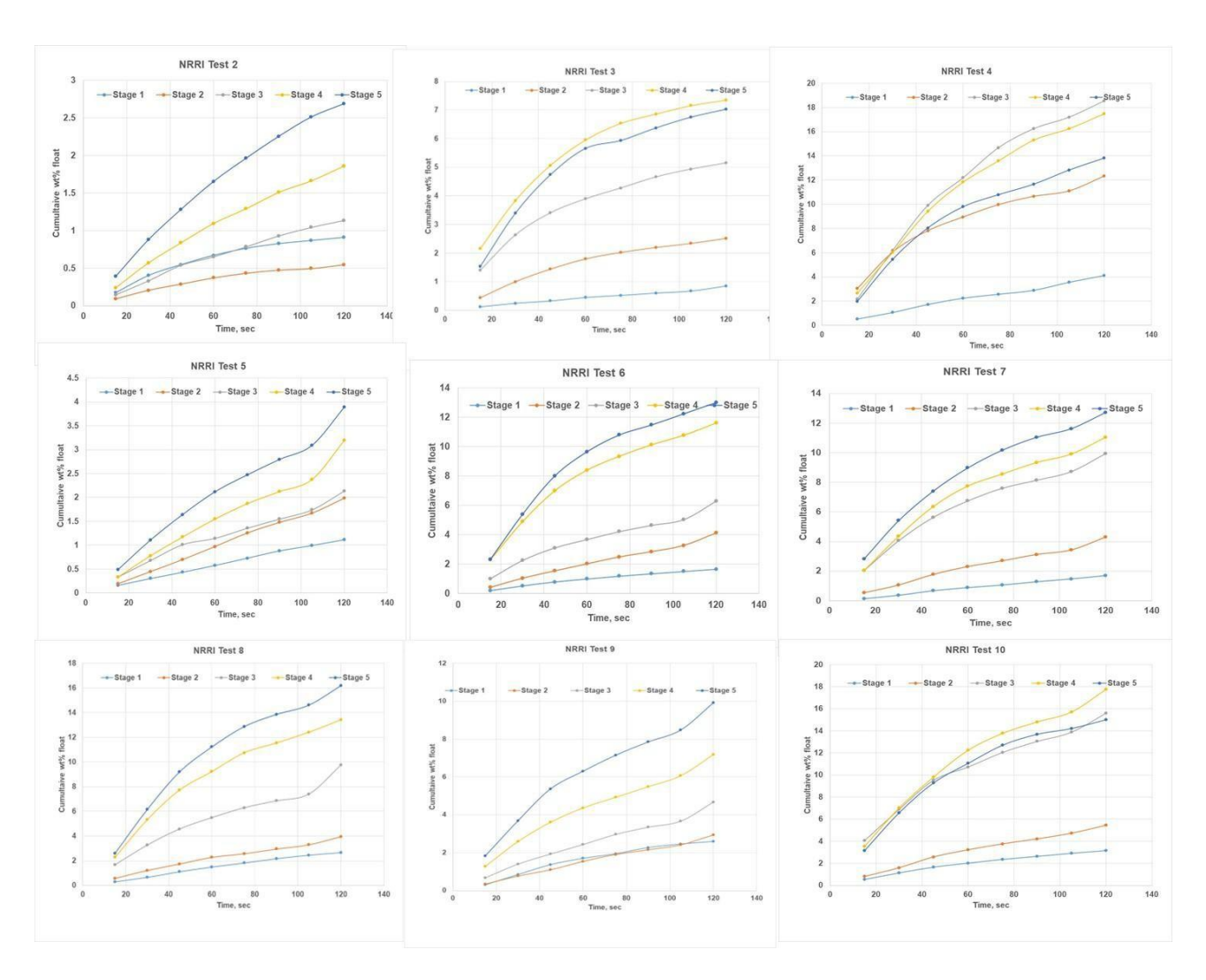


Figure XII. Kinetics curves for froth recovery of reach stage of flotation (NRRI Test 2–10) for Sample A.

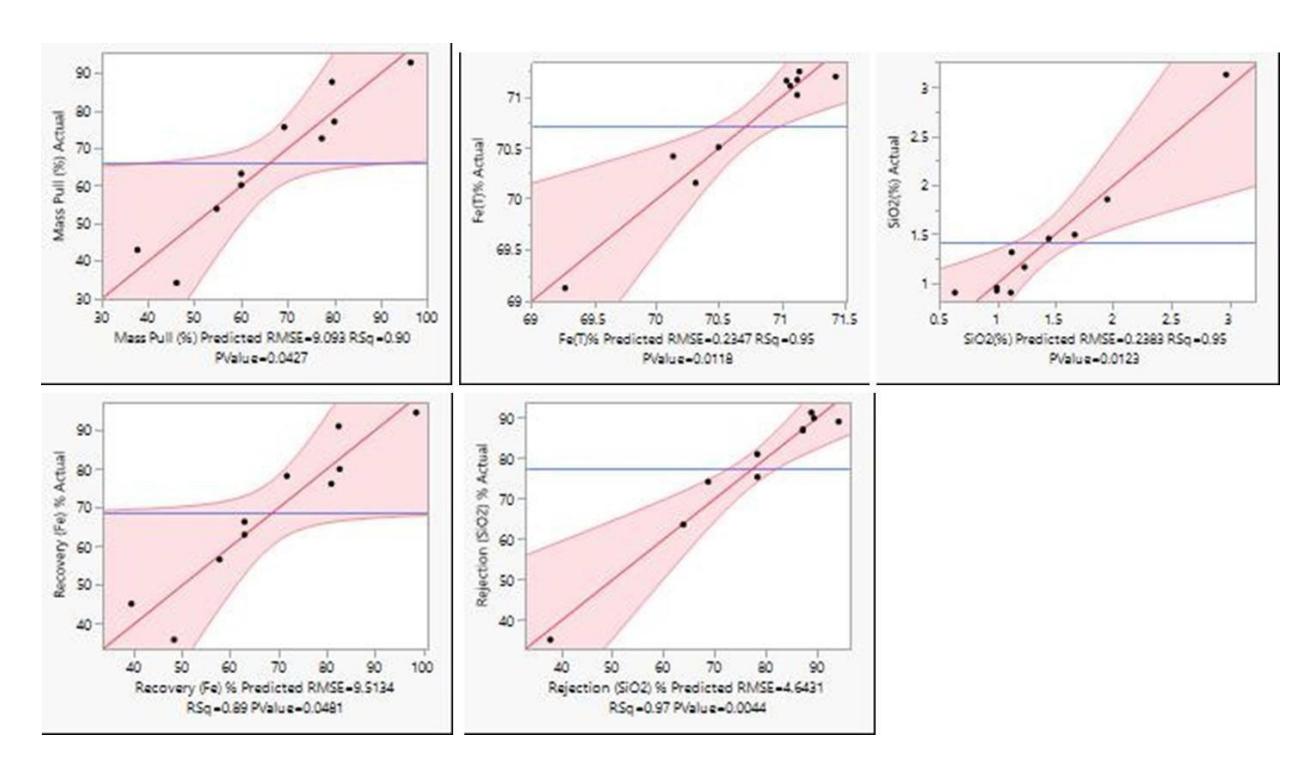


Figure XIII. Relation between actual and predicted responses based on the developed models (Sample A).

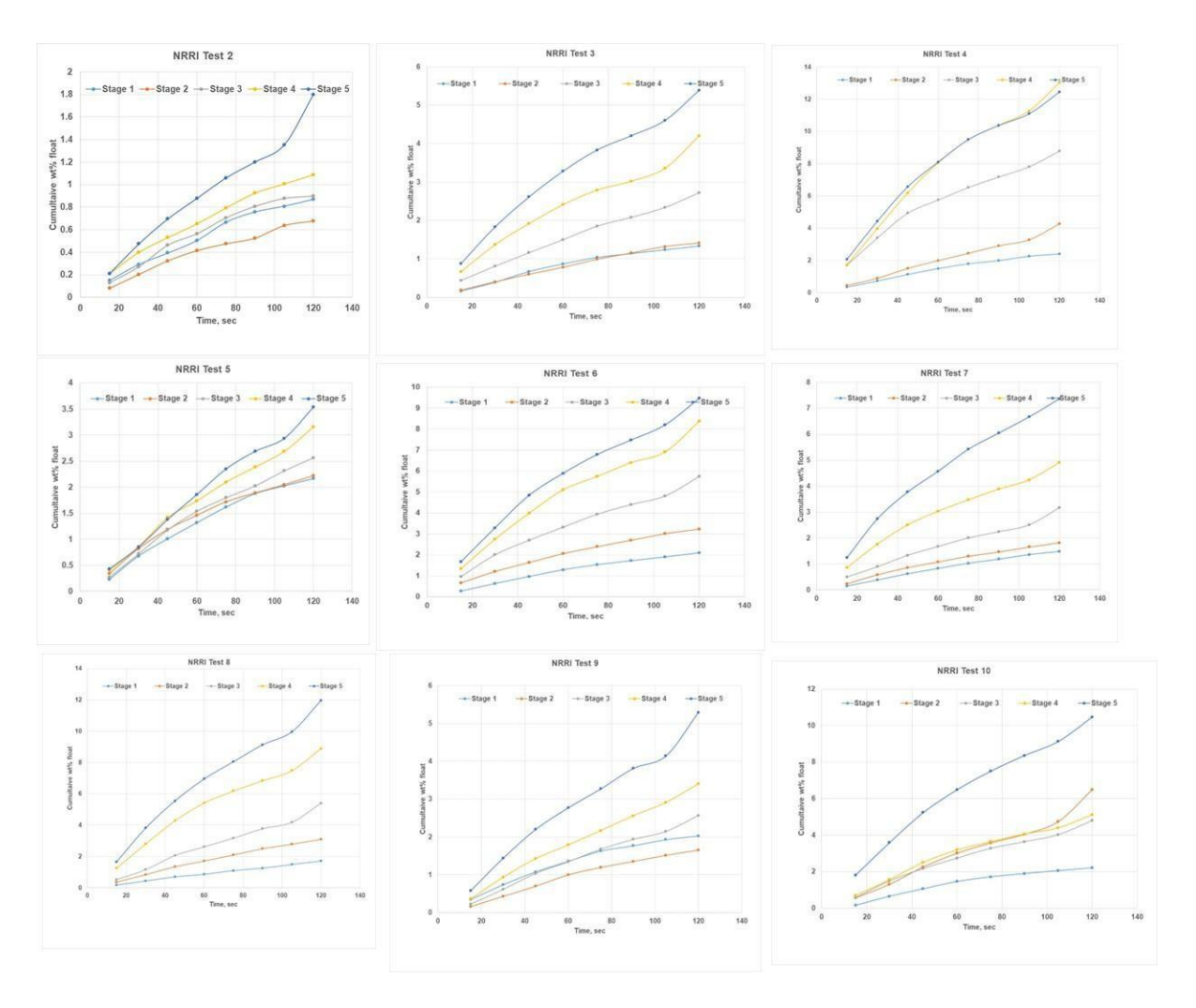


Figure XIV. Kinetics curves for froth recovery of reach stage of flotation (NRRI Test 2–10) for Sample C.

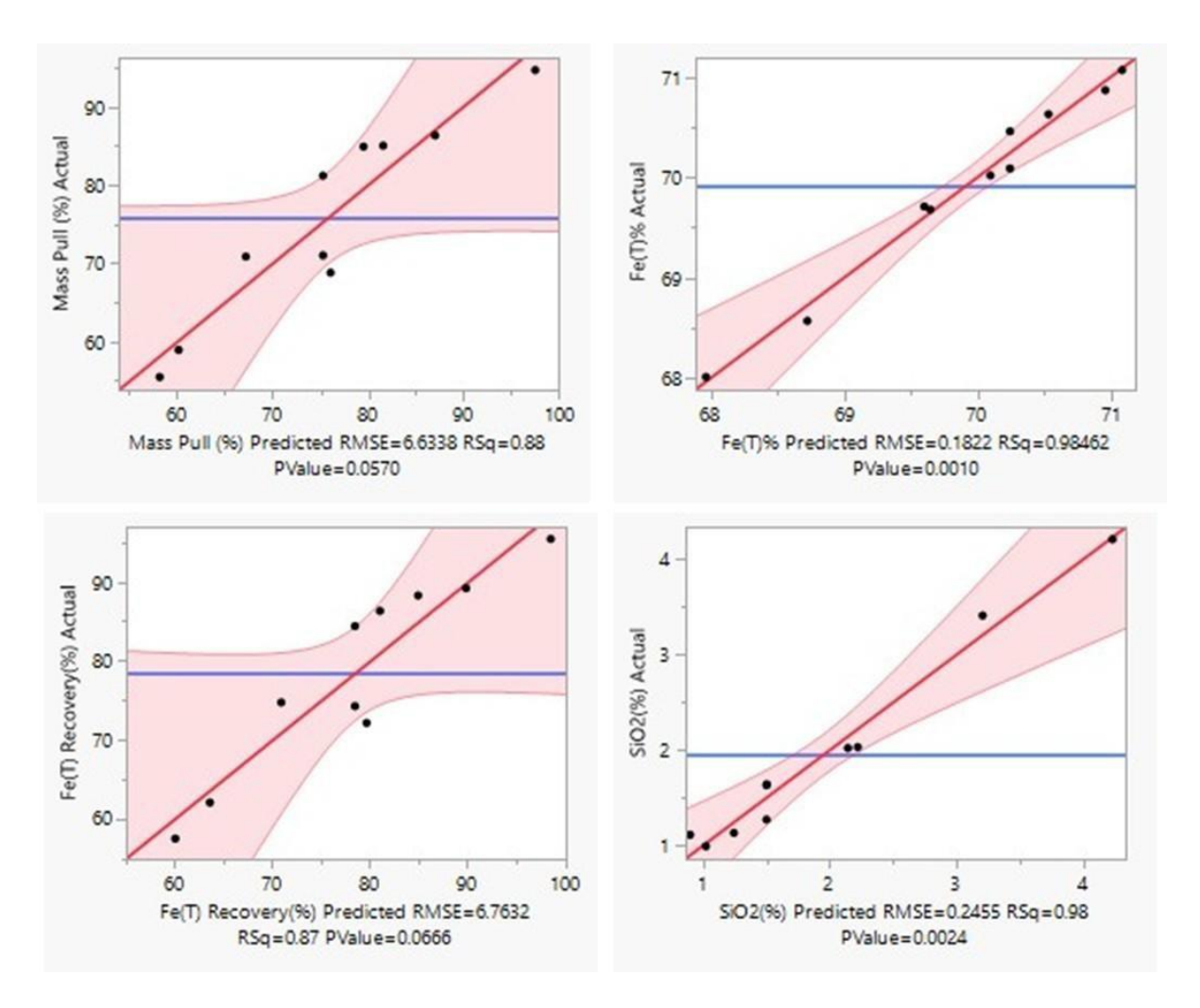


Figure XV. Relation between actual and predicted responses based on the developed models (Sample C).

Appendix E: XRD Patterns for the Beneficiated Products after Magnetic Separation and Flotation

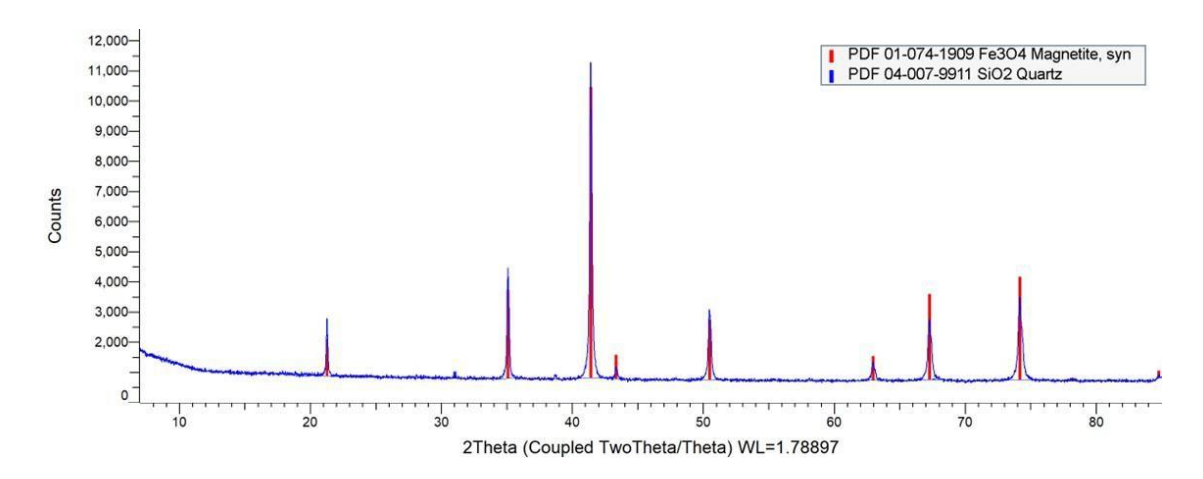


Figure XVI. XRD pattern for the magnetic fraction of the optimum condition at double-stage magnetic separation in LIMS for Sample A.

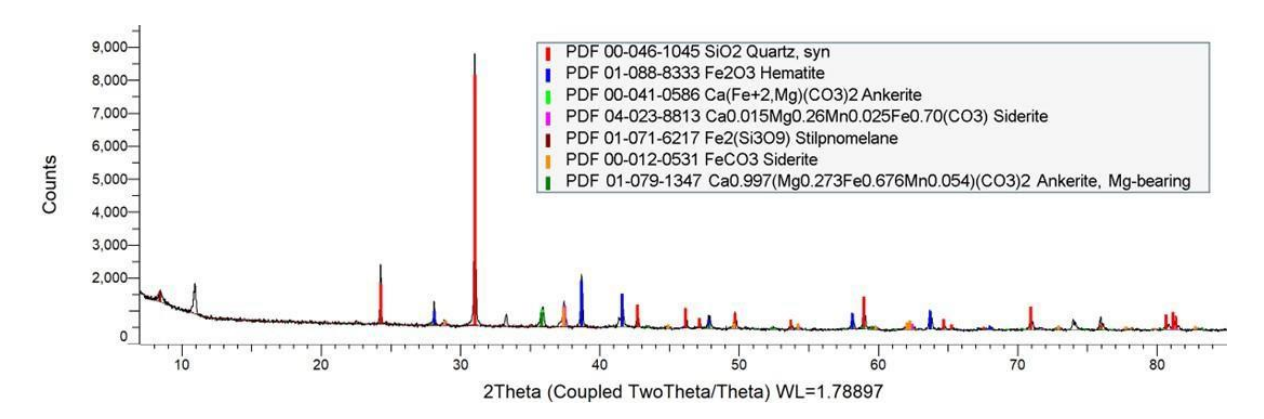


Figure XVII. XRD pattern for the non-magnetic fraction of the optimum condition at double-stage magnetic separation in LIMS for Sample A.

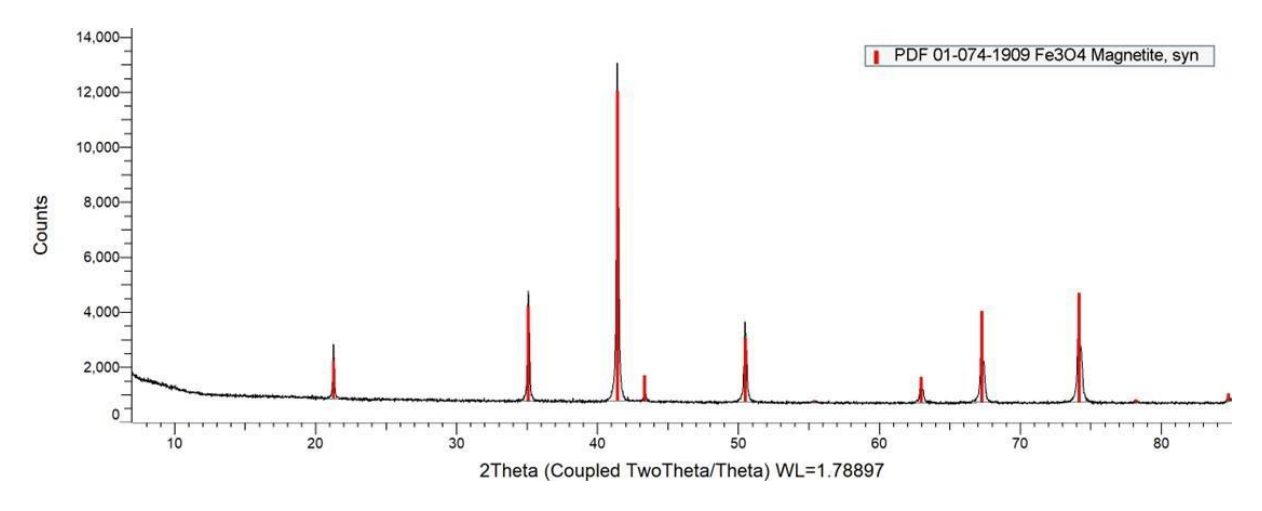


Figure XVIII. XRD pattern for the concentrate (underflow) of flotation process for Sample A.

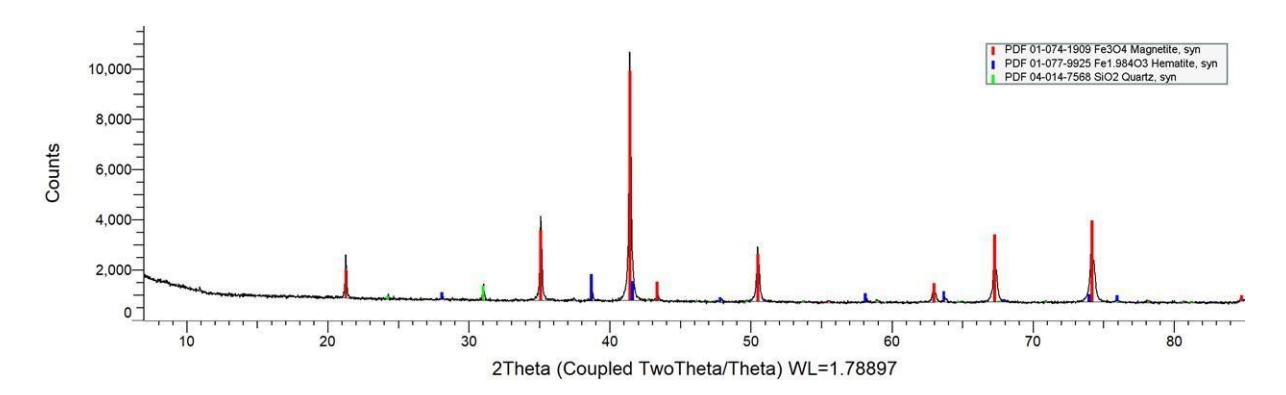


Figure XIX. XRD pattern for the tailings (froth) of flotation process for Sample A.

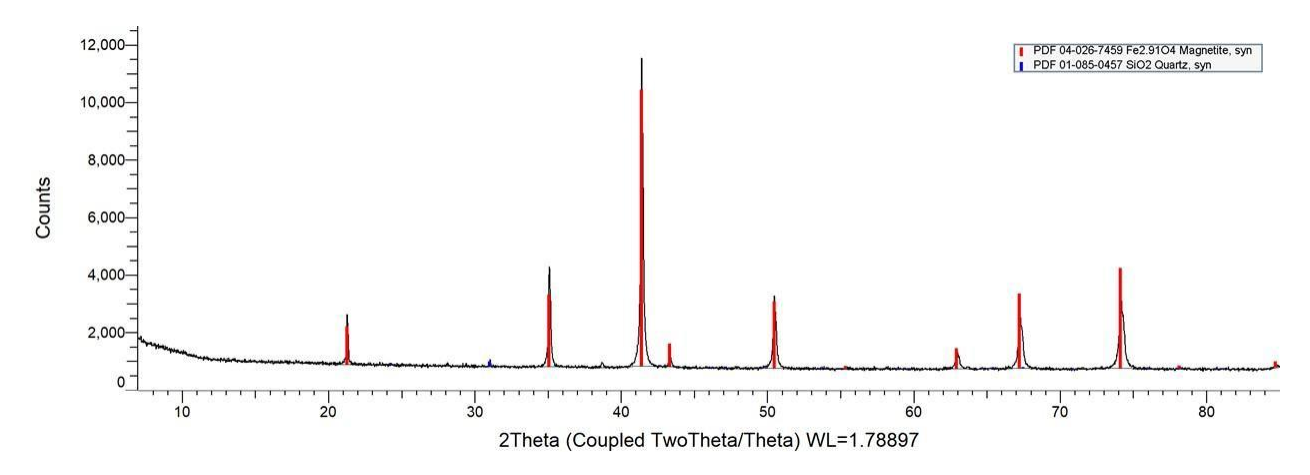


Figure XX. XRD pattern for the magnetic fraction of the optimum condition at double-stage magnetic separation in LIMS for Sample B.

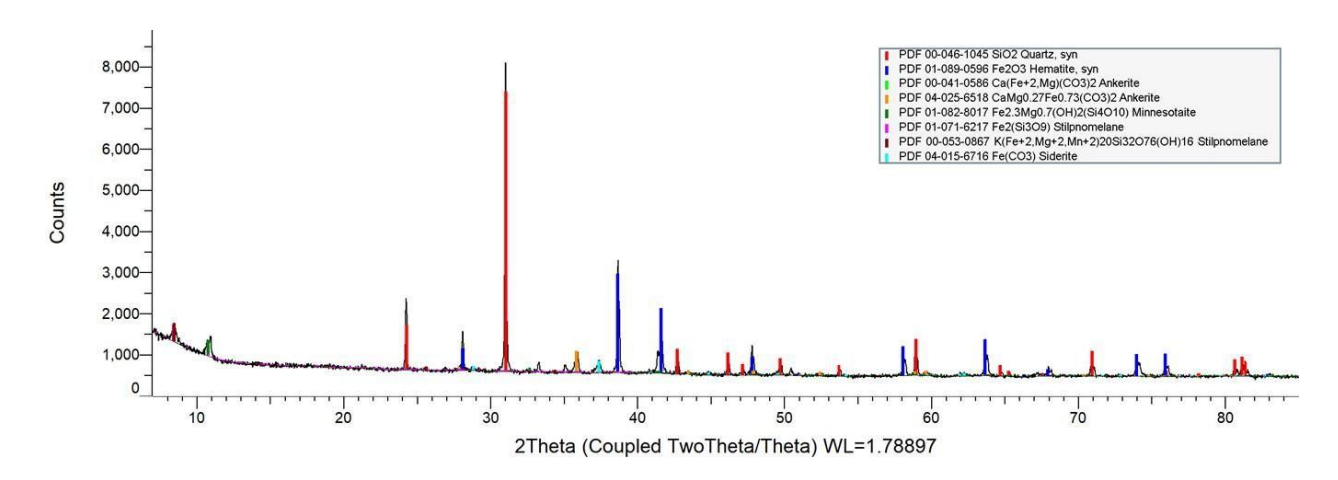


Figure XXI. XRD pattern for the non-magnetic fraction of the optimum condition at double-stage magnetic separation in LIMS for Sample B.

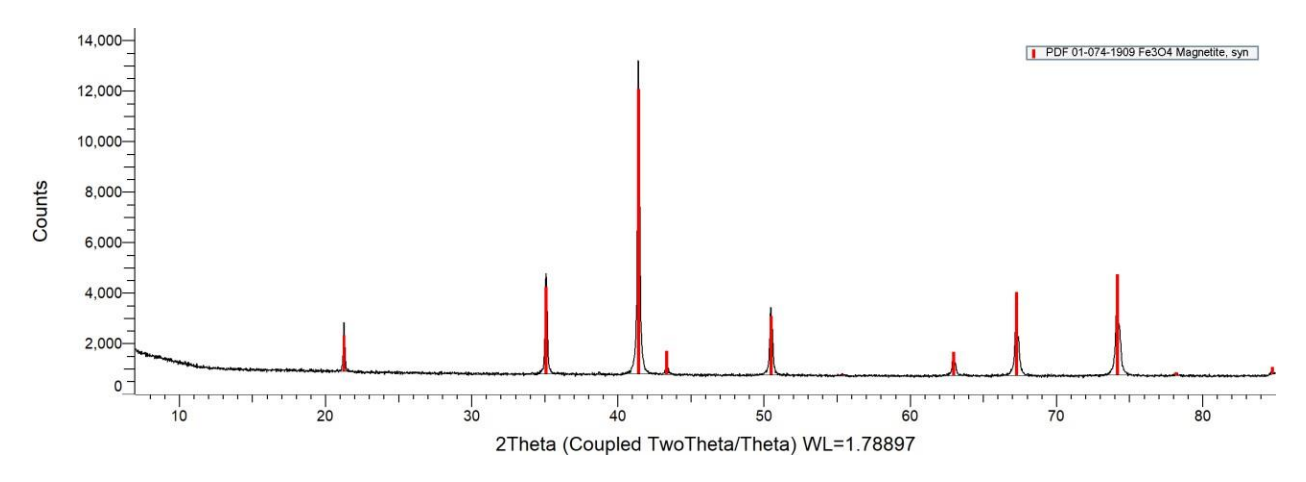


Figure XXII. XRD pattern for the concentrate (underflow) of flotation process for Sample B.

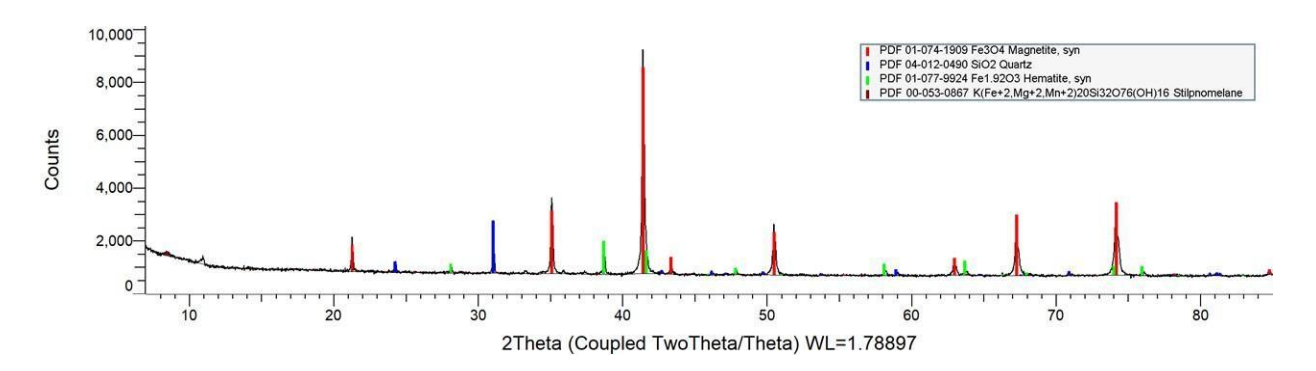


Figure XXIII. XRD pattern for the tailings (froth) of flotation process for Sample B.